An Integrated Feasibility Study of Reservoir Thermal Energy Storage (RTES) in Portland, OR, USA

Prepared by John Bershaw

Portland State University

In collaboration with:

Portland State University
Alison Horst
Ashley Streig
Darby Scanlon
Ellen Svadlenak
Jenny Liu
Peter Hulseman
Ray Wells
Robert Perkins
Tom Potiowsky

City of Portland
Alisa Kane

U.S. Geological Survey
Erick Burns (Part 2)
Colin Williams (Part 2)

AltaRock Energy Inc.
Matt Uddenberg
Trenton Cladouhos

Oregon Health Sciences University
Boz Van Houten
Noel Mingo

FINAL REPORT

Federal Agency and Organization Element	U.S. Department of Energy Geothermal Technologies Program
Award Number	DE-EE0008104
Project Title	Portland Deep Direct-Use Thermal Energy Storage (DDU-TES) Feasibility Study
Principal Investigator	John Bershaw Assistant Professor Department of Geology Portland State University Portland, OR 97201
Recipient Organization	Portland State University Office of Sponsored Programs PO Box 751 (SPA) Portland, OR 97207-0751
DUNS Number	05-222-6800
Date of Report Submission	10/28/2021
Reporting Period	10/1/2017 – 9/30/2020
Project Partners	AltaRock Energy, Inc. City of Portland Oregon Health Sciences University U.S. Geological Survey
DOE Project Team	DOE Contracting Officer – Laura Merrick DOE Project Officer – Arlene Anderson Project Monitor – Angel Nieto

EXECUTIVE SUMMARY

In regions with long cold overcast winters and sunny summers, Deep Direct-Use (DDU) can be coupled with Reservoir Thermal Energy Storage (RTES) technology to take advantage of pre-existing subsurface permeability to save summer heat for later use during cold seasons. Many aquifers worldwide are underlain by permeable regions (reservoirs) containing brackish or saline groundwater that has limited beneficial use due to poor water quality. We investigate the utility of these relatively deep, slow flowing reservoirs for RTES by conducting an integrated feasibility study in the Portland Basin, Oregon, USA, developing methods and obtaining results that can be widely applied to RTES systems elsewhere. As a case study, we have conducted an economic and social cost-benefit analysis for the Oregon Health and Science University (OHSU), a teaching hospital that is recognized as critical infrastructure in the Portland Metropolitan Area. Our investigation covers key factors that influence feasibility including 1) the geologic framework, 2) heat and fluid flow modeling, 3) capital and maintenance costs, 4) the regulatory framework, and 5) operational risks. By pairing a model of building seasonal heat demand with an integrated model of RTES resource supply, we determine that the most important factors that influence RTES efficacy in the study area are operational schedule, well spacing, the amount of summer heat stored (in our model, a function of solar array size), and longevity of the system. Generally, heat recovery efficiency increases as the reservoir and surrounding rocks warm, making RTES more economical with time. Selecting a base-case scenario, we estimate a levelized cost of heat (LCOH) to compare with other sources of heating available to OHSU and find that it is comparable to unsubsidized solar and nuclear, but more expensive than natural gas. Additional benefits of RTES include energy resiliency in the event that conventional energy supplies are disrupted (e.g., natural disaster) and a reduction in fossil fuel consumption resulting in a smaller carbon footprint. Key risks include reservoir heterogeneity and a possible reduction in permeability through time due to scaling (mineral precipitation). Lastly, a map of thermal energy storage capacity for the Portland Basin yields a total of 43,400 GWh, suggesting tremendous potential for RTES in the Portland Metropolitan Area.

PROJECT DELIVERABLES

Task 1: The technical team at Portland State University in collaboration with the U.S. Geological Survey will develop the geologic framework for modeling and for a geologic hazards assessment.

We modeled three stratigraphic surfaces (top Columbia River Basalt group (CRBG), base CRBG, and Eocene basement) using well log, outcrop, seismic, aeromagnetic, and gravity data. Products include a map of data control, three structure maps: top CRBG, base CRBG, and Eocene basement, in addition to three isochore (thickness) maps between these surfaces. A schematic cross section through the proposed well locations in the south waterfront area of the Portland basin was created. Modeled surfaces and data tables are available online in the Geothermal Data Repository (GDR).

We summarize geologic conditions and model parameters for injection rates, volume, and water injection depth, and compare to aquifer storage and recovery systems and wastewater injection guidelines in the attached report. A Coulomb stress model of displacement gradients for 1.5 meters of modeled slip on the Portland Hills fault within the Portland Basin was also completed.

We summarize likely geochemical impacts on an RTES system in the attached report. This includes results from a series of equilibrium reaction models and reactive transport models which investigate the effects of heating, native groundwater compositions, atmospheric conditions, flow rates, and reactive phases present in aquifer matrices in terms of mineral dissolution and precipitation reactions, and resulting mass transfers and changes in aquifer porosity. A CSV file with data, summary statistics and hierarchical cluster analysis results is available online in the Geothermal Data Repository (GDR).

Task 2: Develop heat and fluid flow simulation tools to produce resource estimates for Oregon Health Sciences University (OHSU) and Portland International Airport (if time allows). Methods will allow assessment of geothermal resource uncertainty resulting from geologic knowledge uncertainty (geologic geometry, and thermal and hydraulic properties).

Tools to evaluate RTES were developed and applied to the Columbia River Basalt Group (CRBG) beneath the Portland Basin. Heat and fluid flow simulations using a model for saturated-unsaturated, variable-density ground-water flow with solute or energy transport (SUTRA) were driven by an annual solar energy supply pattern and conventional building heating demand model. Simulations were done to demonstrate the effects of varying heat-delivery rate and temperature on the heat production history of the reservoir. Analytic solutions were developed to help design RTES systems (e.g., well-spacing, thermal source sizing, etc.). Finally, a map of thermal energy storage capacity was produced for the CRBG beneath the Portland Basin.

Task 3: Based on OHSU end-user needs, model the full system from an engineering standpoint including wells and pumps in the subsurface and wellheads, pipes and heat exchangers at the surface, to scale a system capable of meeting critical infrastructure needs.

A full system is described including both above and below ground infrastructure that can meet the needs of OHSU heating demand. Multiple scenarios are presented to investigate variation in costs associated with different system design. Estimated capital and maintenance costs are integrated into economic calculations.

Task 4: Evaluate and document through high-level analysis the market potential within Portland for implementation of Deep Direct-Use coupled with seasonal thermal energy storage, its economic and operational feasibility, and anticipated regulatory barriers and mitigations, with more detailed analysis for potential application within OHSU and time permitting, Portland International Airport.

The analysis contained in this report considers the costs of existing energy options in comparison to RTES, in addition to the potential environmental benefits/impacts and resiliency and reliability characteristics related to natural catastrophes. In addition to estimating the economic feasibility of an RTES system as part of an OHSU case study, we extend these results at a high level to ascertain the general market potential of applying geothermal technology to commercial buildings within Portland.

We also convened a meeting of government regulators who provided insight into permits and time needed to implement this technology across the Portland Basin. Key regulatory considerations that came out of this meeting are outlined in this report.

Task 5: Organize the project to ensure communication occurs regularly between team members and that milestones are being achieved as planned.

Quarterly meetings were held to coordinate work between team members and develop summary documents (presentations, quarterly reports, and this final report).

TABLE OF CONTENTS

INTRODUCTION

Storage of thermal energy in saline or brackish aquifers (underlying freshwater aquifers) allows use of largely undeveloped relatively low-quality groundwater-resources for matching of peak energy production with peak energy demand. Deep direct-use geothermal energy storage (DDU-TES) is a specific type of geothermal energy storage and heat exchange. According to the OECD Glossary of Environmental Statistics (1997) "direct-use" refers to energy consumption that is used at the source or is transmitted without transformation. Deep geothermal systems are direct use as they extract and use heat from water pumped out of local aquifers. According to the United States Office of Energy Efficiency and Renewable Energy (OEERE, A), "typical geothermal direct-use operations utilize a natural resource—a flow of geothermal fluid at elevated temperatures which is capable of providing heat and cooling (via absorption chillers) to buildings, commercial and residential applications, industrial processes, greenhouses, and aquaculture ponds." In the case of direct-use geothermal heating (i.e., using the temperature of the geothermal water to heat or cool equipment or spaces), the energy produced, stored, and later extracted is delivered as hot or cold water. For example, summer solar energy might be stored in a heated reservoir and then extracted in the winter. Similarly, winter low temperatures might be harvested using dry fluid coolers (i.e., heat exchange with atmosphere) for use during the summer.

The physics of this technology has been historically researched, developed, and implemented, usually under the name Aquifer Thermal Energy Storage (ATES); and this technology is mature in some parts of the world. For a systematic description and history, see Fleuchaus et al. (2018). Most commonly, ATES systems are operated in the uppermost aquifers beneath high heating/cooling demand districts of metropolitan areas. A primary distinction between most ATES systems and the saline/brackish systems summarized herein, is that saline/brackish reservoirs have much in common with traditional geothermal reservoirs, except for having comparatively low temperatures and relatively shallow depths. Saline/brackish reservoirs have geochemically evolved fluids, a consequence of comparatively low groundwater flowrates and long residence times along flow paths that are poorly connected with shallower fresh groundwater systems. For ATES, regional groundwater flow commonly causes significant drift of stored heat in the direction of regional groundwater flow, and extraction wells need to be located to optimally intercept the stored heat which mixes with regional groundwater flow. In contrast, the low groundwater flowrates within many brackish/saline systems ensures that most of the stored heat is not washed away from the injection zone. Because the proposed brackish/saline storage zones share characteristics of traditional geothermal reservoirs (particularly in terms of chemistry, flowrate, and poor-connection with shallow fresh aquifers), the term Reservoir Thermal Energy (RTES) is proposed to distinguish thermal energy storage using slow-moving geochemically-evolved aquifers from traditional ATES applications.

RTES may have advantages over ATES, and the disadvantages are seemingly tractable problems. In regions where freshwater supplies have largely been appropriated for other beneficial uses, the use of brackish/saline waters as a working fluid for heat exchange represents a new opportunity for beneficial use of these largely undeveloped groundwater resources. Deep storage of heat would prevent thermal plumes from easily reaching surface waters, preventing adverse ecological impacts. While exploration risks and costs of development of RTES will likely be higher than for ATES, working with geochemically evolved waters is standard fare for the geothermal industry, so engineering solutions already exist or are the subject of active engineering research.

The remainder of this report explores the feasibility of implementing RTES in the Portland Basin, Portland, Oregon, USA. To characterize feasibility, we begin with a detailed study of the geologic framework and associated geologic and operational hazards (Part 1). Then, we employ a heat and fluid flow model to estimate the heat resource available for an urban hospital, Oregon Health Sciences University (OHSU) using RTES technology. We also estimate the potential RTES resource if utilized throughout the Portland Basin (Part 2). The infrastructure required to fully implement RTES for OHSU is designed and associated capital and maintenance costs are estimated (Part 3). Lastly, the economics of implementing RTES in a new conventional building at OHSU are estimated, resulting in a levelized cost of heating (LCOH), which is compared to other sources of heating available to OHSU. This, in addition to considerations of the regulatory environment and societal (non-fiscal) benefits are integrated into an interpretation of feasibility (Part 4).

PART 1: PORTLAND BASIN GEOMETRY AND HAZARDS

1.1 Portland Basin Geometry

Study Area Description

The 1,300 km^2 Portland Basin contains the cities of Portland, Oregon and Vancouver, Washington, separated by the Columbia River, which traverses the basin center on its way to the Pacific Ocean (Figure 1). The Portland Basin has low heat flow which is estimated to be 50 mW/m^2 (Burns et al., 2018) with low traditional hydrothermal favorability (Williams & DeAngelo, 2008). But, there exist favorable conditions for RTES: a deep permeable low-flow aquifer system in the Columbia River Basalt Group (CRBG) that is hydraulically separated and thermally well-insulated from the overlying regional aquifer.

Geology

The Portland Basin (Figure 1) is a NW-SE trending part of the Puget-Willamette forearc trough, formed during oblique subduction of the Juan de Fuca plate beneath North America (Wells et al., 1998; Evarts et al., 2009). The forearc trough may be a flexural response of loading by the Cascade magmatic arc or Coast Range, with basin segmentation related to NW-striking dextral faults, which have been active since at least the mid-Miocene. The Willamette Valley region is seismically active with the largest historic event a M 5.7 earthquake that occurred in Scotts Mills in 1993 (Wong, 1997).

Portland Basin stratigraphy (Figure 2) records a history of volcanism and sedimentation during much of the Cenozoic. Basement consists of oceanic basalt of the Eocene Siletzia terrane, accreted to North America about 50 million years ago (Wells et al., 2014). Siletzia is overlain by marine sedimentary rocks which interfinger with Cascade volcanics to the east. A depth to the Siletzia basement map based on gravity data suggests that the Portland Basin is up to 2.5 km deep and may have extended further west to the Tualatin Basin in the Paleogene (McPhee et al., 2014). Paleogene marine sedimentation was followed by emplacement of CRBG flows in the mid-Miocene. More than a dozen basalt flows arrived via the ancestral Columbia River valley, filling in pre-existing topography with 300m or more of basalt (Beeson et al., 1985). Continued Neogene subsidence and uplift of the Portland Hills followed CRBG emplacement (Evarts et al., 2009). About 300 m of lacustrine, fluvial, and volcaniclastic rocks overlie the Columbia River Basalt. Eruption of the Boring volcanic field between 3 Ma and 50 ka produced cinder cones and associated lava flows, still visible on the east side of the basin (Evarts et al., 2009). Between about 18 and 15 ka, glacial outburst floods (Missoula floods) inundated the region to a depth of about 120m, mantling the basin with sediments derived from the continental interior (Waitt, 1985).

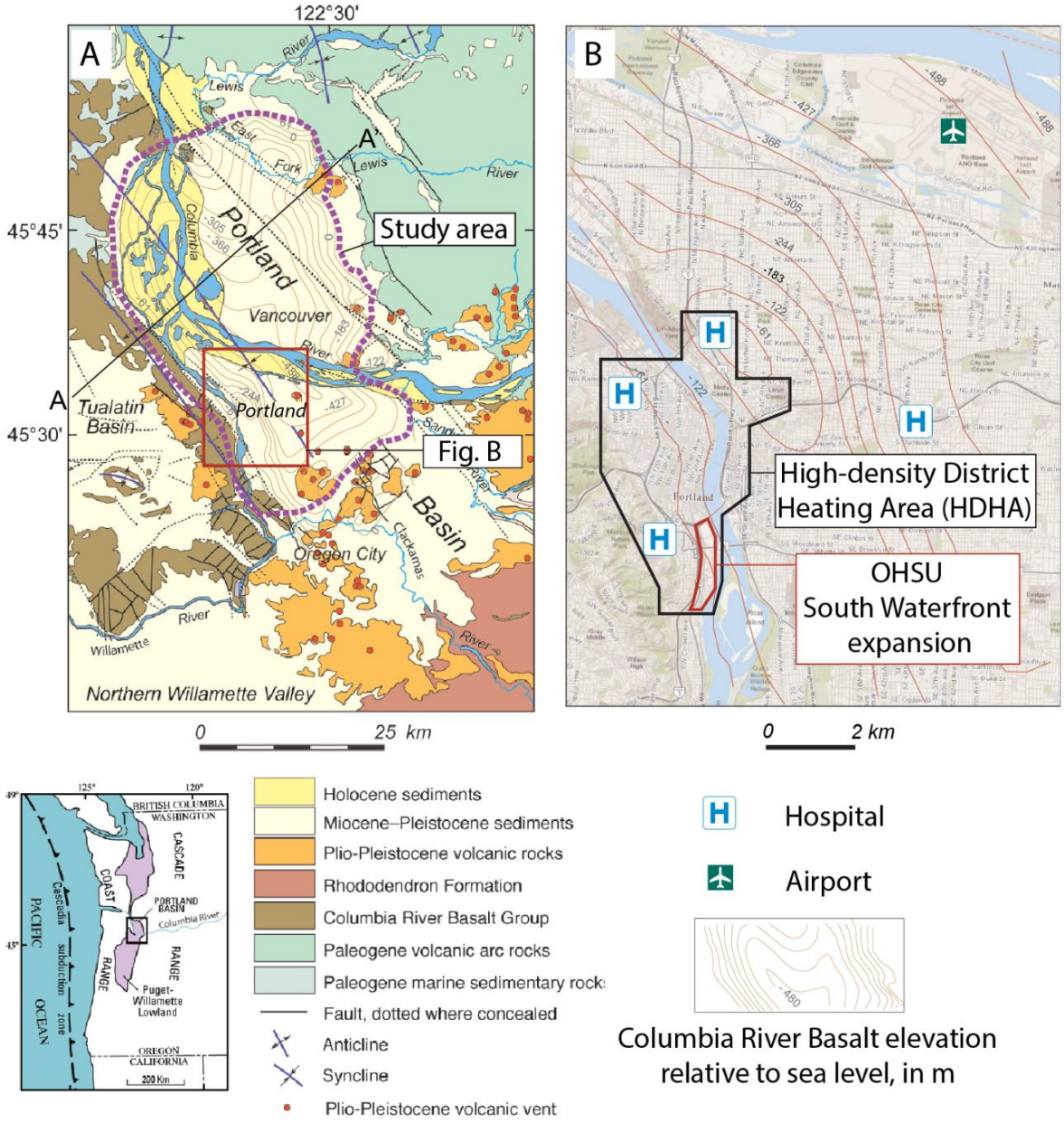

Figure 1. Location maps of study extents with elevation contours of top of the Columbia River Basalt Group. (A) Study area extent for resource map development. Geology is modified from Evarts et al. (2009). A-A' is an approximate location for the generalized cross-section in Figure 1. (B) Focus area inset map shows a high-density area where RTES might be used for district heating and the Oregon Health and Science University (OHSU) south waterfront expansion area used as the foundation for representative simulations. The south waterfront expansion area is an area where OHSU plans to build 6 new large energy-efficient hospital buildings over the next two decades. The lower small inset map shows regional context of A.

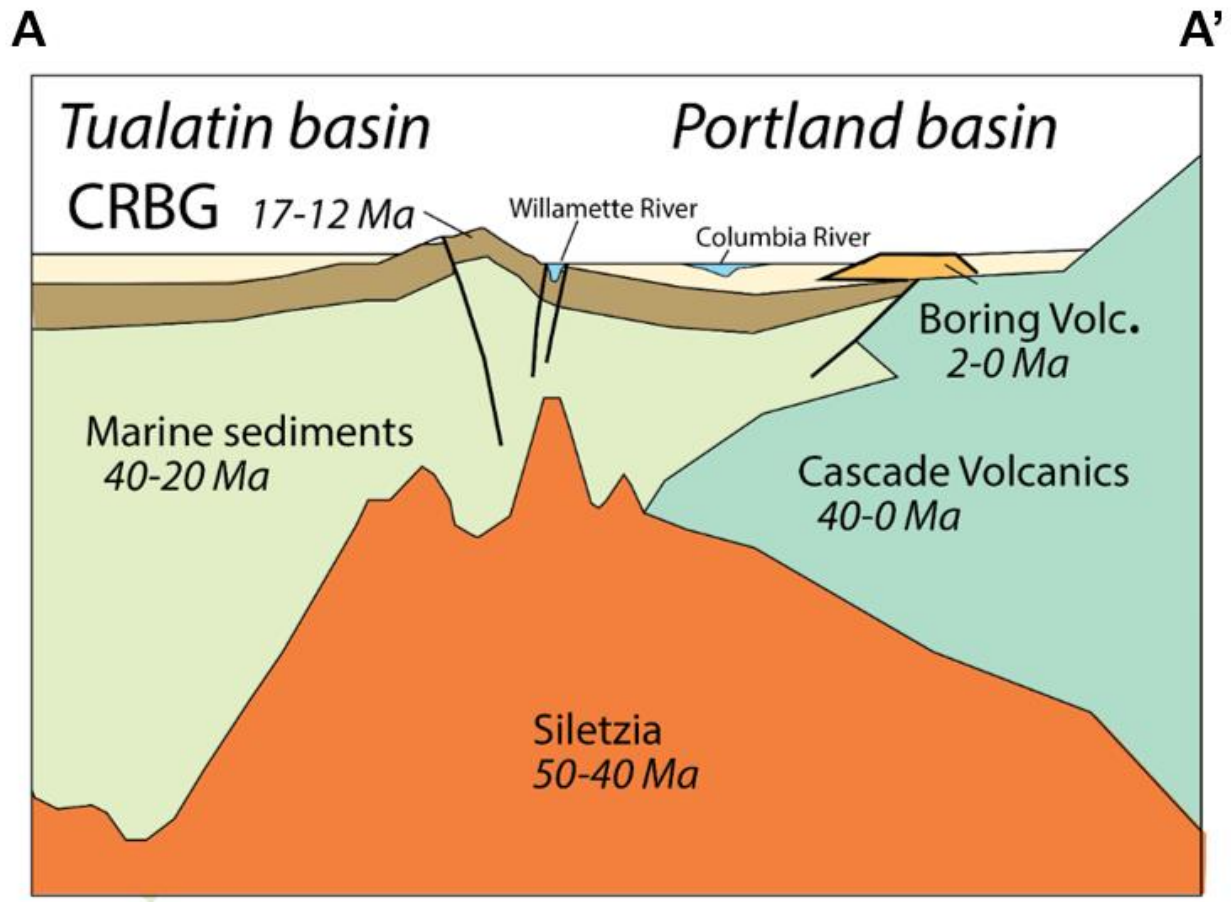

Figure 2. Generalized cross-section of major geologic units across the fore-arc trough that forms the Portland depositional basin (modified from McPhee et al., 2014). The cross-section is generally orthogonal to the NW-SE trending folds and faults shown in Figure 1, and colors match those shown in Figure 1. The Columbia River Basalt Group (CRBG) is the RTES target. In the Portland Basin, the regional aquifer is primarily in the sediments overlying the CRBG. Vertical exaggeration = ~5X.

Portland Basin Geologic Model

We modeled three stratigraphic surfaces (top CRBG, base CRBG, and Eocene basement) using well log, outcrop, seismic, aeromagnetic, and gravity data (**Error! Reference source not found.**). Lithologic data from surficial geology and well logs plays a crucial role in characterizing subsurface geology in areas that lack other types of subsurface data. The majority of water wells for the southern Portland basin are accessed from the Oregon Water Resources Department (OWRD) Groundwater Site Information System (GWIS). The few oil and gas exploration wells available for this study are accessed through the Oregon Department of Geology and Mineral Industries (DOGAMI) oil and gas index. Geologic interpretations of lithologic logs are accessed through the USGS CRBG stratigraphy database. All surfaces modeled and supporting data are available online in the Geothermal Data Repository (https://gdr.openei.org/).

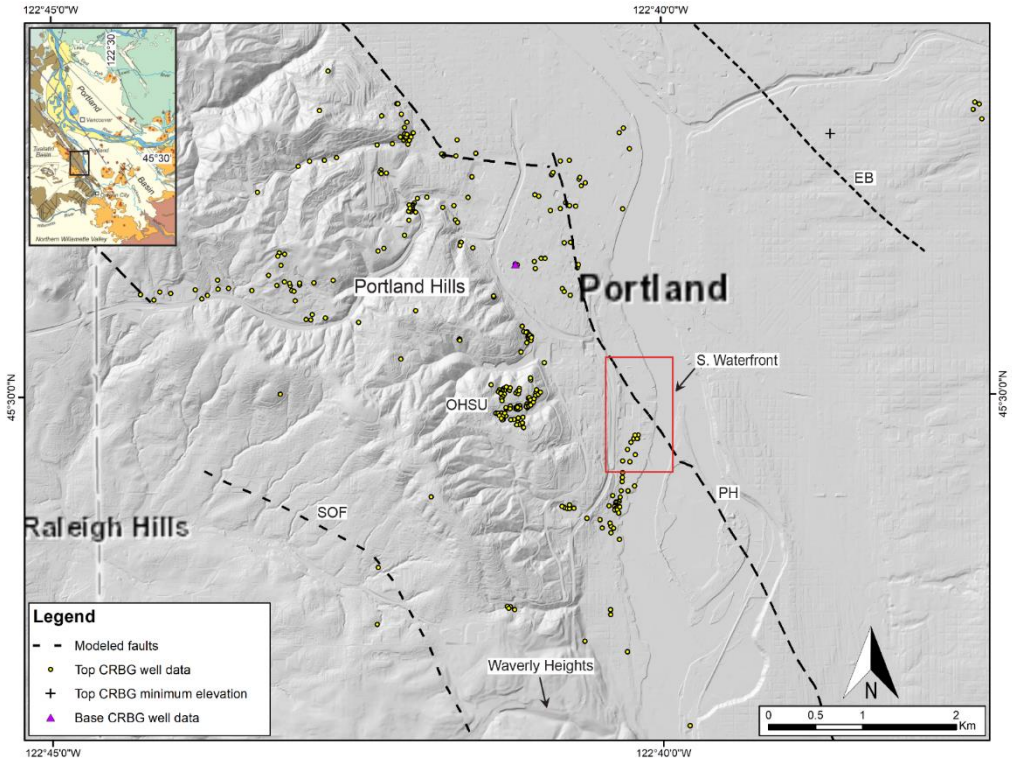

Figure 3. Data control for top and base CRBG structure (surface) maps. OHSU – Oregon Health & Science University; SOF – Sylvan –Oatfield fault; PH – Portland Hills fault; EB – East Bank fault.

Geologic field relations and schematic cross sections suggest that CRBG unconformably overlies Eocene basement of Waverly Heights south of the area of interest (Beeson et al., 1989; Wells et al., 2018; Wells et al., 2019). In the south waterfront area, the top of CRBG steadily decreases in elevation eastward from 200 ft to ~ -100 ft toward the center of the Portland basin (Figure 5). This steady decrease in elevation is consistent with traversing down the limb of an anticline (i.e., the Portland Hills). The base of CRBG in the south waterfront area decreases eastward from -225 ft to ~ -800 ft. The uncertainty of this surface is higher than for top CRBG, as it is derived from far fewer data points (i.e., PSU injection well, Waverly Heights outcrop). The gravity derived Eocene basement surface provides a better estimate of base CRBG elevations in the area of interest, assuming the unit unconformably overlies basement. The predicted depth to Waverly Heights from the depth to basement model agrees with depth encountered in the PSU injection well.

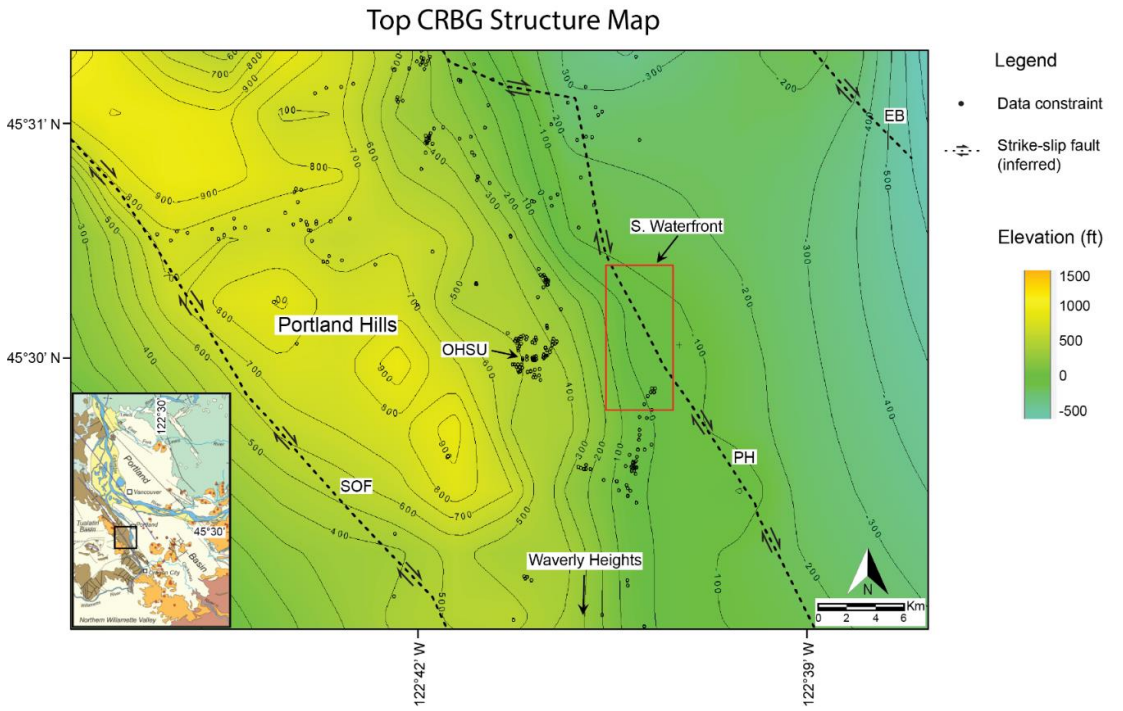

Figure 4. Structural contour map of base CRBG. Contour interval = 100 ft. OHSU – Oregon Health & Science University; SOF – Sylvan-Oatfield fault; PH – Portland Hills fault; EB – East Bank fault.

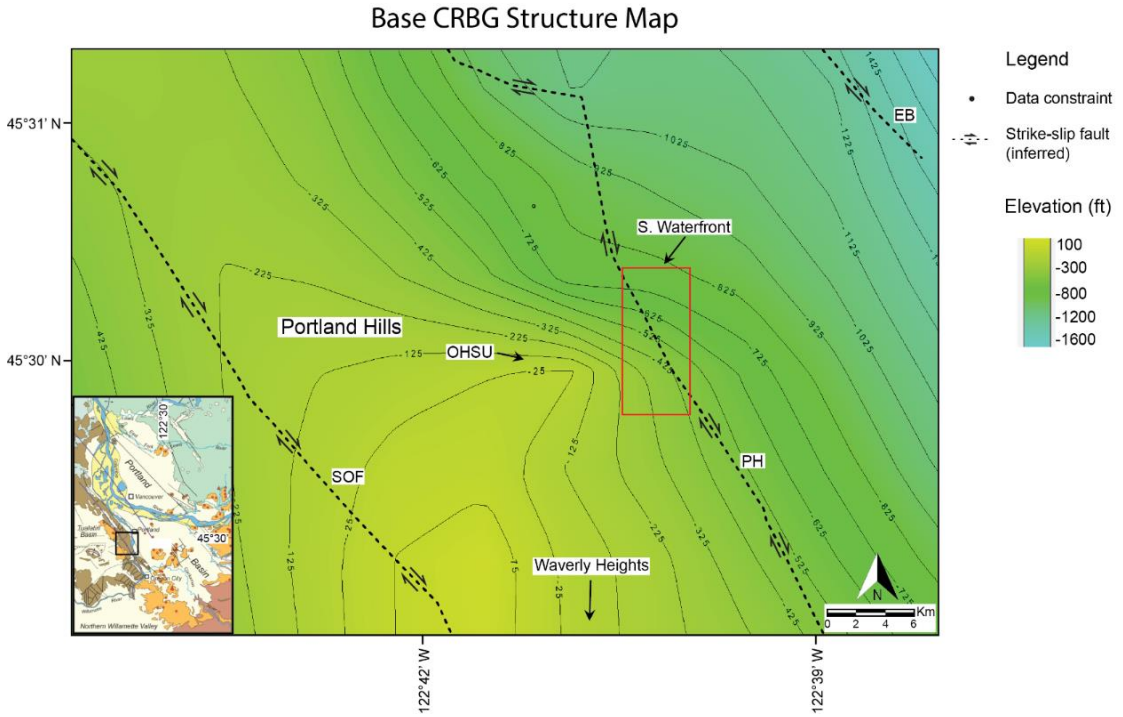

Figure 5 Structural contour map of top CRBG. Contour interval = 100 ft. OHSU – Oregon Health & Science University; SOF – Sylvan-Oatfield fault; PH – Portland Hills fault; EB – East Bank fault.

Eocene basement decreases from -500 ft to ~ -1,000 ft in the south waterfront area. Three proposed well locations are depicted on the schematic cross section in Figure 6, and their depths to top and base CRBG are listed in Table 1. Measured depths to energy storing strata decrease southward across the south waterfront area. The proposed wells cross the inferred trace of the Portland Hills fault. Motion on this fault is thought to be taken up in dextral strike-slip motion, with a component of dip-slip (Blakely et al., 1995).

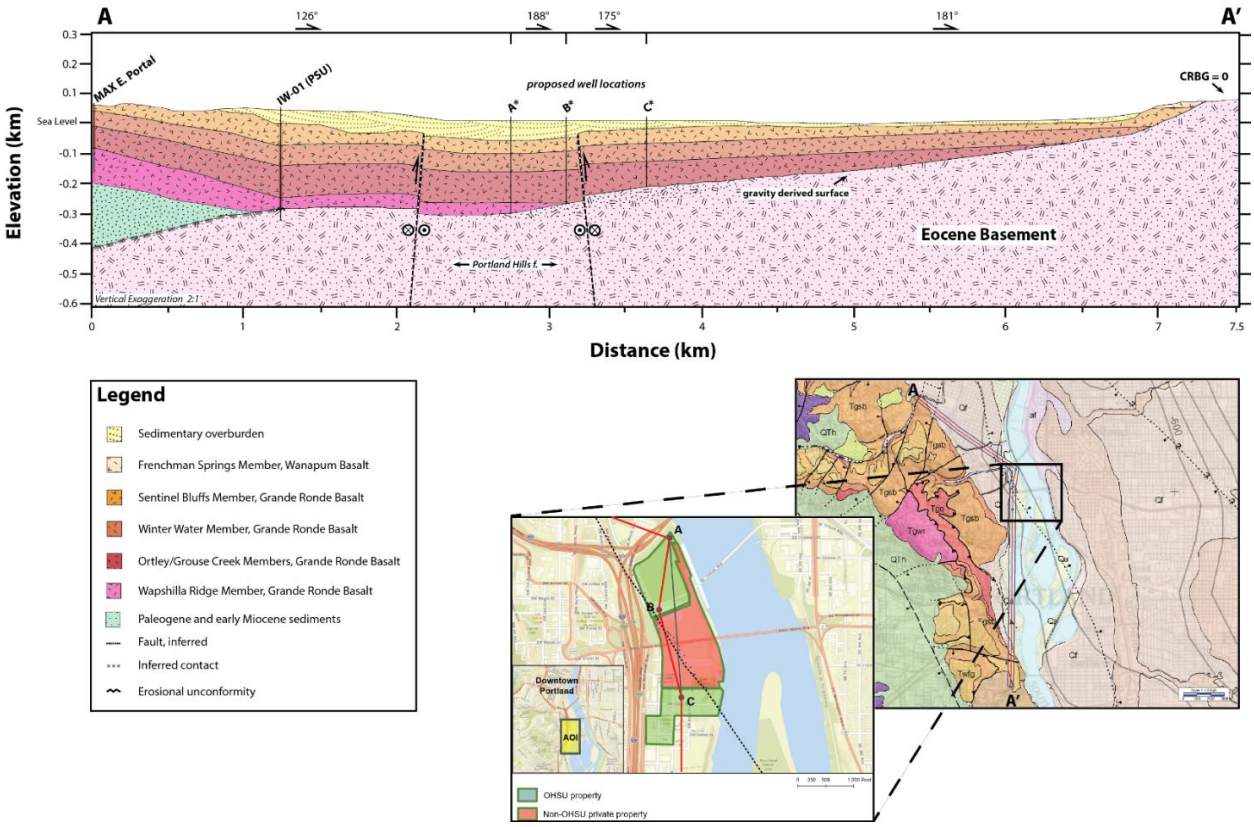

Figure 6 Schematic cross section A-A' through proposed well locations in the south waterfront area of the Portland basin. Azimuth directions denote cross section line orientation relative to north (0°/360°). Inset: Regional geologic map from Wells et al., 2018; Wells et al., 2019; AOI – area of interest (S. Waterfront).

Table 1 Cross-section derived elevation and measured depths (MD) for proposed well locations.

Well	Surface elevation (ft)	Top CRBG MD (ft)	Base CRBG MD (ft)
A	26	204	946
B	36	99	836
C	36	73	714

Major faults in the southern Portland basin are modeled as sub-vertical planes. The fault of interest near the south waterfront area is the Portland Hills fault, which is modeled down to a gravity derived basement surface (Eocene basement) (McPhee et al., 2014). A perspective view of the model looking northwest (Figure 7) shows the south waterfront area with the Portland Hills fault and nearby major faults integrated.

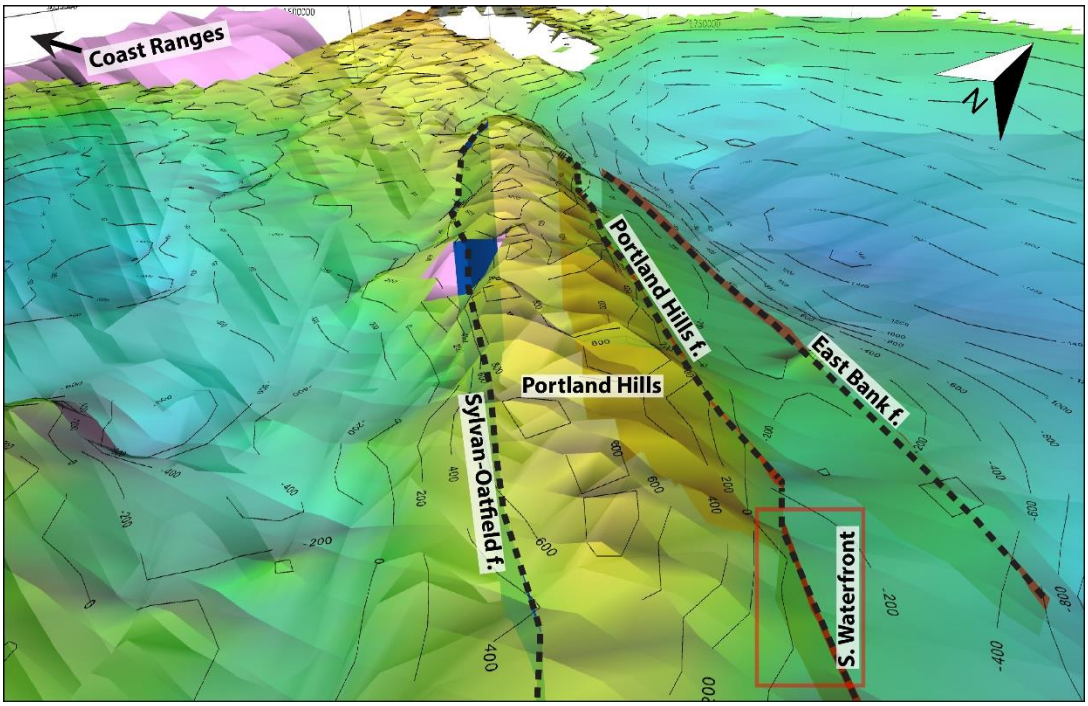

Figure 7. Perspective view looking northwest near the south waterfront. Top CRBG surface (colored and countoured) is shown overlying Eocene basement. Major faults can be seen as sub-vertical planes underneath the surface. Contour interval = 200 ft.

1.2 Seismic and Structural Hazards Analysis

Compilation of Faults and Seismicity

We compiled data on faults from the US Geological Survey Quaternary Fault and Fold Database (QFFD). along with a few bedrock faults mapped by Wells et al. (2018, 2019). Primary information about these seismic sources are provided in Table 2, and a more comprehensive database of fault characteristics is provided in the Appendix (Table A1). We used earthquake focal mechanisms to evaluate fault dip and estimate the seismogenic depth of some

Table 2. Summary of Fault Characteristics for faults included in the Seismic Source Characterization

Fault	Dip Direction	Dip Angle	Sense of Movement	Length (km)	Age (QFFD)
Beaverton	South	70°	Reverse	15	Middle and late Quaternary

Bolton	West	70°	Reverse & right-lateral strike slip	9	Class B (Various age)
Canby-Molalla	Northeast	70°	Right-lateral	51	Late Quaternary
East Bank	Northeast	70°-90°	Reverse & right-lateral strike slip	55	Middle and late Quaternary
Gales Creek	West	70°-90°	Reverse & right-lateral strike slip	73	Undifferentiated Quaternary
Helvetia	West	70°	Reverse & right-lateral strike slip	10	Undifferentiated Quaternary
Lackamas Lake	Southwest	70°	Normal & right-lateral strike slip	44	Middle and late Quaternary
Mount Angel	Northeast	60°-70°	Reverse & right-lateral strike slip	32	Latest Quaternary
Newberg	Southwest	70°	Reverse	8	Undifferentiated Quaternary
Oatfield	Northeast	70°	Reverse & right-lateral strike slip	40	Undifferentiated Quaternary
Portland Hills	Southwest	70°	Reverse & right-lateral strike slip	62	Undifferentiated Quaternary
Sherwood	South	50°	Reverse	14.5	N/A (from bedrock faults)

faults with historical microseismicity (<M4 earthquakes), these data are provided in the Appendix (Table A2). We used empirical scaling relationships for fault length and type of displacement to estimate the maximum magnitude (Mmax) earthquake and Average Lateral Displacement (AD) faults included in the seismo-tectonic model are capable of generating (Table 3) (Wells and Coppersmith, 1994; Hanks and Bakun, 2002). Figure 8 shows surface displacements resulting from a scenario 1.5 m right lateral slip on the Portland Hills fault (Table 3), from a Coulomb stress model (Coulomb 3.3; Toda et al., 2011).

Risk to Infrastructure

We provide a review of existing scenario ground shaking maps for the Portland Metropolitan region for both local crustal fault rupture and a subduction zone earthquake. For a crustal fault rupture like a scenario M 6.8 earthquake on the nearby Portland Hills fault the

Table 3. Maximum magnitude earthquake and average displacement calculated for fault lengths and depths. Fault depths calculated from focal mechanisms for some faults, and where there was no focal mechanism information, the maximum and minimum depths of the seismogenic crust were estimated at 20-25 km.

						Maximum Magnitude Earthquake (M)					**Average Displacement (AD)**
						Wells and Coppersmith (1994)			Hanks and Bakken (2002)		Wells and Coppersmith (1994)
						Strike-slip	Reverse	Normal	All		Strike-Slip
	SRL	Min	Max	Min	Max	**M** = 5.16 + 1.12 * log (**SRL**)	**M** = 5 + 1.22 * log (**SRL**)	**M**=4.86+1.32* log(**SRL**)	**M** = (4/3) * log(**A**) + 3.07 +/- 0.04		log(**AD**) = -1.7 + 1.04 * log (**SRL**)
Fault	**Length (km)**	**Depth (km)**	**Depth (km)**	**Area (km3)**	**Area (km3)**				Min	Max	
Beaverton	15	20	25	300	375	6.5	6.4		6.4	6.5	0.3
Bolton	9	20	25	180	225	6.2	6.2		6.1	6.2	0.2
Canby-Molalla	51	20	25	1020	1275	7.1	7.1		7.1	7.2	1.2
East Bank	55	20	25	1100	1375	7.1	7.1		7.1	7.3	1.3
Gales Creek	73	20	25	1460	1825	7.2	7.3		7.3	7.4	1.7
Helvetia	10	20	25	200	250	6.3	6.2		6.1	6.3	0.2
Lackamas Lake	44	20	25	880	1100	7.0		7.0	7.0	7.1	1.0
Mount Angel	32	20	25	640	800	6.8	6.8		6.8	6.9	0.7
Newberg	8	20	25	160	200	6.2	6.1		6.0	6.1	0.2
Oatfield	40	20	25	800	1000	7.0	7.0		6.9	7.1	0.9
Portland Hills	62	20	25	1240	1550	7.2	7.2		7.2	7.3	1.5
Sherwood	14.5	20	25	290	362.5	6.5	6.4		6.4	6.5	0.3

proposed RTES study site is expected to experience between 0.7 to 0.75 g acceleration and Modified Mercalli Intensity IX Violent shaking (Table 4) (Bauer et al., 2018). A 2018 report (Bauer et al., 2018) reveals high horizontal accelerations and shaking intensity for this scenario, this 2018 publication uses the latest mapping and earthquake modelling to improve potential earthquake impacts for the Portland metropolitan region. An earlier study by Wong and others (2000) found a lower range of 0.5 – 0.6 g acceleration for this area, and lower Modified Mercalli Intensity shaking of VIII, Severe shaking (Table 4). A Portland Hills fault earthquake could cause roughly 1 minute of ground shaking.

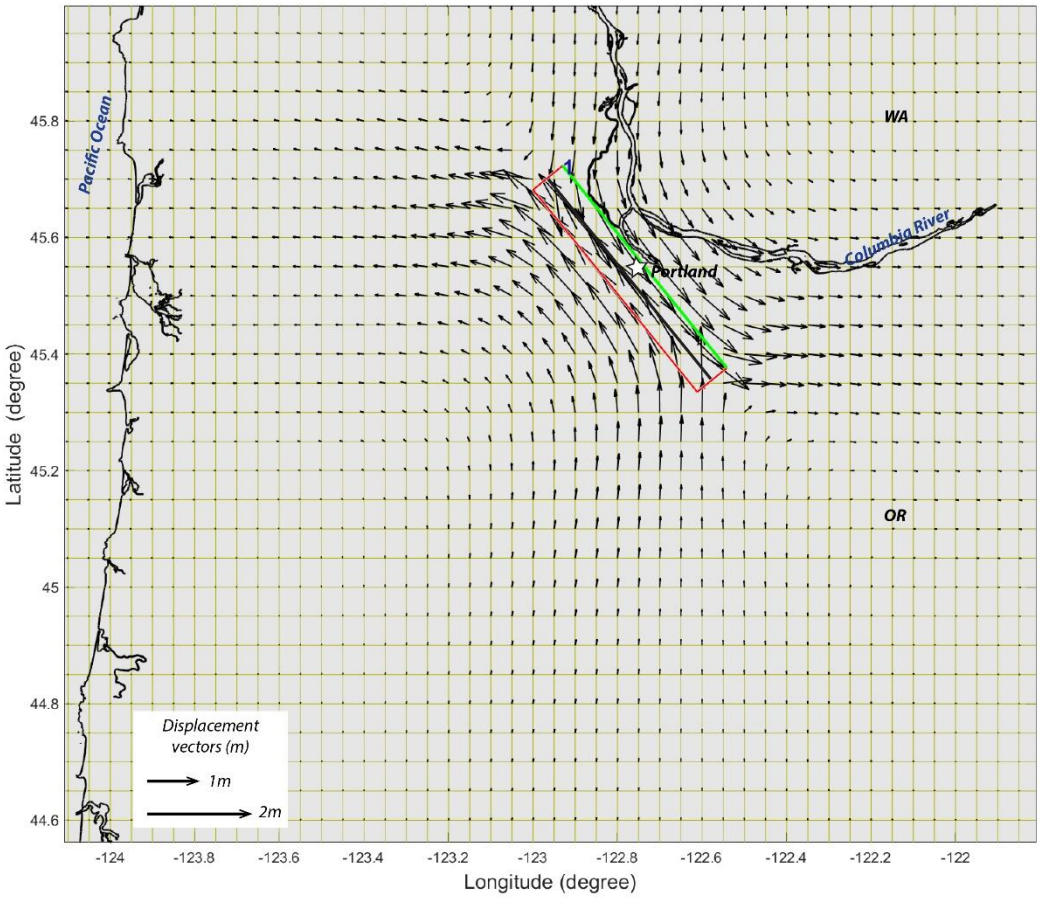

Figure 8. Surface displacements resulting from a scenario 1.5 m right lateral slip on the Portland Hills fault (Table 3), from a Coulomb stress model (Coulomb 3.3; Toda et al., 2011). The Columbia river is shown in black, the Portland Hills fault is shown as a single fault source bound by a red and green rectangle, black arrows show horizontal displacement vectors surrounding the fault.

A scenario M 9.0 subduction zone earthquake would generate > 3 to as much as 6 minutes of shaking and would result in peak horizontal acceleration of 0.25 to 0.30 g (Table 4) (Bauer, et al., 2018). Shaking would be severe, Modified Mercalli Intensity VIII (Table 4) (Bauer, et al., 2018). For this scenario earthquake, the likelihood of permanent ground deformation for saturated soil is very high, from 100 – 1,180 cm of permanent deformation (Table 4). Deformation at the proposed area of the RTES thermal storage injection well locations on Willamette waterfront OHSU property includes liquefaction and lateral spread. Permanent ground deformation should be anticipated in the event of either a crustal fault or subduction zone earthquake, and appropriate well shut off systems should be in place to ensure system shut down in the event of ground failure. Geotechnical investigations should be completed in future phases of this project to evaluate site specific liquefaction and lateral spread susceptibility and evaluate potential for engineered ground improvement to minimize this risk.

Table 4. Summary of Ground Acceleration, shaking intensity, and liquefaction susceptibility for the proposed RTES thermal storage site.

Earthquake Type	Peak Horizontal Acceleration (g)	Modified Mercalli Intensity	Permanent Ground Deformation (cm) for saturated soil	Reference
Crustal fault: Scenario Portland Hills Fault M 6.8 earthquake	0.5 - 0.6	VIII, Severe shaking		Wong et al., 2000
Crustal fault: Scenario Portland Hills Fault M 6.8 earthquake	0.7 - 0.75	IX, Violent		Bauer et al., 2018
Subduction Zone: Cascadia M 9.0 earthquake	0.25 - 0.30	VIII, Severe shaking	Very high; 100 - 1,180 cm	Bauer et al., 2018

Induced Seismicity

We evaluate geologic conditions and model parameters for injection rates, volume, and water injection depth. We compiled rates, volumes and depths of injection for local aquifer storage and recovery wells and also injection wells and regulations associated occurrences of induced seismicity in the United States and Switzerland. We compare proposed depths and rates of injection for the proposed RTES in Portland, OR with compiled values and find the proposed system falls below the range of values for nearby operating aquifer storage and recovery wells which are shallow, have low injection and withdrawal rates, and have not been historically associated with occurrences of induced seismicity in the Portland region (Figure 9).

Table 5. Proposed injection rates and depths for RTES

Well Location	Injection Rates (gallons per minute)	Injection Volume per day (gallons)	Injection Volume per month (gallons)	Depth of injection (feet)	Source
South Waterfront	~50 gallons per minute	~72,000 gallons per day	~2,160,000 gallons per month	Columbia River Basalt Group – 800-950 ft.	Section 3.2 of this report

Table 6. Injection wells in downtown Portland. Injection volume per month calculated from average injection rates for a 30-day month.

Well Location	Injection Rates (gallons per minute)	Injection Volume per day (gallons)	Injection Volume per month (gallons)	Depth of Injection (feet)	Notes	Source
Southwest Portland Business district	100-1500 gallons per minute, with average 300-600 gallons per minute	648,000 gallons per day	19,440,000 gallons per month	Troutdale: 250-300 ft. Basalt: 350-1,000 ft.	No induced seismicity in the area	Gannett, 1985
Portland State University	500 gallons per minute	720,000 gallons per day	21,600,000 gallons per month	Drilled to 1,200 ft.	No induced seismicity in the area	Fortis Construction, 2009

For the purpose of this project, the base of the CRBG at a depth of 800-950 ft is the proposed RTES water storage target, and is used as the proposed injection depth for this project. We use a baseline injection rate of 50 gallons per minute (72,000 gallons/day), and estimated volume injected of 2,160,000 gallons per month (for an average 30-day month) (Table 5).

Regional Wells

Two injection wells are located in downtown Portland in the Portland Business District and at Portland State University, < 2 km northwest of the proposed OHSU RTES site (Figure 9). These wells inject water to depths less than 1,200 feet and have injection rates less than 1,500 gallons per month (Table 6). No historical seismicity is associated with water injection in these wells. Injection depths in these wells are comparable to our proposed target injection depth for this project, the fluid injection rates are higher than our proposed RTES thermal storage system (Figure 10). Table 7 is a compilation of water injection data from aquifer storage and recovery (ASR) systems in Beaverton, OR, adjacent to the Portland Basin (Figure 9). Here, fluid injection depth is shallower than our proposed project, though injection rates and volumes are much higher than what we are proposing for the OHSU RTES wells (Figure 10; Table 5). These ASR wells are operating ~ 30 km west of the proposed OHSU RTES study site, in the same regional stress regime and no historical seismicity is associated with water injection in these wells.

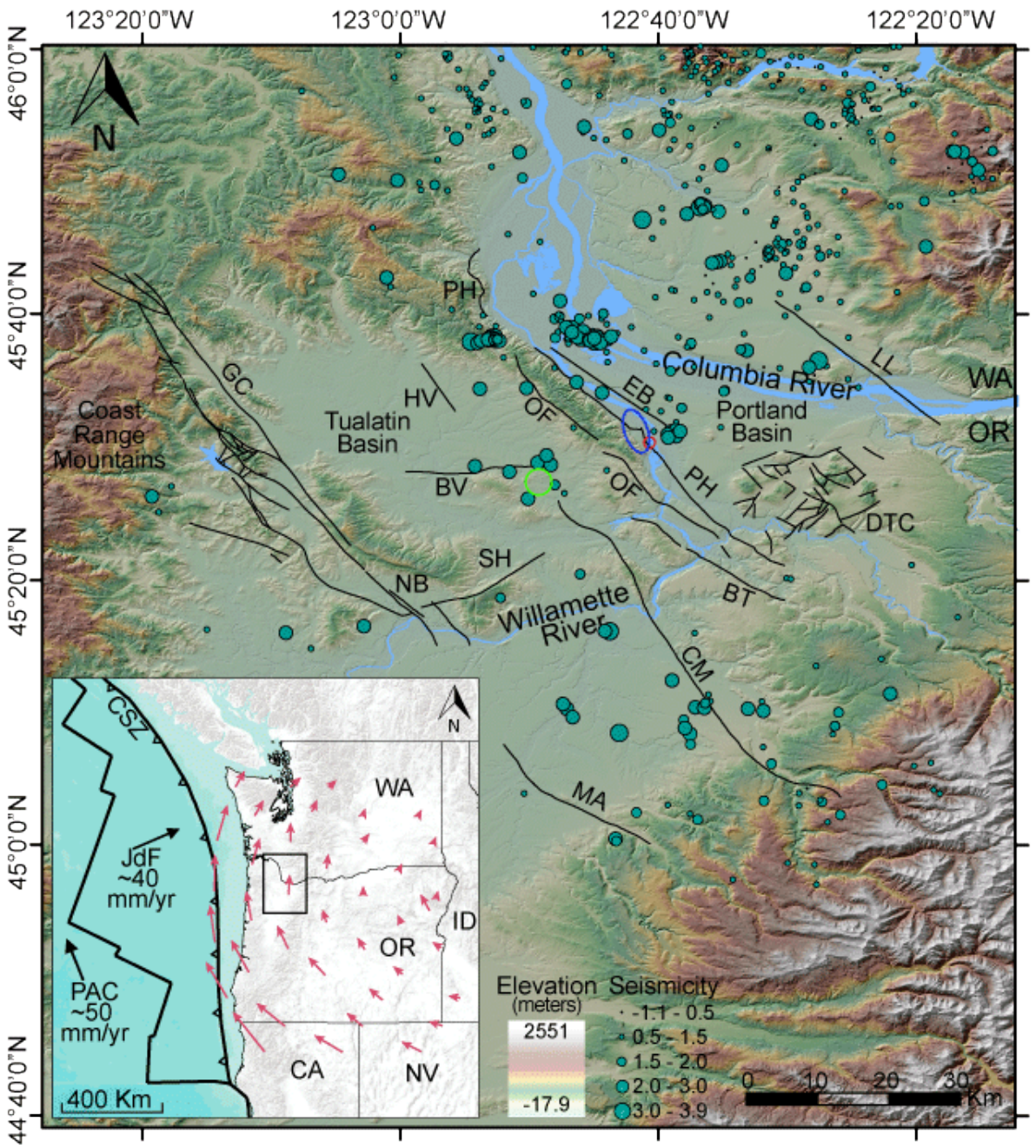

Figure 9. Regional physiographic map of the Portland and Tualatin Basins, Quaternary active faults, and microseismicity, elevation draped over hillshade. The proposed RTES site is shown by a red circle, location of wells in downtown Portland from Table 6 are shown by blue circle and ASR well locations, Table 7 are shown by the green circle. Microseismicity from the Pacific Northwest Seismic Network (University of Washington, 1963). Locations for all faults except Gales Creek and Sherwood are from Quaternary Fold and Fault Database (US Geological Survey, 2006); Gales Creek and Sherwood faults mapped by Wells and others (2017). Faults labeled: GC: Gales Creek, BV: Beaverton, SH: Sherwood, MA: Mount Angel, CM: Canby-Molalla, BT: Bolton, OF: Oatfield, EB, East Bank, PH: Portland Hills, LL: Lackamas Lake, and DTC: Damascus-Tickle Creek (DTC shown on map but not included in seismic source characterization due to lack of data on the fault). (Inset) Tectonic setting of Pacific Northwest United States with block model velocities from GPS (pink arrows) relative to a stable North America (McCaffrey et al., 2013). Arrows show inferred long-term motion after subtracting deformation due to locking on the Cascadia megathrust. Cascadia Subduction zone labeled CSZ, Juan de Fuca (JdF) and Pacific (PAC) plates and rates of motion shown with arrows and GPS surface velocity.

Table 7. Injection rates and depths from aquifer storage and recovery wells in Beaverton, OR.

Cycle	Well #	Injection Rate	Cycle Period	Total Volume Injected (gallons)*	Average Total Volume per Month for 1 well (gallons)**	Depth of Injection (feet)***	Source
1 (1999)	W1	618 gallons per minute	2 days	1,700,000 gallons	25,500,000 gallons per month	~330 feet	Eaton and Melady, 2007
2 (1999)	W1	618 gallons per minute	30 days	34,500,000 gallons	34,500,000 gallons per month	~330 feet	Eaton and Melady, 2007
3 (2000)	W1	618 gallons per minute	65 days	74,700,000 gallons	34,583,333 gallons per month	~330 feet	Eaton and Melady, 2007
4 (2001)	W1 W2	618 gallons per minute 972 gallons per minute	4 months	159,100,000 gallons	19,791,666 gallons per month	~330 feet	Eaton and Melady, 2007
5 (2002)	W1 W2	618 gallons per minute 972 gallons per minute	5.5 months	310,500,000 gallons	28,227,272 gallons per month	~330 feet	Eaton and Melady, 2007
6 (2003)	W1 W2	618 gallons per minute 972 gallons per minute	5.75 months	394,600,000 gallons	34,131,043 gallons per month	~330 feet	Eaton and Melady, 2007
7 (2004)	W1 W2	618 gallons per minute 972 gallons per minute	5 months	444,300,000 gallons	44,430,000 gallons per month	~330 feet	Eaton and Melady, 2007
8 (2005)	W1 W1	618 gallons per minute 972 gallons per minute	2.6 months	209,500,000 gallons	40,288,461 gallons per month	~330 feet	Eaton and Melady, 2007
9 (2006)	W1 W2	618 gallons per minute 972 gallons per minute	4.4 months	303,300,000 gallons	34,465,946 gallons per month	~330 feet	Eaton and Melady, 2007

*Provided in Eaton and Melady (2007)

**Calculated from volume injected from Eaton and Melady (2007) and cycle period, for an average 30-day month for one injection well

***Injection depth is based on depth of CRB (Eaton and Melady, 2007; Scanlon, 2019)

Table 8. Oklahoma Regulatory Commission (ORC) Guidelines on Injection rates and Depths, and for wells in regions at risk of induced seismicity

Injection Rates	Volume per day (gallons)	Volume per Month (gallons)	Depth of Injection (feet)	Notes	Source
ORC Maximum Value					
<5,000 barrels per day	210,000 gallons per day (146 gallons per minute)	6,300,000 gallons per month	200 feet for injection of <1000 barrels per day 500 feet for injection of >1000 barrels per day	If 1,000 barrels per day or less, there must be an overlying strata of at least 200 feet thickness between lowest base of fresh water and top of proposed interval of injection to be considered fresh water protection sufficiency. If greater than 1,000 barrels, there must be at least 500 ft. in thickness	The Oklahoma Register, 2018

Table 9. Injection Well data from Oklahoma and Kansas

Oklahoma (2015)			
Example Well	**Volume**	**Notes**	**Source**
1	68,003,574 gallons per month	Maximum volume to date (for a single class II injection well)	Auch, 2016
2	6,837,211,907 gallons per month	Total volume to date	Auch, 2016
3	625,717 gallons per month	Mean volume to date	Auch, 2016
Kansas (2015)			
Example Well	**Volume**	**Notes**	**Source**
1	28,927,845 gallons per month	Maximum volume to date (for a single class II injection well)	Auch, 2016
2	3,401,229,017 gallons per month	Total volume to date	Auch, 2016
3	746,701 gallons per month	Mean volume to date	Auch, 2016

Fluid Injection and Induced Seismicity

Fluid injection can trigger earthquakes if pore pressure at a fault increases beyond a critical pressure threshold (Keranen et al., 2013). Wastewater in Oklahoma is being injected at great depths into the crystalline basement, and as a result induces slip on basement faults causing seismicity. We compiled information on wastewater regulation for disposal wells in Oklahoma by the Oklahoma Regulatory Commission (Table 8). These types of regulations are the responsibility of the US EPA, though frequently permitting authority is delegated to state agencies (McGarr et al., 2015). In recent decades, there has been an increase in earthquakes in the central United States, which has been linked with oil and gas wastewater fluid injection in these regions (Rubinstein and Mahani, 2015). In Oklahoma, three > M 5 earthquakes have occurred in injection areas that experienced an increase in both the number of injection wells and injection rates (Table A3) (Hincks et al., 2018). These include the M 5.8 Pawnee, M 5.1 Fairview, and M 5.6 Prague earthquakes (Keranen et al., 2013; Yeck et al., 2016; Barbour et al., 2016; Goebel et al., 2017). In these regions fluids are injected to depths of 6,000 – 11,000 feet, to avoid contamination of groundwater (Keranen et al., 2013; Yeck et al., 2016; Barbour et al., 2016; Goebel et al., 2017; University of Southampton, 2018). In response to the earthquakes, the Oklahoma Corporation commission released a summary of new guidelines for injection wells

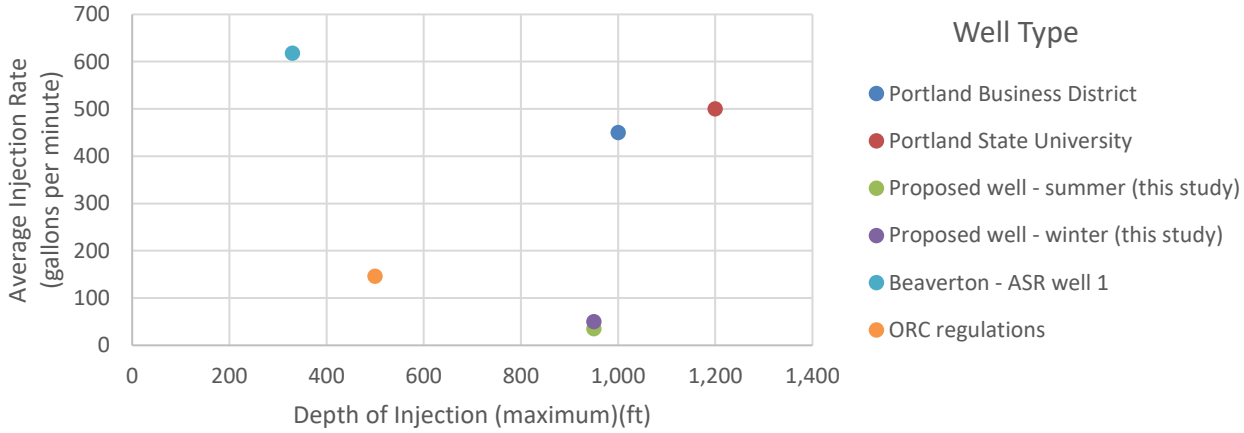

Figure 10. Plot of depth of fluid injection versus average injection rate for several injection well types.

that requires operators to prove injection depths do not extend to basement lithology depths (Hincks et al., Oklahoma Corporation Commission directive, 2015). Table 9 lists injection volumes in Oklahoma and Kansas. Injection rates where these earthquakes occurred in Oklahoma are considerably higher than rates proposed for this study (Figure 11). Injection depths are considerably greater than the depths of the proposed study (Table 5, Table A3).

In Basel Switzerland seismicity was induced by fluid injection into hot dry rock at crystalline basement depths of ~16,400 feet. Basel, Switzerland is located on a historically active fault that generated a M 6.5 earthquake in 1356 CE, and that destroyed the city. Earthquakes began with the onset of fluid injection, steps were taken to relieve pressure in the wells, and injection was halted within 6 days of the initial injection. The region experienced 200 earthquakes between M 0.7 and 3.4 Dyer et al., 2007. Fluid injection for this enhanced geothermal system remains suspended. The injection depth for this system far exceeds the depths of our proposed project and other regional wells (Figure 11).

Proposed Site Considerations

In the Pacific Northwest, seismicity occurs in the upper 10-20 km, the seismogenic crust. The proposed RTES project targets injection depths of less than a kilometer, which is much shallower than depths where regional seismicity is documented. Under a base case scenario, the proposed RTES wells would inject an estimated volume of 2,160,000 gallons per month (for an average 30 day month). For RTES in the Portland Basin, we are proposing two wells that will inject water to the subsurface at rates lower than local aquifer storage and recovery wells in Beaverton, and considerably lower than wastewater injection practices in Oklahoma and Kansas. These wells are relatively shallow (~1,000 feet), and nowhere near basement lithology depths with high pressures and temperatures. We believe our proposed system is operating within safe

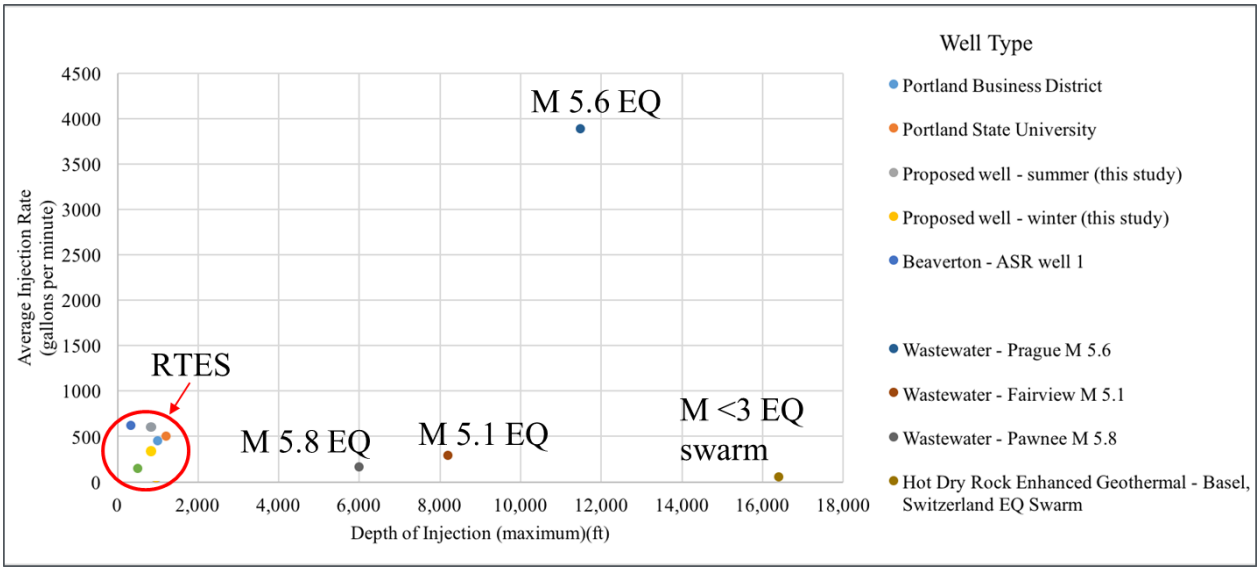

Figure 11. Plot of depth of fluid injection versus average injection rate for several injection well types in regions that have documented induced seismicity.

injection depths and rates for the Portland Metropolitan region given our comparison with regional fluid injection wells and the lack of regional induced seismicity from those injection wells. In addition, RTES operates two wells at the same time, one that is injecting and one that produces from the same reservoir some distance away (>1,500 ft). Thus, the net change in pore pressure is anticipated to be minimal compared to ASR and wastewater injection wells.

However, there are active faults in the region that should be considered in future planning phases that include geotechnical site investigations. For example, the Portland Hills fault is the closest mapped fault to the proposed RTES location, a mapped trace is located 0.25 km to the west (Figure 9) (U.S. Geological Survey, 2006). There are no geophysical investigations near the proposed study area that image the Portland Hills fault at depth, nor are there nearby geological investigations that evaluate displacement on the Portland Hills fault in the last 12,000 years. Our compilation of existing geotechnical studies and seismic source characterization indicates a sub-vertical Portland Hills fault. Given the short distance of the proposed site from the Portland Hills fault, ~0.25 km, further investigation of this fault is warranted prior to development of the RTES system.

1.3 Geochemical Analysis

Groundwater Chemistry

The chemical composition of native CRBG aquifer waters prior to extraction and heating needs to be constrained to determine potential impacts of cyclical hot water injection, storage and extraction in terms of scale build up in piping and heat exchange components, and changes to aquifer porosity and permeability. Identifying an ‘initial’ average groundwater chemical

composition establishes a baseline for comparison with simulated heated and re-injected water compositions and allows for modeling reactions between injected and in-place waters.

The groundwater chemistry data analyzed in this project was compiled from published literature, well logs, and local, state, and federal water quality reports. Groundwater chemistry obtained for >200 wells in and around the Portland Basin were gathered into a hydrogeochemical database for analysis, available online in the Geothermal Data Repository (GDR). While the database largely focuses on wells screened within the CRBG, it also includes wells screened within the overlying Troutdale Formation (alluvial) aquifer and underlying volcanic and marine sedimentary units. The database, and hence our analysis, is limited by a lack of reported data for some key parameters and analytes (particularly the redox state of waters and Al concentrations).

Aqueous speciation and mineral saturation states for the groundwater samples included in the compiled database were calculated using the geochemical modeling programs PhreeqC (Parkhurst, 1995) and Geochemist's Workbench (Bethke, 2008). Calculations were performed using the Lawrence Livermore National Laboratory (LLNL) thermodynamic database (Johnson et al., 2000). The LLNL database was modified using data from the Carbfix database (Aradóttir et al., 2012) to include the following solid phases relevant to low-temperature hydrothermal alteration in the Columbia River Basalts: basaltic glass, plagioclase, olivine, pyroxene, Fe-chlorite, Mg-chlorite, celadonite, Fe-celadonite, mesolite, and stilbite. Equilibrium modeling was used to determine activities of aqueous species, fugacity of gases, and the saturation state of groundwater samples with respect to minerals in the thermodynamic databases.

Calculated saturation indices indicate that western Oregon CRBG groundwaters are, expectedly, undersaturated with respect to the primary basalt phases plagioclase, pyroxene, and basaltic glass. Waters are typically slightly undersaturated to saturated with respect to calcite and other carbonate minerals such as siderite, magnesite, rhodochrosite (Figure 12). They tend to be slightly oversaturated with respect to most SiO_2 phases, except amorphous silica with which they are slightly undersaturated (mean SI of -0.46); this is common in other aquifer types and may indicate that aqueous SiO_2 concentrations are controlled by equilibrium with clays. Groundwater is, on average, oversaturated with respect to both goethite and gibbsite and undersaturated to saturated with respect to amorphous/nanocrystalline hydrous ferric oxide ($Fe(OH)_3$(ppd)). CRBG groundwaters also tend to be oversaturated with respect to clay and zeolite phases, although some groundwaters are slightly undersaturated with respect to certain smectites.

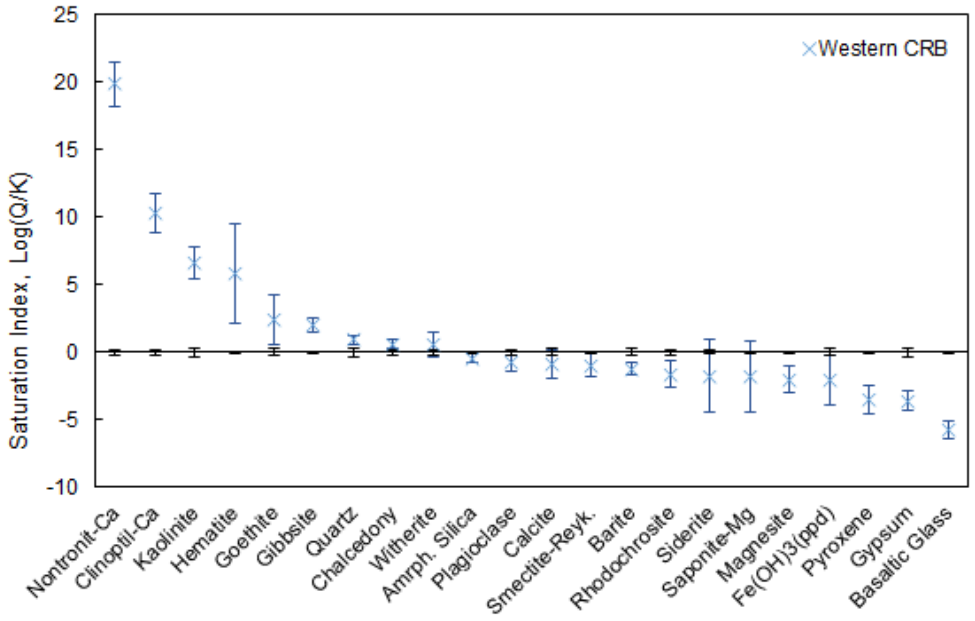

Figure 12. Average saturation indices of minerals with respect to CRBG groundwater in Portland and Tualatin Basins. Error bars are based on the standard deviation of the samples' average SI. Error bars about the origin provide the standard deviation of the SI calculation based on stoichiometry.

Both routine statistics and a Hierarchical Cluster Analysis (HCA) were used to characterize the groundwater chemistries reported in the database. Hierarchical cluster analysis groups samples into distinct populations based on underlying relationships within the dataset. This allows for easier investigation into the relationships between dissolved constituents, spatial distribution, and lithology (Vlassopoulos et al., 2009). HCA was used to identify broad groundwater types within the Portland, Tualatin, and Northern Willamette Valley Basins using all data, including samples from units overlying and underlying the CRBG, as well as data only for CRBG aquifers. Groups range from unevolved recharge water to high TDS saline waters as summarized in Table 10. The average composition of three clusters identified using only CRBG aquifer waters were used as starting points for modeling geochemical changes induced by RTES.

Geochemical plots of water data show that water compositions approach saturation with respect to calcite with increasing depth (Figure 13). The deflection of evolved CRBG waters (CRB3) from the linear trend of Ca+Mg vs total cations (Figure 13) largely reflects calcite precipitation removing Ca from solution with continued weathering of basalts. However, a similar plot of waters from all aquifers (Figure 13) shows some water compositions that are not at or near saturation with respect to calcite fall well to the right of the linear trend. The elevated Na and Cl concentrations in these samples (from Groups 3 and 4) can be explained as mixing of less evolved waters with upwelled saline or brackish waters from underlying, typically marine sedimentary waters (mixing of 10 to 50% Group 6 waters). Mixing models were run using the

Table 10. Groups identified using HCA, ranging from recharge waters to deep saline waters.

Group	Water Type	Description
Clusters identified using compositions of groundwaters sampled from CRBs, Troutdale Formation, & underlying marine sediments		
1 ●	Recharge	Recharge water, consisting of unevolved Troutdale and CRB. Characterized by low TDS (<300 mg/L)
2 ●	Evolving recharge	More evolved Troutdale and CRB water that has not experienced mixing with brackish water. Contains lower Na:Ca ratios
3 ●	Unevolved, mixed waters	Less evolved CRB water that has been influenced by mixing with brackish water. Low TDS, but increased Na to Ca concentrations
4 ●	Mature, some mixing	More evolved CRB water that has mixed with brackish water. Characterized by higher TDS and widely scattered Na:Ca ratios
5 ●	High sulfate	Older, evolved CRB and tertiary marine sediment waters, with high SO_4 concentrations (average of 87 mg/L SO_4)
6 ●	Brackish	Brackish water that has migrated upwards, characterized by high Na:Ca and average TDS > 1,000 mg/L
7 ●	Saline	Older, saline water from marine sediments and basement volcanics. Contains very high TDS (average >10,000 mg/L)
Clusters identified using compositions of groundwaters sampled only from CRB units.		
CRB1 ●	Recharge	Low TDS recharge water, undersaturated with respect to calcite.
CRB2 ●	Evolving CRB	More evolved CRB still undersaturated with respect to calcite, but with elevated bicarbonate and cation concentrations.
CRB3 ●	Mature CRB	Mature, high TDS deep CRB waters. At equilibrium with respect to calcite.

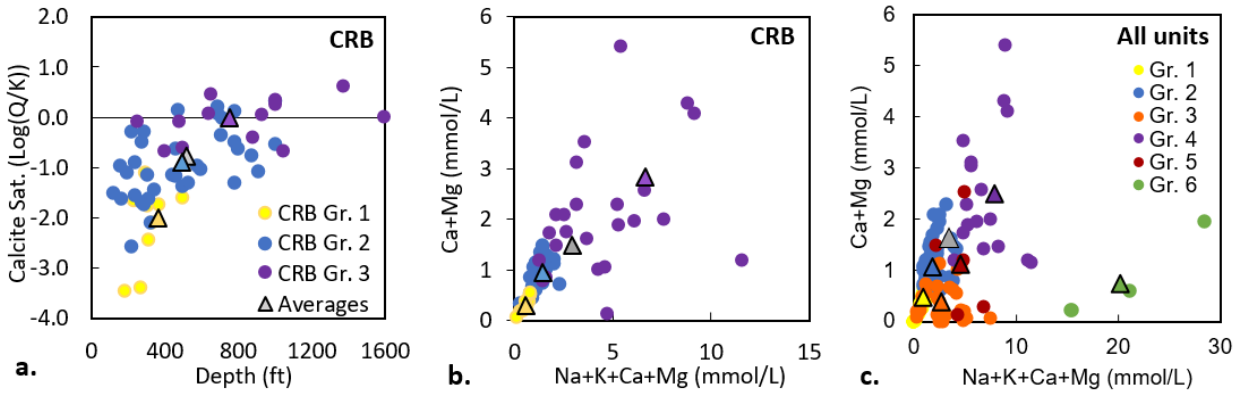

Figure 13. a) Calcite saturation of CRBG groundwaters by group with depth, b) Ca and Mg versus the sum of major cations for samples from the CRBG, and c) Ca and Mg versus the sum of major cations for all hydrogeologic units. Triangles represent the average composition of each group. Cluster group 7 points not shown to highlight differences in less saline waters.

Geochemist's Workbench Smart Mix option in the Geochemist's Spreadsheet application. End members and mixing results are provided in the Geothermal Data Repository (Svadlenak, 2019, Appendix A, Table A-5).

Mixing could be enabled by Holocene active faulting in the Portland Basin (Horst, 2019), as many apparently mixed waters are located near faults within the basin. Additionally, Group 6 wells are high in sodium, chloride, and other dissolved solids, and are located along a northwest-southeast trend, at the base of the Chehalem mountains and between the Gales Creek Fault to the north and the Mount Angel Fault to the south (Figure 14). The Gales Creek and Mount Angel fault systems are connected by the Gales Creek–Mount Angel Structural Zone (Reidel et al., 1989). Deeper groundwater may be upwelling along the fault planes and mixing with shallow groundwaters in this location. Upwelling would explain why a well that taps the shallow Troutdale aquifer (TB-TR-2) contains such brackish water, and faulting provides an explanation for the presence of Tertiary marine sediments in relatively shallow wells (TB-M-3 and TB-M-10, in Svadlenak, 2019, Appendix A Table A-1, uploaded to the GDR).

RTES will likely source its water from deeper CRBG aquifers present in the Portland Basin. Because there is little published data regarding the water composition in the lower CRBG, and because groundwater compositions may vary depending on depth, proximity to structures, and location within the basin, our geochemical reaction models use a range of potential native compositions based on the means of groups identified via HCA (Table 11). These include: shallow / minimally evolved CRBG waters (CRB1), evolved CRBG waters (CRB2), mature/mixed CRBG waters that are at or near saturation with respect to calcite (CRB3), sedimentary waters (basin-wide Avg 6), and brackish to saline Na-Cl-type marine sedimentary or volcanic ("basement") waters (basin-wide Avg 7). Water compositions representative of the underlying units, represented by HCA Groups 6 and 7 (Avg 6 and Avg 7) are included because there is interest in using these units as storage sites in addition to the CRBG aquifers. An "average" CRBG groundwater composition (CRB_Avg) was also calculated from all CRBG groundwater data. The resulting composition approximates the samples that fall at the end of the Ca-Mg linear trend in Figure 13 (gray triangles).

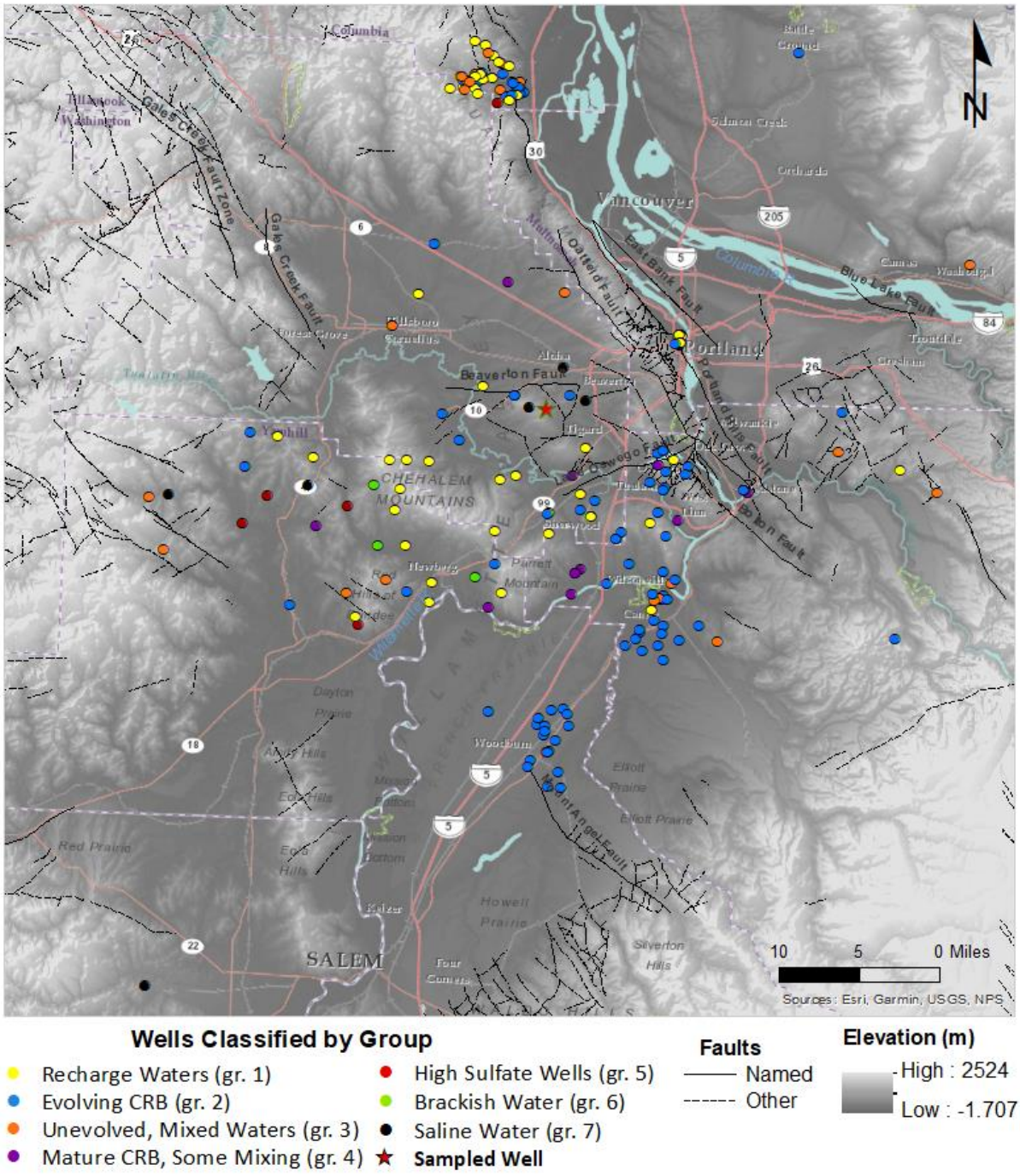

Figure 14. Western Oregon well locations, color coded by groundwater group. Lines represent faults. Note that group 6 wells (in green) are shallow wells with a brackish water chemistry that plot directly within the Gales Creek – Mount Angel Structural Zone.

Table 11. Average water compositions for cluster groups used in geochemical reaction models. [1]Aluminum concentrations available for only 6 CRB groundwater samples; same value use for all groups. [2]Eh or pe values available for only 14 CRB groundwater samples; same value used for all CRB groups.

Cluster Group:	Unit	CRB 1	CRB 2	CRB 3	CRB Avg.	Avg. 6	Avg. 7
Count	--	11	43	24	78	4	7
Well Depth	ft.	370	490	750	530	200	3080
Temperature	°C	11.3	11.2	14.4	12.5	12.3	14.7
pH	--	6.88	7.11	7.69	7.24	8.30	7.97
SiO_2	mmol/L	0.647	0.865	0.759	0.816	0.222	0.353
Na^+	mmol/L	0.252	0.449	3.68	1.33	19.4	143
K^+	mmol/L	0.036	0.089	0.276	0.125	0.121	3.06
Ca^{++}	mmol/L	0.168	0.560	2.29	1.05	0.647	86.4
Mg^{++}	mmol/L	0.135	0.376	0.596	0.412	0.098	1.87
HCO_3^-	mmol/L	0.751	2.15	1.89	1.87	6.07	0.950
Cl^-	mmol/L	0.065	0.490	9.19	3.18	14.5	288
$SO4^{--}$	mmol/L	0.012	0.055	0.067	0.043	0.064	0.606
F^-	mmol/L	0.0059	0.010	0.028	0.015	0.033	0.012
NO_3^-	mmol/L	0.011	0.0051	0.0034	0.0054	0.0005	0.0024
Total Fe	mmol/L	0.002	0.017	0.012	0.014	0.077	0.018
Total Mn	mmol/L	0.0001	0.0014	0.042	0.014	0.0013	0.0096
[1]Al^{+++}	mmol/L	--	--	0.0024	0.0024	--	--
Ba^{++}	mmol/L	2.2E-05	--	0.0004	0.0003	--	0.0002
[2]Eh	mV	--	--	--	150	-88	-160
Calculated Parameters							
CO_2 Fugacity	bar	0.0037	0.0068	0.0018	0.0046	0.0014	0.00025
TDS	mg/kg	100	240	670	400	1350	16300
Select Mineral Saturation Indices (log Q/K)							
Amorph. Silica		-0.41	-0.21	-0.31	-0.24	-0.82	-0.61
Calcite		-2.1	-0.96	0.15	-0.64	0.62	0.95

Initial Mineralogy

Initial CRB mineralogy is identified from published literature, as well as from X-ray diffraction (XRD) and scanning electron microscopy (SEM) analysis of ASR well cuttings from the Beaverton area. The primary mineralogy of the basalts is plagioclase feldspar, pyroxene (usually augite), and iron oxides (mostly titanomagnetite); it may also include minor amounts of apatite, olivine, and occasional sulfides (Ames, 1980 and Hearn et al., 1985). XRD analysis of cuttings from the Wapshilla Ridge member of the Grande Ronde returned a composition of 66.2% andesine and 33.8% augite. A Sentinel Bluffs member sample yielded a similar composition of 68.6% andesine and 31.4% augite.

Secondary mineralization often occurs within the CRBG aquifers. Secondary minerals are more typically associated with water-bearing interflow zones. Amorphous silica, cryptocrystalline quartz (chalcedony), smectites and other clays, zeolites, and various iron oxides are all common products of secondary mineralization (Deutsch et al., 1982; Hearn et al., 1990; Tolan et al., 2009a). Benson and Teague (1982) suggested secondary minerals in the CRBG form in the order 1) smectite and iron oxides, 2) clinoptilolite or other zeolites, and 3) silica and other clays, in response to dissolution of basaltic glass. Studies by Hearn and others (1985) and Benson and Teague (1982) found that almost alteration seems to occur below 100 °C.

The formation of iron oxides generally occurs above depths of ~1,000 ft (Hearn et al., 1985) and requires suitably oxidizing redox conditions. Baker and Neill (2017) report the smectite nontronite forms early in the weathering process of the CRBG. However, they also found that at later stages of basalt weathering, dissolution of relict feldspars, apatite, and titanomagnetite coated with nontronite coincides with precipitation of montmorillonite and kaolinite clays. Celadonite (a mica group mineral) has also been found in scoriaceous flow tops of the Grande Ronde Basalt, filling vesicles and replacing the groundmass. Dissolution of basaltic glass and groundmass augite may respectively provide the necessary K, and Mg and Fe for celadonite formation (Strawn et al., 2012). XRD analysis of an interflow zone sample yielded a composition of 76% andesine, 23.3% augite, and 0.7% smectite ("montmorillonite") clay. Modeling of clay phase stabilities for the CRBG Avg water composition over a range of relevant temperatures and pHs indicates that saponite (a smectite) should be the dominant clay phase above 50 °C (Figure 4). The Avg 6 cluster waters, with a pH of 8.3 at measured temperatures of ~12 °C are at or near saturation with respect to Saponite-K and Saponite-Mg (mean SI values of -0.08 and +0.17, respectively), while modeled waters are highly supersaturated (SI values 2 to 5+) with respect to other clay phases included in the thermodynamic database, including nontronites and smectites. One exception is the CRB1 mean water, which appears at or near saturation with respect to Smectite-high-Fe-Mg (SI = 0.19). The most commonly reported zeolites are clinoptilolite and heulandite (Ames, 1980; Vlassopoulos et al., 2009; Zakharova et al., 2012).

Mineral phases utilized in the geochemical models include those which are: 1) identified in pertinent literature, 2) major primary minerals within the CRBGs or secondary minerals at or near equilibrium with CRBG groundwaters (Figure 12) and 3) those with precipitation rates sufficiently fast to potentially impact the RTES cycle. Literature recognizes both chalcedony (cryptocrystalline silica) and amorphous silica as potential secondary silica phases within the CRBG (Deutsch et al., 1982; Cummings et al., 1989; Gannett and Caldwell, 1998; Vlassopoulos et al., 2009). Models were also run both with and without gibbsite, and with and without clinoptilolite (a zeolite phase). Because clay and zeolite reaction rates are four to five orders of magnitude slower than reaction rates for amorphous silica, and because zeolites generally form after clays, clinoptilolite was only examined using equilibrium modeling to capture the "most extreme" case.

Table 12. Primary and secondary minerals used in geochemical modeling of RTES system.

Primary Minerals	Secondary Minerals		
Plagioclase	Amorphous Silica	Calcite	Saponite-Mg
Pyroxene	Chalcedony	Magnesite	Smectite-Reykjanes
Basaltic Glass	Gibbsite	Rhodochrosite	Smectite-high-Fe-Mg
	Fe(OH)3 (ppd)	Witherite	Smectite-low-Fe-Mg
	Goethite	Siderite	Clinoptilolite

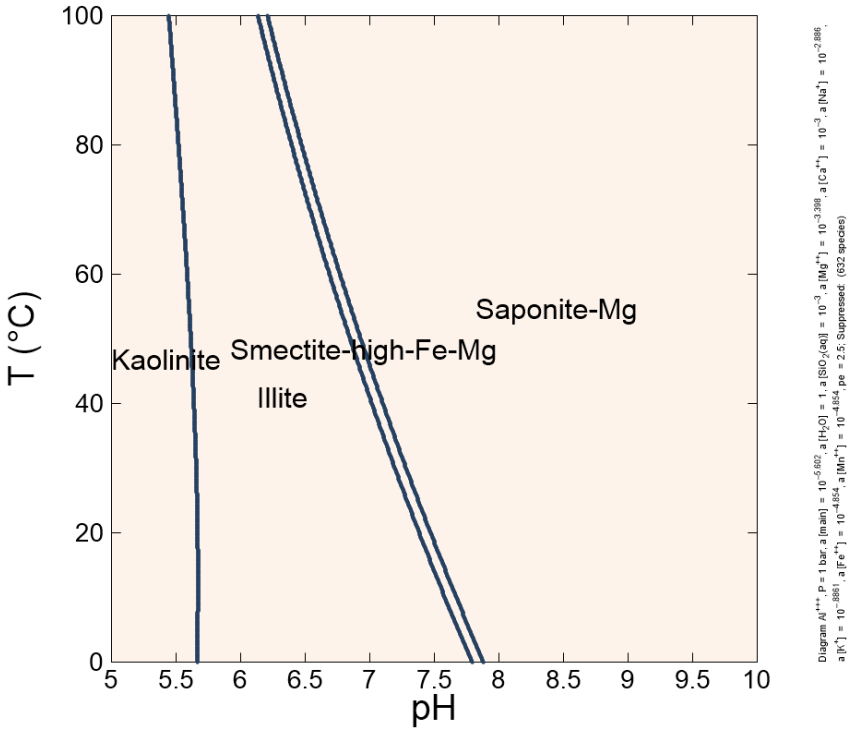

Figure 15. Temperature-activity (pH) diagram showing stability fields for various clay phases assuming "CRB_Avg" water composition. (Nontronites and smectite-low-Fe-Mg and smectite-Reykjanes were allowed to form in this model).

Modeling Methodology and Model Inputs

The program Geochemist's Workbench (Bethke, 2008) and the modified thermodynamic database were used to simulate the mass transfers and potential changes to water quality that result from cyclical heating and cooling of native groundwater, and to constrain the impacts of mineral assemblage, temperature, atmospheric pressure, flow rate, and water composition on results. Both equilibrium and kinetic transport models were used to simulate movement of water through the RTES system.

Equilibrium Modeling

The initial equilibrium models employ a polythermal reaction model to simulate heating extracted groundwaters from ambient aquifer temperature of ~11-14°C to a maximum temperature of 70°C (near the upper temperature threshold of the proposed RTES system).

Mineral saturation states are calculated for each step of the reaction path. Oversaturated minerals are allowed to precipitate in some cases to simulate scale formation in the heat exchange system and associated piping; in other cases, mineral precipitation is suppressed until the second modeling step (re-injection into the aquifer), to simulate slow kinetics or transfer of mineral mass as suspended solids. Initial heating was modeled with both fixed and sliding gas fugacities, the latter to simulate systems open to the surface atmosphere. In the sliding fugacity models, CO_2 and O_2 were allowed to slide from their initial estimated fugacities within the confined basalt aquifer to their fugacities under atmospheric pressure (CO_2 fugacity of 0.0004 and O_2 fugacity of 0.206). The resulting water was then subject to heating.

The secondary mineral assemblage considered in equilibrium models consists of amorphous silica, calcite, $Fe(OH)_3$(ppd), goethite, magnesite, rhodochrosite, siderite, witherite and saponite-Mg (as a proxy for all smectite clays). However, uncertainties due to lack of redox data for most samples in the database necessitates the use of an average Eh of ~150 mV for all water types, which limits formation of $Fe(OH)_3$, goethite and FeIII-bearing smectites in most waters. Gibbsite was initially included, but as it has a higher solubility than clays, was subsequently excluded.

The next modeling step simulates injecting heated water (from which carbonate mineral mass had been removed during the previous heating step) into the aquifer, with an assumed porosity of 0.2. Non-equilibrium dissolution of primary minerals at higher temperatures was modeled by titrating 60 mg/L (0.22 mmol/L) of plagioclase and 40 mg/L (0.4 mmol/L) of pyroxene into the water. The mass of minerals reacted was based on a series of batch reaction experiments conducted at elevated temperatures using CRBG cuttings and water samples. The minerals the water becomes oversaturated with in this step could precipitate and decrease aquifer porosity, if the volume of minerals precipitating exceeds the volume of minerals dissolving. Differences in bulk mineral volumes are due to net mass transfers due to dissolution and precipitation of specific minerals which may entail density differences between primary and secondary minerals, incorporation of dissolved ions or water in mineral phases (e.g., dissolved carbonate in calcite or waters of hydration in clays), and ion substitution in the idealized mineral formulas.

The last step in the equilibrium model simulates mixing between injected and native groundwaters via a flash model which incrementally mixes native groundwater with the injected fluid (from 0 to 100%). While this modeling step is revealing in terms of the impacts of mixing on mineral solubilities, the true extent of mixing is unknown. The additional use of transport modeling attempts to constrain the amount of mixing that is expected to occur between injected and native waters within the aquifer.

Kinetic Modeling

1D kinetic transport models simulate water-rock reactions within the aquifer over a 180-day injection-storage-extraction period. Use of a kinetic transport model accounts for both reaction rates and flow dynamics and so may provide more realistic estimates of mass transfers between minerals and water, and the extent of mixing between injected and native groundwaters during injection and storage. Modeled system parameters are provided in Table 13. Flow rates were varied to ascertain impact on mass transfer within portions of the modeled system. Domain lengths of 20 to 200 m were used to investigate the impacts of rock-water interactions and mixing in the near-well and distal regions of the system.

Table 13. Kinetic transport modeling parameters

Modeled Parameters	Values	References
1D Models		
Linear Domain		
Distance	20 to 200m	
Nodal spacing	0.5 – 1.0 m	
Node Cross-Sectional Area	1.0m (y) x 1.0m (z)	
Flow Rate	0.1 – 100 $m^3/m^2/d$	Tolan et al., 2009a
Permeability	1 darcy	Burns et al., 2015; Jayne and Pollyea, 2018
Longitudinal Dispersivity	2 m	Schulze-Makuch, 2005
Diffusion Coefficient	$1x10^{-6}$ cm^2/s	
Heat Capacity	840 J/kg/°C	Burns et al., 2015
Thermal Conductivity	1.6 W/m/°C	Burns et al., 2015
Radial Domain (near-well)	*Parameters not listed below are same as above*	
Radius 1 (well interface)	0.20m	
Radius 2 (domain length)	10m	
Nodes	10	
Angle	1 rad	
Flow Rate at Radius 1	1 to 400 $m^3/m^2/d$ (declines sharply with radius)	
2D Models	*Parameters not listed below are same as above*	
Distance (X)	200 m	
Distance (y)	160 m	
Nodes (X)	50	
Nodes (Y)	40	
Height (Z)	3 m	
Well Location	(20, 80m)	
Transverse Dispersivity	1 m	
Initial Hydraulic Gradient	0.005	
Pumping Rate	14 L/s	

As most reaction rate constants reported in literature are for 25°C, rate constants were calculated for higher temperatures in GWB using the Arrhenius equation and the activation energy and pre-exponential factor (Table 14), rather than the rate constant (with the exception of basaltic glass). A rate constant for 70°C was determined for basaltic glass via a linear regression

from values reported by Gislason and Oelkers (2003) for glass dissolution at 50°C and 100°C and neutral pH. Due to limited kinetic data for precipitation reactions, dissolution reaction data was used for some secondary phases (e.g., smectites). Specific surface areas were compiled from literature. Nucleation area was set at 1000 cm2/cm3 for all phases. Nucleation areas can vary by mineral, and seed particles can take a long time to form sufficient mass to initiate mineral nucleation (Van Pham et al., 2012; Hellevang et al., 2013).

A 2D kinetic transport model was also used to simulate the injection and storage period at high flow rates and explore long-range spatial variations of mineral precipitates. This simulated injecting water for 120 days at 13.9 L/s, followed by ambient flow for another 80 days, assuming a permeability of 1 darcy and a hydraulic gradient of 0.005 (1 m head drop over 200 m length). 2D transport model parameters are included in Table 13. The modeled injection well location was at x = 20 m, y = 60 m within the 200 m by 120 m domain. Minerals in the 2D model were incorporated the same way as the 1D model, with primary minerals and clays controlled kinetically, and carbonates controlled via equilibrium.

All minerals in kinetic transport models were suppressed, except for those allowed to kinetically react (kinetic parameters summarized in Table 14) and carbonate minerals. For most models, carbonate minerals are assumed to react on fast enough time scales to be controlled by equilibrium (Bethke, 2008), an assumption supported by nearly identical results obtained in initial modeling efforts using both kinetically and equilibrium-controlled carbonate precipitation. Initially, only primary basalt minerals were assigned an initial mass (45% plagioclase, 30% pyroxene and 5% basaltic glass), based on the bulk mineralogy identified by Camp et al. (1978). Models were run both with and without basaltic glass, as glass in the interflow zones has likely weathered to clay since emplacement. Secondary minerals were assumed to form as a result of kinetically controlled dissolution and precipitation reactions, so were not assigned an initial mass unless otherwise noted. Subsequent models utilized lesser amounts of available reactive minerals, including calcite (e.g., 3% calcite, 0.5% plagioclase and pyroxene), in order to simulate secondary minerals coating fractures which are assumed to account for the effective porosity.

Successive cycles were modeled using the *CRB_Avg* composition and a transport model wherein heated water is injected water for 180 days at a rate of 1 $m^3/m^2/d$, then recovered for another 120 days at the same rate. This simulation is accomplished in GWB by reversing the direction of flow and the hydraulic gradient at the end of the injection period. 1 $m^3/m^2/d$ was chosen to simulate slower flow during the storage period. The recovery cycle is shorter than the injection cycle to 1) ensure recovered water is as close as possible to its injection temperature, and 2) to leave some heated water in place to minimize cooling in the aquifer and increase long-term system efficiency. The first cycle begins by heating water to 70°C (using a polythermal equilibrium model) and injecting and recovering it from the aquifer using the transport model, building a 70°C reservoir within the aquifer. Transport model parameters and rates are the same as those included in Table 13 and Table 14 (using a linear domain).

Table 14. Dissolution rate constants (log(k)), activation energies (Ea), pre-exponential factors (log(A_w)) and specific surface areas (SA) at 25°C and neutral pH for primary and secondary minerals utilized in kinetic modeling. (Assuming dissolution rates approximate precipitation rates for secondary precipitates due to lack of available precipitation data). [1]Basaltic glass dissolution rate constant at 70°C. [2]Carbonate minerals are assumed to be equilibrium controlled for most models due to relatively fast reaction rates (Bethke, 2008). Calcite kinetic parameters used in simulations of calcite-lined pore space. [3]Reported for precipitation, not dissolution

Mineral*	**Log(k)** mol/m^2/s	**E_a** KJ/mol	**Log(A_w)** mol/m^2/s	**SA** m^2/g	**Reference**
Pyroxene (Augite)	-11.97	78.0	1.69	0.125	Palandri and Kharaka, 2004
Plagioclase (Andesine)	-11.47	57.4	-1.41	0.16	Stillings et al., 1996; Palandri and Kharaka, 2004
Basaltic Glass[1]	-12.23	--	--	23	Gislason and Oelkers, 2003
Calcite[2]	-5.81	23.5	-1.7	0.21	Palandri and Kharaka, 2004; Hellevang et al., 2013
Siderite[2]	-6.9	--	--	0.21	Hellevang et al., 2013
Smectite (Saponite-Mg)	-12.78	35.0	-6.65	10	Palandri and Kharaka, 2004; Hellevang et al., 2013
Amorphous Silica[3]	*-9.42*	*49.8*	*-0.66*	10	Palandri and Kharaka, 2004

Recovered water is cooled to 40°C using a polythermal equilibrium model, to simulate extracting heat from the water during the winter period. This cooled water is then injected into a different zone of the same aquifer system (building a cooler 40°C reservoir), modeled using a transport model with the same parameters and reactant phases as the transport model used to model the initial 70°C reservoir. The 40°C water recovered from this model is then reheated upon extraction to 70°C, using an equilibrium model and polythermal reaction path. This simulates reheating water during the summer period, prior to injection back into the original 70°C reservoir. Injection of 70°C reheated water marks the start of the next cycle. The resulting modeled system has two pumping regimes: the first occurs during the summer when water from the cooler reservoir is extracted, heated (via solar energy or another method), and injected into the hotter reservoir. The second occurs during the winter period, where water is pumped from the hotter reservoir, its heat extracted, and the resulting cool water is pumped into the cooler reservoir. As in previous models, minerals can precipitate as needed after each modeling step. "Waste" water (40°C water) is stored and later reheated because it would require more energy to continuously heat native groundwater with a temperature of ~12°C than recycled water with a presumed temperature of ~40°C.

Modeling Results

Multiple processes account for changes in geochemical conditions during heating and cooling of aqueous solutions. These include:

- Changes in aqueous pH and speciation with temperature.
- Changes in solubilities of minerals and gasses with temperature. Solubilities may increase with increasing temperature or decrease (gasses, carbonate minerals, some silicates). Changes in gas fugacities resulting from temperature changes or open systems may also impact mineral solubilities (e.g., carbonate solubilities with changes in fCO_2).
- Increased reaction rates with increasing temperatures.
- Exceedance of activation energy barriers at higher temperature, allowing precipitation of phases that are kinetically prohibited at lower temperatures.

Various models were constructed to explore geochemical changes through different stages of RTES operation, including initial groundwater extraction and heating, injection of heated waters into and reactions with CRBG aquifer, mixing with ambient native waters, and multiple cycles of injection and extraction. Models were utilized to explore the impacts of:

- Different groundwater compositions
- Different reactive phases and reactive phase surface areas (kinetic models)
- Varying temperatures of injected waters
- Varying pumping rates

Equilibrium Modeling

Step 1: Initial Heating of Extracted Groundwaters

Because many CRBG groundwaters are near saturation with respect to calcite and because the solubilities of calcite and other carbonates, such as siderite, decrease with temperature and with loss of CO_2(g), carbonate scaling is of primary concern during heating of groundwaters. The solubility of saponite clays also decrease with temperature. As shown in Figure 16 and Figure 17, the temperature at which waters become saturated with respect to calcite, siderite and saponite and the potential mass of the resulting precipitates is dependent on the

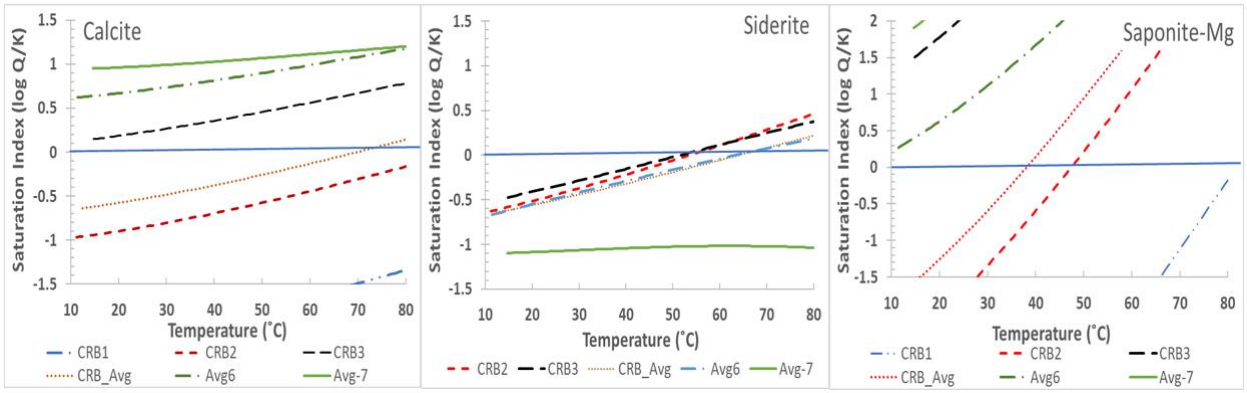

Figure 16. Saturation indices for calcite, siderite, and saponite-Mg with respect to temperature for different initial water compositions (from Table 11). A saturation index of 0 (horizontal blue line) represents equilibrium; SI values > 0 indicate the potential for mineral precipitation.

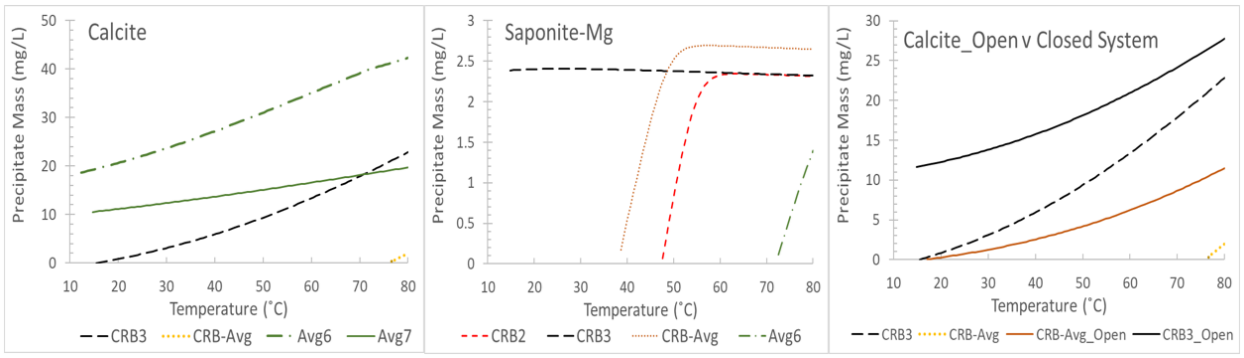

Figure 17. Modeled mineral precipitate mass (mg/L) resulting from heating different initial water compositions. Graph on the right shows differences between mass of precipitated calcite for closed (dashed or dotted lines) vs open atmosphere conditions (solid lines) for CRB3 and CRB_Avg only.

initial compositions (and saturation states) of the groundwaters. Less evolved waters may not reach saturation with respect to calcite at all or not until the water reaches relatively high temperatures (e.g., 70°C for *CRB_Avg* water; Figure 16). However, more evolved waters that are already at or above saturation with respect to calcite are likely to precipitate calcite throughout the range of temperatures considered. All of the CRBG waters reach saturation with respect to siderite between ~50-60°C. All but the least evolved waters (e.g., *CRB1*) exceed saturation with respect to saponite clays at relatively low temperatures (< 50°C). Although not shown in Figure 16 and Figure 17, more mature waters (*CRB_Avg*, CRB3, Avg6 and Avg7) precipitate some iron oxyhydroxide ($Fe(OH)_3$(ppd)), though typically less than 1 mg/L. However, the amounts of iron oxyhydroxide and siderite are dependent on the redox state of the water for which little data is available; these models utilized an Eh = 150 mV (the average of available Eh data for CRBG groundwaters).

While the potential volumetric masses of precipitates shown in Figure 17 may appear small (10s of mg/L), the cumulative precipitate mass over weeks to months of pumping at

projected pumping rates > 10 L/s may be significant. Should waters be subjected to open atmospheric conditions in the piping / heat exchange infrastructure, waters will lose CO_2 gas and the mass of calcite precipitated may be significantly greater (Figure 17) via the following reaction:

$$CO_{2(g)} + H_2O + CaCO_3 = Ca^{++} + 2HCO_{3-}$$

Kinetic constraints may inhibit short-term precipitation in the heat exchange system, particularly for clays. Calcite reaction rates are orders of magnitudes higher, so scale build up is of concern. However, if flow through times are short enough (e.g., < 1 day), it is possible that calcite precipitates may be carried into the aquifer as suspended colloids even if precipitation is initiated within the above-ground infrastructure. Filtration of suspended solids by the aquifer can result in significant decreases in aquifer porosity and permeability near the injection well.

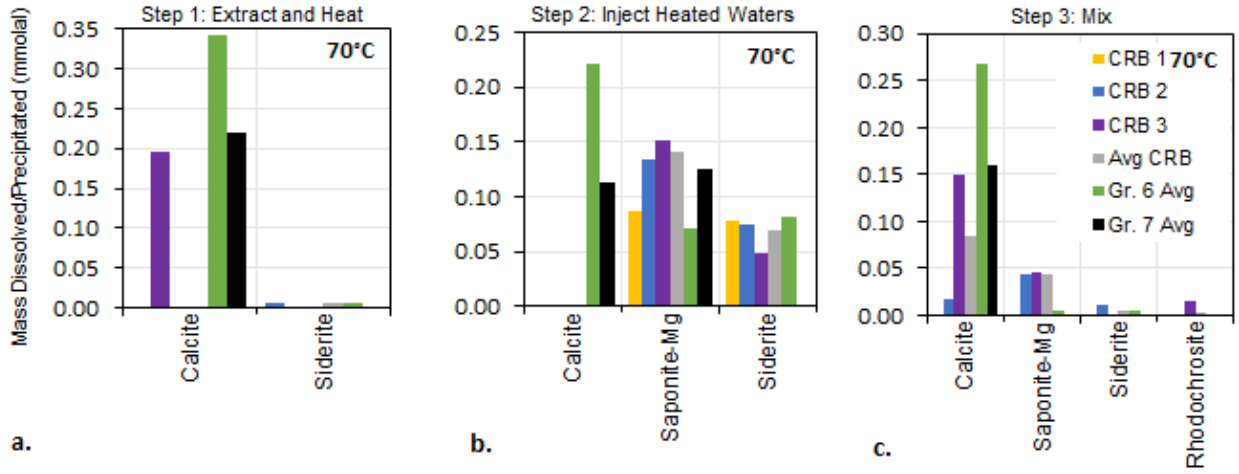

Figure 18. Amount of minerals precipitated per kilogram of water due to a) extraction and heating at the surface, b) injection and reaction with aquifer rock, and c) mixing between injected and native groundwaters. Colors represent different native groundwater compositions.

Steps 2 and 3: Injection of Heated Water into Aquifer and Mixing with Native Groundwater

Prior to injection into the aquifer, minerals (carbonates, iron hydroxides) for which waters are oversaturated are allowed to precipitate out to simulate scale formation at the surface, though this may not be a realistic assumption as explained above. Due to their slower reaction rates, clays (modeled as saponite-Mg) are not allowed to precipitate at surface but are allowed to precipitate upon injection of heated (70°C) water into the aquifer. Primary mineral dissolution (modeled as titration of plagioclase and pyroxene into the water) supplies additional Ca, Mg, Fe, Si, and Al which induces precipitation of additional saponite, as well as calcite and siderite in many waters.

Mixing injected and native waters results in precipitation of saponite-Mg, followed by carbonate minerals (Figure 18). Saline water and mature CRBG water types (the highest TDS

waters) precipitate the most mineral mass in response to mixing between injected and native groundwaters (in addition to precipitating the most mineral mass at the surface). Precipitation of calcite and other carbonates in this step may be linked to changes in pH and differences in the PCO_2 of injected and native groundwaters.

Kinetic Transport Modeling

Varying Water Compositions and Reactive Solids and Volumes/Surface Areas

An inherent problem with kinetic modeling is the uncertainty with respect to available reactive surface areas of modeled solids. This is compounded in complex natural systems by uncertainties as to what types of solid phases are even present. A series of models were constructed to investigate the impact of varying solids and reactive surface areas. The initial models assumed only the two primary basalt minerals plagioclase and pyroxene to be present. Their percent volumes (relative to the modeled aquifer domain) were varied from 45% and 35% respectively (the entire solid volume) to 0.45 and 0.35%, assuming only 1% of the solid was available to react (the rest of the solid is unavailable or "inert").

The potential for basaltic glass as a matrix component was explored using 45% plagioclase, 30% pyroxene, and 5% basaltic glass. A final scenario assumed reactive volumes of 3% calcite, and 0.5% each plagioclase and pyroxene to simulate calcite coated fracture surfaces; this scenario was used only for water types that are at saturation with respect to calcite under ambient conditions. Saponite clays and amorphous silica were allowed to precipitate kinetically; carbonate minerals (calcite, siderite, magnesite, rhodochrosite, and witherite) were allowed to precipitate via equilibrium control, except for the last scenario where calcite was kinetically controlled. Injection of both *CRB_Avg* and CRB3 waters at 70°C were simulated at a specific discharge of 1 m^3/m^2/day (for simplicity) through a linear aquifer domain initially containing ambient-temperature native groundwater.

The results for the *CRB_Avg* waters (Figure 19) show that the choice of reactive mineral mass can have significant impacts on results. Assuming the full volume of aquifer matrix is available to react, there is a net increase in aquifer porosity near the injection site and essentially no change further away. Inclusion of a small amount of basaltic glass yields very similar results near the injection site, but a slight reduction in aquifer porosity downgradient. However, such volumes of reactive material are likely only approached in the case of very fine-grained granular aquifers and are unlikely to reflect the fractured, brecciated and vesiculated nature of the basaltic flow zones. A reactive volume of only 10% of the matrix yields a net decrease in porosity (<5%, from 0.200 to 0.191) near the injection site, and a slight increase in porosity immediately

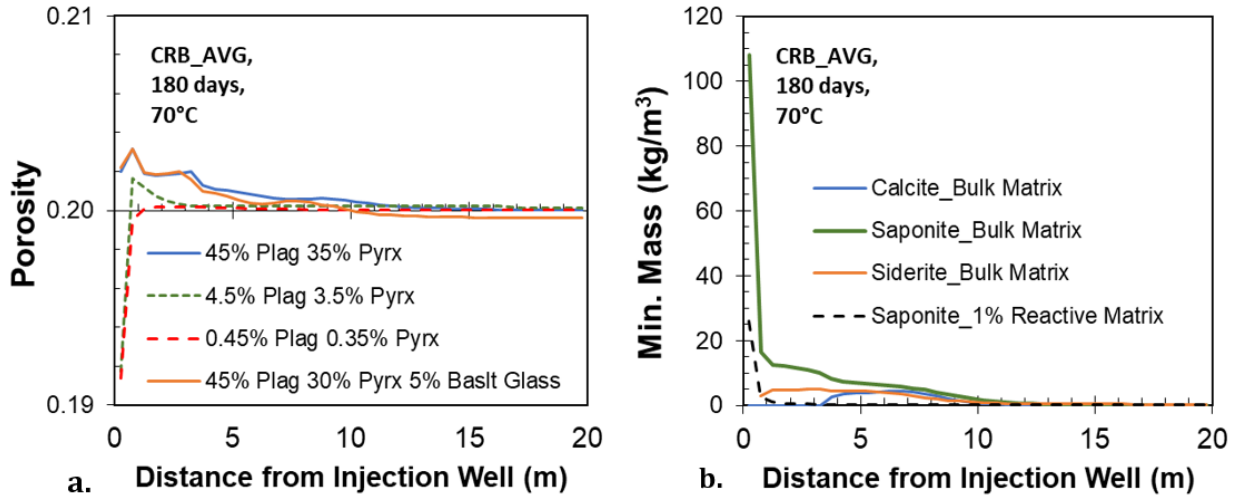

Figure 19. a) Changes in aquifer porosity (initially set at 0.20) after 180 days of injection of 70°C water (CRB_Avg) at a specific discharge of 1 m^3/m^2/day with varying %volumes of reactive minerals. These models assume removal of carbonate precipitates during initial heating at surface. b) The spatial distribution of select mineral masses precipitated in modeled aquifer domain. Solid lines represent case assuming bulk aquifer matrix (45% by volume plagioclase, 35% pyroxene); dashed line represents mass of saponite precipitated assuming 1% of aquifer matrix is available for reaction (0.45% plagioclase, 0.35% pyroxene).

downgradient. A reactive volume of only 1% of matrix yields a similar decline in porosity near the injection site and little change downgradient. Because any carbonate resulting from heating is assumed to have been removed at the surface, the porosity differences are largely due to the volume of primary silicates dissolved in the injected fluid and the volume of saponite precipitated. Although there is less saponite precipitated in the case of 1% reactive matrix compared to fully reactive matrix, there is also less dissolution of primary silicates.

Results for *CRB3* waters are shown in Figure 20. The worse-case scenario (a & b) would be the injection of waters where no carbonates were removed during heating, either because precipitation is slow compared to transport time or because high flow rates keep precipitates in suspension until injection and filtration in the aquifer. In this scenario (Figure 20), some loss of porosity can be expected, regardless of assumed matrix minerals or their reactive volumes. Porosity is reduced from 0.200 to ~0.175 (>10%) over the course of 180 days of continuous pumping for both the 1% reactive matrix and the calcite-lined fracture scenarios. The bulk matrix scenario yields a porosity loss of <5% (to ~0.19), with some increased porosity immediately downgradient. Much of the porosity loss is still the result of saponite formation although both calcite and saponite are present in significant amounts. In the scenario where carbonates have been removed prior to injection (by treatment or scale formation (c & d), there is similar porosity loss near the injection point, except in the case where all the solid matrix is available to react.

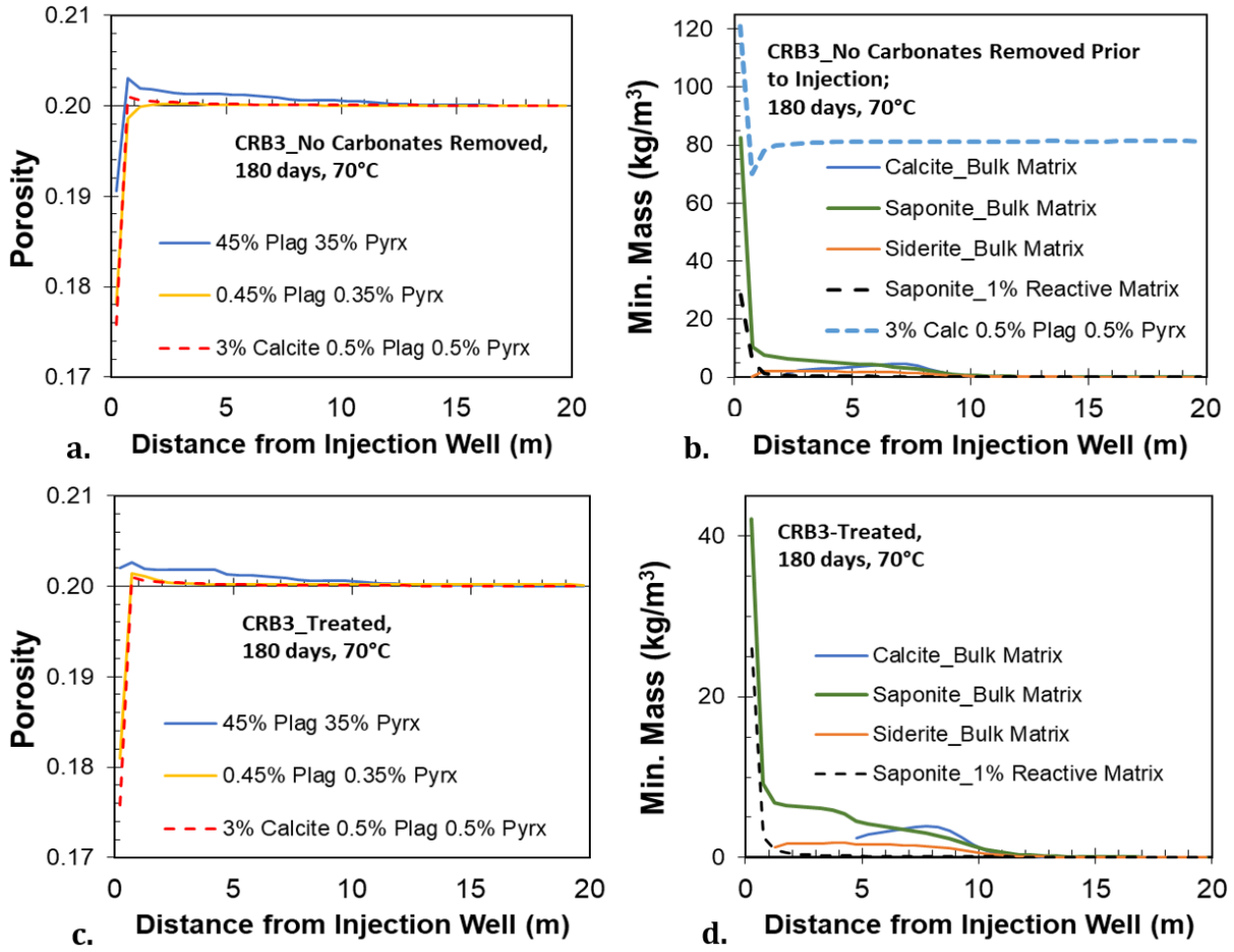

Figure 20. Changes in aquifer porosity (initially set at 0.20) and secondary mineral distribution after 180 days of injection of 70°C CRB3 water at a specific discharge of 1 m^3/m^2/day with varying %volumes of reactive minerals. (a & b) Water is injected without removal of carbonates during heating (injected waters are supersaturated with respect to carbonates). (c & d) Carbonate precipitates removed at surface (injected waters are at saturation with respect carbonates).

Two-dimensional modeling injection of heated *CRB3* waters supports the 1D model results. After 180 days, there is some porosity loss in the immediate vicinity of the injection well, largely due to saponite precipitation, and a slight increase in porosity immediately away from the well (Figure 21). Precipitation of calcite and siderite (not shown) occurs mostly just outside that zone of porosity increase. Farther from the well, at the injection (cooling/mixing) front, amorphous silica begins to precipitate (Figure 21). However, the amount per unit volume of silica precipitate is ~1000x less than for carbonates and the zone of silica precipitation will migrate with the injection front.

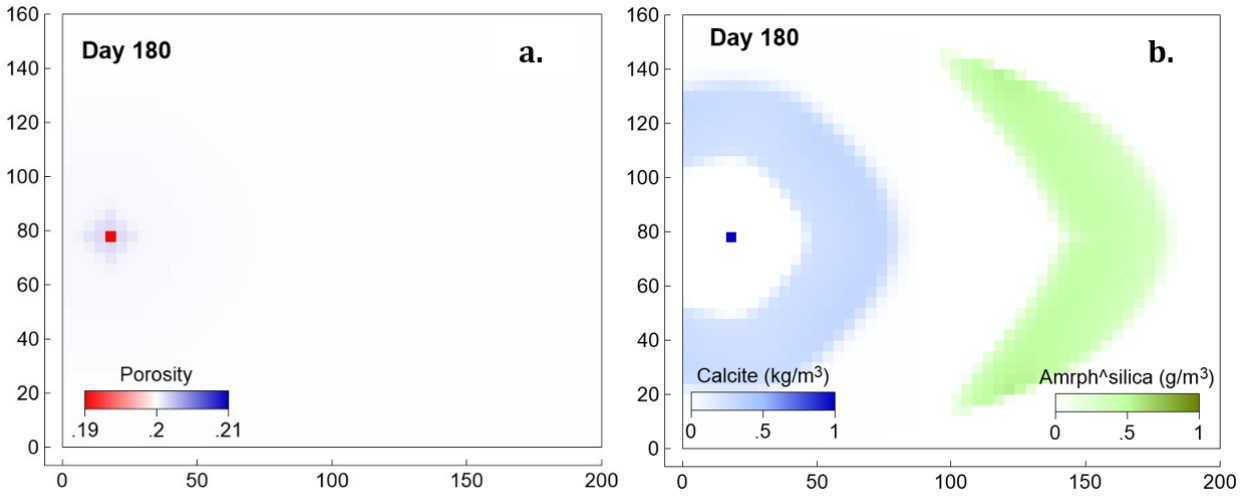

Figure 21. Map view of 2D model results showing a) changes in aquifer porosity (initially set a 0.20) near well injecting 14 l/s 70°C CRB3 waters (with carbonate precipitates removed during heating and 4.5% plagioclase, 3.5% pyroxene initial reactive solids); and b) distribution of calcite and amorphous silica deposits after 180 days of injection (siderite, not shown, has similar distribution as calcite). Model coordinates in meters; well located at x = 20, y = 80 m.

Varying temperature of injected waters

Heating groundwater reduces the solubilities of calcite, siderite, and saponite-Mg. This causes waters that are undersaturated to become oversaturated with respect to these phases (Figure 16). Reducing the temperature of the injection fluid reduces the degree of oversaturation and the mass of resulting precipitates. It also reduces reaction rates and dissolution of primary silicates that supply ions for continued precipitation of secondary phases. Model results using 50°C injection waters yield significantly different results in terms of secondary mineral masses and changes in porosity (Figure 22). Assuming 10% reactive solid matrix and the same mineral suite as before, model results show a slight increase in aquifer porosity for *CRB2* and *CRB_Avg* waters and only a slight decrease (< 1%) in the case of more evolved *CRB3* waters after 180 days of injection. After 3 years of continuous pumping (which is not the planned mode of operation), *CRB_Avg* waters induce only a 5% decrease in porosity, comparable to the results obtained after only 180 days of injecting 70°C waters (Figure 22).

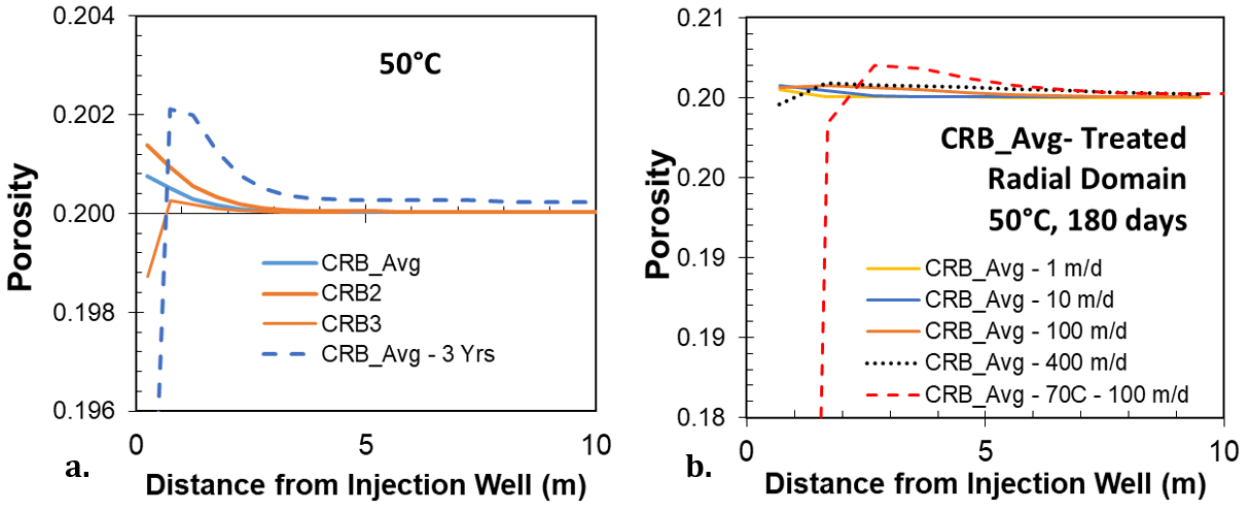

Figure 22. a) Modeled changes in porosity (initially set at 0.200) near injection point (left side) for various water types (following removal of any carbonate precipitates during heating). A specific discharge of 1 m/d is used for all cases. Solid lines are for 180 days of injection; dashed line is for 3 years of continuous CRB_Avg water injection. b) Modeled changes in porosity near injection site for CRB_Avg waters injected at different rates (specific discharge in m/d at injection site; radial domain model employed which allows sharp declines in specific discharge with increasing radius and cross-sectional area). All lines are for injection of 50°C waters, except dashed line (provided for reference) which is modeled with 70°C water. Reactive solid volumes are 4.5% plagioclase and 3.5% pyroxene for all cases.

Varying flow rate

The impact of varying flow rates on porosity near the injection point was explored using a radial model domain. The radial domain accounts for increasing cross-sectional area and a corresponding decrease in specific discharge away from the injection site. This enables modeling of high flow rates that are expected in the first few meters where cross-sectional flow-through areas are minimal. Increasing the flow rate (the number of pore volumes per unit time) produces a greater mass of secondary minerals, though it may also enhance dissolution of primary silicates by maintaining significant undersaturation. For *CRB_Avg* waters injected at 50°C, there is not a great difference in porosity (a very slight increase) between an injection rate of 1 and 100 m/d; there is a slight decrease at 400 m/d. However, there is a significant loss of porosity (>50%) at 100 m/d when injecting *CRB_Avg* waters heated to 70°C, where they are oversaturated with respect to carbonates and saponite (Figure 22).

Modeling of Successive Cycles

The results from modeling recycling of water between two ("hot" and "cool") reservoirs indicate that both reservoirs may experience porosity loss (Figure 23). In the 70°C reservoir, saponite and calcite formation causes a porosity loss in the immediate vicinity of the injection well, followed by a slight porosity increase downgradient. However, the greatest changes to porosity in the 70°C reservoir occur during the initial cycles and impacts may be less severe and possibly reversed in subsequent cycles, as water temperatures are maintained within more narrow limits and waters chemistries are held closer to saturation with respect to key minerals.

The 40°C reservoir shows a slight porosity increase after the first cycle, as primary minerals dissolve in response to the elevated temperature. In later cycles, porosity decreases near the injection well due to precipitation of clays and silica minerals.

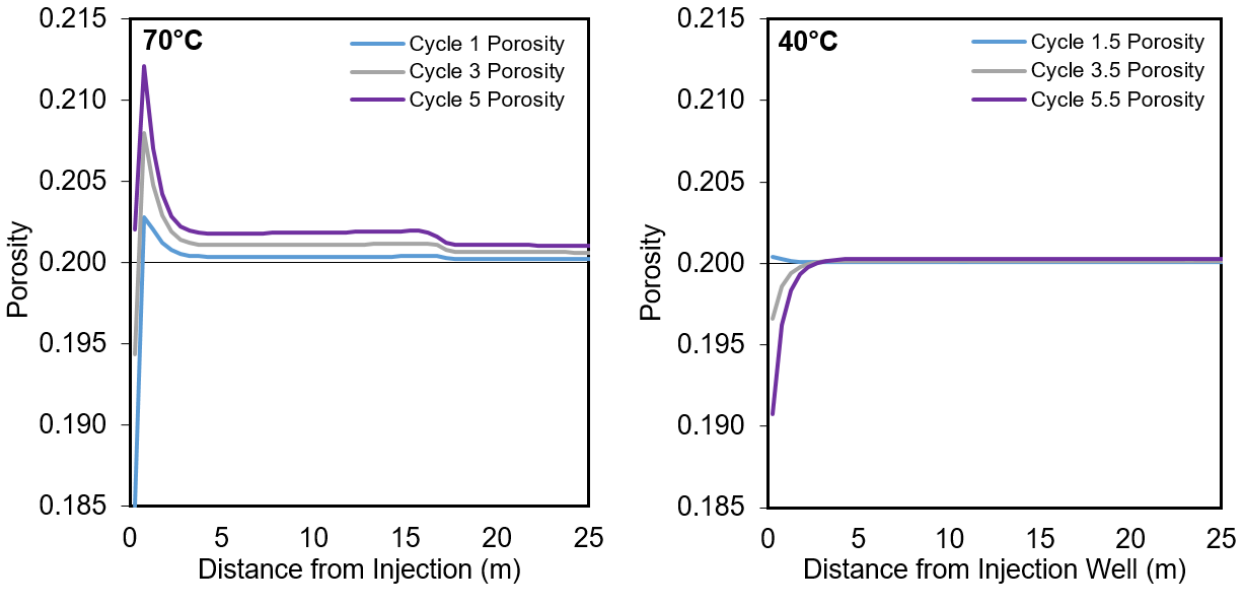

Figure 23. Changes in porosity after 5 successive cycles of pumping/recovery/pumping in a) primary aquifer ("70°C") and re-injection of cooled water into b) separate reinjection zone ("40°C").

Conclusions and Recommendations

The major ion chemistries of native CRBG groundwaters evolve by dissolution of primary silicates until waters reach saturation with respect to calcite, at which point Ca is removed via precipitation and Na+K / total cation ratios increase. Locally, waters may be impacted by mixing with upwelled saline water from underlying units, presumably along cross-cutting structures or open boreholes. Therefore, the RTES site should be carefully chosen to avoid structures which could facilitate upwelling of cooler waters from deeper units.

Because the solubilities of some common phases, including calcite, siderite (Fe carbonate) and saponite-Mg (smectite clay), decrease with increasing temperature, elevated temperatures can result in extensive mineral precipitation. Reaction rates for carbonate precipitation are typically orders of magnitude faster than for clays, so precipitation of carbonate minerals (chiefly, calcite and siderite) has the potential to form extensive scale deposits within pipes and heat exchange systems upon heating, particularly if native groundwaters are evolved and already saturated with respect to calcite. Ideally, the target zone would also be chosen to avoid water that is saturated with respect to calcite, though less evolved waters may still reach saturation with calcite, siderite, and or saponite clay above ~50°C. Precipitation of these phases in the aquifer, or transfer of suspended precipitates to the aquifer, could result in significant declines in porosity and permeability, likely at or near the injection site.

The impact of RTES operation on aquifer porosity and permeability will depend on the composition of groundwaters and on the nature and extent of available reactive surfaces in contact with injected waters. Most kinetic transport simulation scenarios indicate some loss of porosity near the injection point when injected waters are heated to 70°C. Such loss is minimized, though not necessarily eliminated, when waters are only heated to ~50°C. Under the most optimistic conditions (less evolved waters, ample reactive silicate surfaces, lower temperatures, and or low to modest flow rates), a slight increase in porosity near the injection point may occur. Under the worst-case scenarios (mature waters that are saturated or oversaturated with respect to calcite, an absence of reactive silicates as in calcite-lined fracture porosity, higher temperatures, and higher flow rates), significant porosity loss (>10%) may occur within one seasonal cycle. Modeling the recycling of waters between two reservoirs maintained at 70°C and 40°C suggests porosity loss in both reservoirs, but that some porosity may be recovered in the 70°C reservoir over multiple cycles.

Silica precipitation is likely to occur at the cooling / mixing front in the RTES reservoir. However, the volumes precipitated are unlikely to cause significant porosity loss and over time the cooling front and associated mineral buildup may migrate with expansion of the hot water mass. Similarly, extracted hot waters that have accumulated additional silica through dissolution of primary silicates may precipitate silica scale upon cooling in the heat exchange system or reinjection zone.

Modeling the extent to which mineral precipitation and dissolution reactions occur is complicated by uncertainties with respect to phases exposed in pore spaces, their reactive surface areas, and kinetic rates. Expanding what is known about the target zone in terms of its water chemistry, the nature of porosity, and the extent of secondary minerals, will allow for more accurate modeling of geochemical impacts from RTES cycles. Therefore, the next phase of the project would ideally include exploratory drilling and water quality sampling.

PART 2: HEAT AND FLUID FLOW MODELING

The USGS team led the heat and fluid flow simulations for evaluation of the RTES reservoir. A summary of relevant details is provided here. The full summary was published in Geothermics (Burns et al., 2020).

Overview

Tools to evaluate reservoir thermal energy storage (RTES; heat storage in slow-moving or stagnant geochemically evolved permeable zones in strata that underlie well-connected regional aquifers) are developed and applied to the Columbia River Basalt Group (CRBG) beneath the Portland Basin, Oregon, USA. The performance of RTES for heat storage and recovery in the Portland Basin is strongly dependent on the operational schedule of heat injection and extraction. We examined the effects of the operational schedule, based on an annual solar hot water supply pattern and a building heating demand model, using heat and fluid flow simulations with SUTRA. We show RTES to be feasible for supply of heating energy for a large combined research/teaching building on the Oregon Health and Science University South Waterfront expansion, an area of planned future development. Initially, heat is consumed to increase the reservoir temperature, and conductive heat loss is high due to high temperature gradients between the reservoir and surrounding rock. Conductive heat loss continues into the future, but the rate of heat loss decreases, and heat recovery efficiency of the RTES system increases over time. Simulations demonstrate the effects of varying heat-delivery rate and temperature on the heat production history of the reservoir. If 100% of building heating needs are to be supplied by combined solar/RTES, then the solar system must be sized to meet building needs plus long-term thermal losses (i.e., conductive losses once the system is heated to pseudo-steady state) from the RTES system. If the solar heating system barely meets these criteria, then during early years, less than 100% of the building demand will be supplied until the reservoir is fully-heated. The duration of supplying less than 100% of building demand can be greatly shortened by preheating the reservoir before building heating operations or by adding extra heat from external sources during early years. Analytic solutions are developed to evaluate efficacy and to help design RTES systems (e.g., wellspacing, thermal source sizing, etc.). A map of thermal energy storage capacity is produced for the CRBG beneath the Portland Basin. The simulated building has an annual heat load of ~1.9 GWh, and the total annual storage capacity of the Portland Basin is estimated to be 43,400 GWh assuming seasonal storage of heat yields water from which 10 °C can be extracted via heat exchange, indicating a tremendous heating capacity of the CRBG.

PART 3: INFRASTRUCTURE AND ENGINEERING

System Overview

The system being proposed for OHSU consists of roof mounted solar heating units and two wells spaced 457 or 914 meters apart. A permeable interval within the Columbia River Basalts Group (CRBG) will be selected for purposes of thermal storage by reviewing logging and well test data. Thin and laterally extensive permeable zones have been encountered when drilling through the CRBG in other locations (Burns et. Al 2016b). A liner will be made up with well screens installed at the selected interval. Once the liner is in place, drillers will gravel pack the well or keep the annulus open, depending on the stability of the wellbore and the presence of fines. According to a model of a new building at OHSU (described in Part 2), the inlet temperature of KCRB is 49.6 °C. A roof mounted solar system will be designed to heat water to between 60 °C and 90 °C. During the summer months, water will be produced from the down-gradient well and heated to the target temperature before being cycled through the building and injected back into the aquifer. In winter months hot water will be produced from the up-gradient well and run through the solar thermal system on sunny days. This will add supplemental thermal energy to the fluid before it is cycled through the building and injected into the down gradient well. Figure 24 details the design of the system and shows the nature of operations during summer months.

The temperature of the produced water has a large impact on the design of the proposed system. If temperatures greater than 49.6 °C can be produced from the upgradient well, then it is possible to use produced water directly within the target building's heating loop. No heat exchanger will be required. However, if the temperature of produced water is too erratic, despite it being above the 49.6 °C threshold, a heat exchanger or some other mechanism may be required to regulate the temperature. In the case where produced water is below 49.6 °C, the water will be sent to a pre-heater which will heat the return water up to a higher temperature before it is brought to 49.6 °C using conventional methods. A potential constraint to using the produced water directly within the heating loop is that the system may not be able to heat enough water during the summer months to meet the annual thermal demand of the building. This is especially true in the first years of operation. Building the solar array to handle the entire heating load of the building in the first years of operation may be cost prohibitive. An alternative to overbuilding the system is to prime the storage system with a more appropriately sized system. Priming would consist of injecting all the heat generated by the solar array during the first year, or years, of operation directly into the ground without passing it through the buildings heating system. In the case of KCRB, annual thermal energy demand from the heating system is 1.88 GWh.

Though we are focused here on heating requirements, we acknowledge that a similar system could be used for cooling during the summer. Future work may focus on using RTES for cooling.

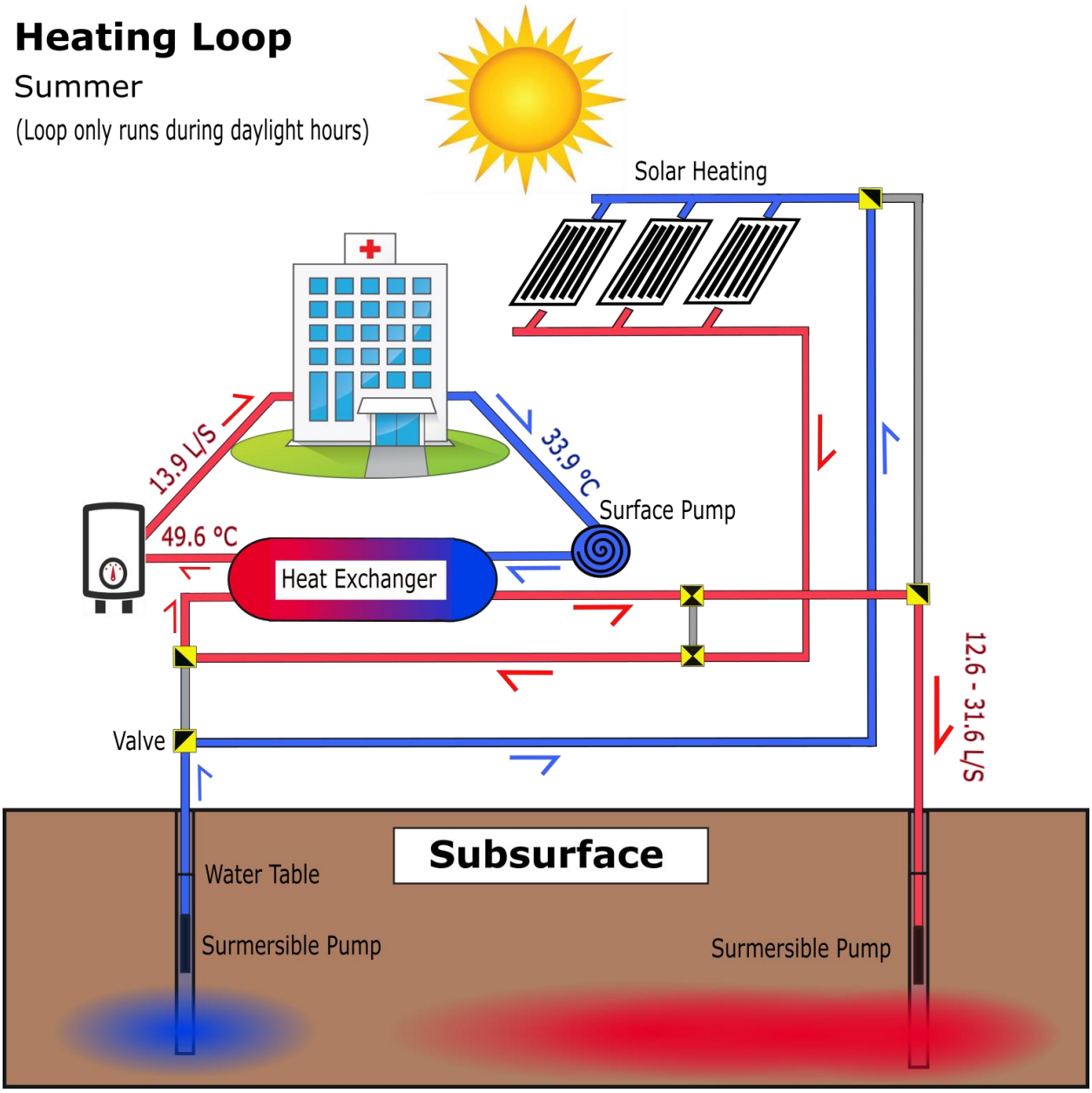

Figure 24. OHSU RTES System. Schematic shows operations during summer months.

Design Assumptions for Well Doublet

The well doublet design is based on the following assumptions:

1. A closed loop of "geothermal" water will have a maximum capacity of 800 gpm (182 m^3/hr) from a cool well to a hot well in summer and reverse in winter
2. The two geothermal wells will be drilled vertically and be spaced 1500-3000 ft (457 -914 m) apart.
3. Well diameters will be slightly oversized to allow for potentially higher flow rates in the future

4. In order to reverse the flow seasonally, a pump will be installed in each well.

3.1 Infrastructure Design

Well Locations

As discussed in the geology section, the targeted aquifer is in the Columbia River Basalt Group. Wells drilled through this CRBG within the region often encounter permeable intervals characterized by thin, laterally extensive, permeable fractured basalt. These units act as an ideal storage medium due to the low thermal conductivity of basalt and the relative isolation of these permeable intervals from the primary aquifer. Two potential well doublet options have been determined to be feasible within the scope of this project. The first potential well paring is

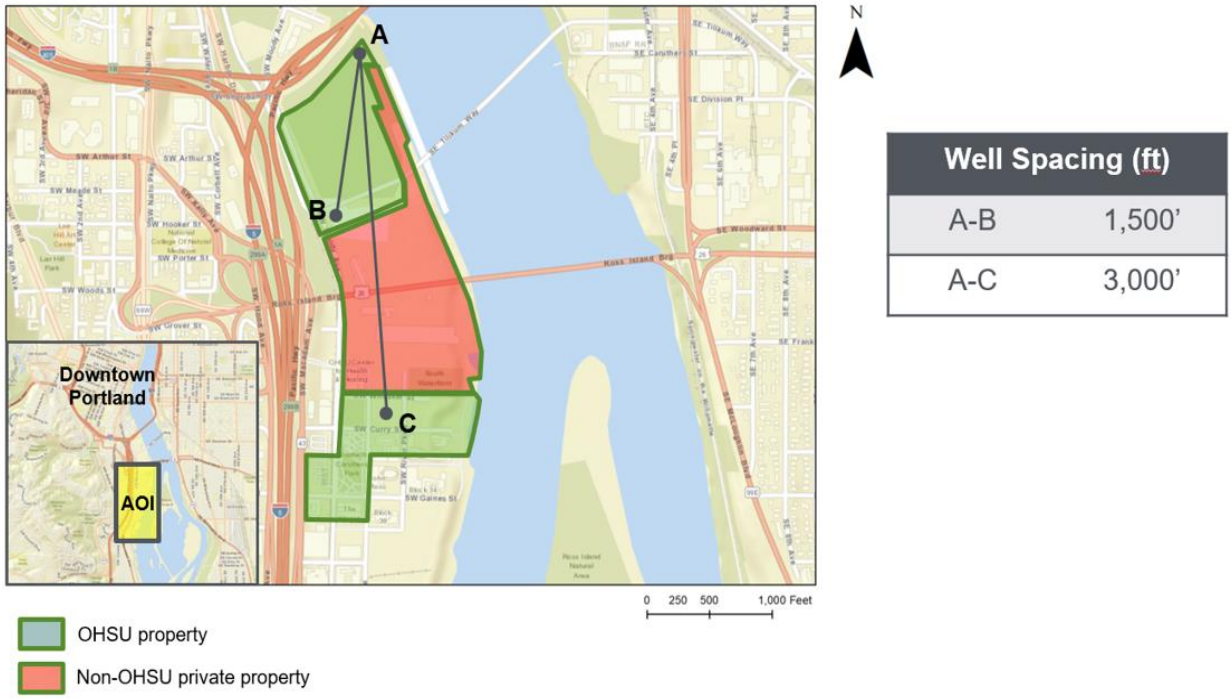

Well Spacing (ft)	
A-B	1,500’
A-C	3,000’

Figure 25. Two potential options for the well doublet system. Point A to B is 457 meters and point A to C is 914 meters. Well depths are shown in Table 1.

between location A and B shown on Figure 25. The second is between location A and location C, which will be the more expensive and time consuming of the two options. A well doublet between A and C will require trenching and installation of underground insulated piping through city and private land. It would be prudent to avoid this option if possible, but it may be required for the cooling doublet system. An RTES cooling system will require much larger volumes of water to be economically viable, which increases the radius of cooled water transported laterally from the injection well within the selected aquifer. Therefore, a larger distance between the cooling water doublet will likely be more efficient over the life of the project.

Modeling has shown that the first potential well paring, with a spacing of 457 meters between wells A and B, is expected to be sufficient to meet the demands of the project. Both

wells will have different target depths, as shown in Table 15. Well B will be drilled to a shallower depth than Well A because geological studies indicate that the CRBG shallows toward the south. The geologic target in both wells is the same as a previously drilled well, MULT 106063 - about 300 feet into the marine volcanics, below the CRBG. MULT 106063 well was drilled north of the site in 2011 under the supervision of PSU.

Production casing depths for the proposed wells, shown in Table 15, are designed to seal the open hole section of the well from the primary aquifer. These casing depths have been designed using well data proximal to the area of development and may need to be changed if the initial analysis of the data is found to be incorrect. Both wells will need to drill through at least 15-30 meters of CRBG before casing is set, therefore casing depth will be affected by the depth of CRBG encountered in the well. The amount of CRBG needed to be drilled before casing is set is dependent on rock competency and fracture density. Setting the production casing a sufficient depth into the CRBG will ensure that no inter-aquifer flow occurs within the well (Figure 26). It is suggested that the project purchase extra casing for both wells to minimize potential down time during well completion.

Table 15. Expected casing design for wells A and B.

WELL CONFIGURATION	HOLE DIAMETER	DEPTHS Well B	DEPTHS Well A	CASING
Surface casing	17-1/2"	50	50	13-3/8" 68 lb L80 Butt
Production casing	12-1/4"	600	800	9-5/8" 47 lb T95 Prem
Completion Interval	8-1/2"	900	1100	Open hole or 7" perforated liner

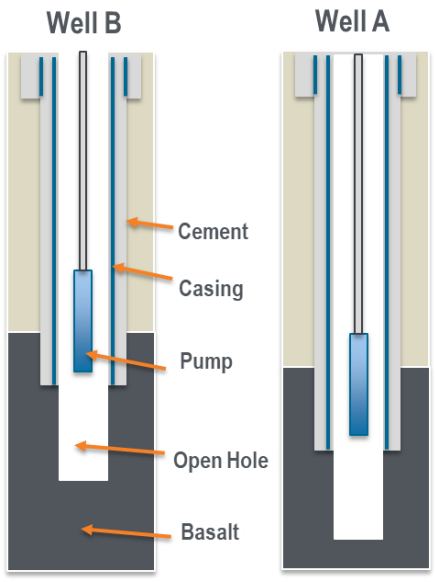

Figure 26. Well schematic of Wells A and B.

Logging and Testing

Both wells will be logged by an onsite geologist over the entire depth. However, once the well reaches its Total Depth (TD) it will be logged using a suite of electric logging tools. These include:

1. Pressure-Temperature-Spinner Survey Tool
2. Gamma Ray
3. SP (Spontaneous Potential)
4. Caliper
5. Resistivity

These logs will help the project geologist identify fluid filled fracture zones within the CRBG. This information will be used to determine where to set the screens or perforations for the liner. In addition to these logs, a series of well test will be performed. At a minimum, a pressure fall-off test will be performed. This test involves setting a transducer at depth, typically through a lubricator or some similar device, injecting water into the well under pressure and then closing the well valve and terminating injection. The resulting fall off in pressure with time will provide valuable information about the nature of permeability in the subsurface.

Additionally, a step rate test may be performed. This will provide information about the injectivity (L/bar) of the well and allow project engineers to determine the optimal settings for the pumps. A step rate test is performed by measuring the wellhead or downhole pressure while pumping at different rates for a set periods of time. Step rate tests should be pumped under pressure and they should be conducted over the range of expected operation. In most cases, project operators should have a step that exceeds the highest expected injection rate in order to determine any potential issues that may result from running the infrastructure at the upper bounds. The maximum allowable pumping rate is determined by the fracture gradient. Pressure while pumping cannot exceed the fracturing pressure of the formation. If the fracture gradient is exceeded it may result in fracturing the formation and/or the cement behind the casing. This would compromise the integrity of well and may cause inter-aquifer communication.

After both wells have been completed, it will be prudent to conduct an inter-well communication test. The first step will be to determine the static water level in relation to a datum shared by both wells. The well with the lower water level will be considered the down gradient well. Once this has been determined, the down gradient well will be pumped and the pressure in the upgradient will be carefully monitored.

Running a tracer test in addition to the other test discussed is highly suggested. Tracer tests are useful because they give detailed information on the permeable pathways that connect wells. Tracer tests can determine if there are multiple flow pathways between wells, the surface area of those flow pathways and the velocity of the water traveling through these pathways. To perform a tracer test, a non-reactive substance will be injected into the up-gradient well at a

known concentration and water samples will be taken at set time intervals from the produced water being pumped continuously from the down gradient well. Tracer tests are a regularly used in hydrological studies. Common tracers include specialty dyes, salts and naphthalene sulfonates.

3.2 Infrastructure Costs

Using the Wellcost Lite software package developed by Bill Livesay, an estimate of the cost of both wells A and B have been made. The predicted cost for Well A is $691,414 and the predicted cost for well B is $611,147 for a total cost of $1,302,561, see both Table 16 and Table 17. An initial quote provided by drilling company Boart Longyear estimate a cost of $800,000 for Well A and $750,000 for well B for a total cost of $1,550,000. These estimates likely have a built-in contingency of 10-15%, which is generally best practice for drilling cost estimates.

Table 16. Estimated drilling and completing costs for Well A.

WELL CONFIGURATION	HOLE DIAMETER	DEPTHS	Interval Time (hours)	CASING	Drilling Cost Summary	Materials	Total
MOB/DEMOB					$ 50,000		$ 50,000
Surface casing	17-1/2"	50	53	13-3/8" 68 lb L80 Butt	$ 60,773	$ 19,532	$ 80,305
Production casing	12-1/4"	1000	238	9-5/8" 47 lb T95 Prem	$ 272,907	$ 194,699	$ 467,605
Completion Interval	8-1/2"	1200	68	Open hole or 7" perforated liner	$ 77,973	$ 15,530	$ 93,503
Total Cost					$ 461,653	$ 229,760	$ 691,414

Table 17. Estimated drilling and completing costs for Well B.

WELL CONFIGURATION	HOLE DIAMETER	DEPTHS	Interval Time (hours)	CASING	Drilling Cost Summary	Materials	Total
MOB/DEMOB					$ 50,000		$ 50,000
Surface casing	17-1/2"	50	53	13-3/8" 68 lb L80 Butt	$ 60,773	$ 19,532	$ 80,305
Production casing	12-1/4"	600	158	9-5/8" 47 lb T95 Prem	$ 181,173	$ 194,699	$ 375,872
Completion Interval	8-1/2"	900	78	Open hole or 7" perforated liner	$ 89,440	$ 15,530	$ 104,970
Total Cost					$ 381,387	$ 229,760	$ 611,147

Contingencies are often a necessary component of drilling budgets because drilling costs are difficult to predict accurately. While determining the cost of materials is straightforward, drilling rates are often unpredictable. This is because there are many potential unexpected issues that can be encountered while drilling. Potential issues include:

1. Artesian Flow
2. Loss Circulation
3. Hole Collapse/Instability
4. Water Management
5. Equipment Malfunction

Many of these issues can be mitigated with proper planning and procedure. Artesian flow can be adequately handled by having excess mud tank capacity, installing a knife valve and/or installing a Blow Out Preventor (BOP) stack. A BOP stack is only needed for wells where high pressure flow is expected. Loss circulation can be mitigated by designing a mud system where

sufficient wall-cake is formed and by having an appropriate amount loss circulation material on site. Hole collapse can be mitigated by using salt or some other approved material to increase the weight of the mud system, allowing for overpressure drilling. Pumps, mud tanks and water source must be oversized with regards to expected conditions in case of large mud losses or artesian flow. Lastly, there should be back-up parts for all mission critical equipment.

Pump Design

Two pumps optimized for two potential operational conditions have been provided by Tom Hoyt of Schlumberger. Both pumps suggested by Schlumberger are electrical submersible pumps (ESP). The first pump, Pump A, has been designed for an optimal flow of 235 gpm, with an operational window between 4.66 kg/s and 14.93 kg/s. The pump has 12 stages and runs at 60 Hz. Pump efficiency at 10.96 kg/s is 77% whereas pump efficiency for 4.66 kg/s and 14.93 kg/s are 55% and 65% respectively (Figure 27). This pump has an initial capital cost of $63,985 and will cost $2,897/month to operate continuously at 10.96 kg/s, assuming $0.10/KWh power cost (Table 18). The set depths for the pump will be contingent on the permeability of the well. However, the pump can go no lower than 50 ft from the base of the production casing. This is done to limit the potential of fines and rocks entering the pump and because of annular restrictions caused by the liner.

Pump B has been designed for an optimal flow of 25.65 kg/s, with an operation range between 21.46 kg/s and 33.58 kg/s. The pump has 13 stages and operates at 60 Hz. Pump efficiency at 25.65 kg/s is 68.5% whereas pump efficiency for 25.65 kg/s and 33.58 kg/s is 65% and 62% respectively (Figure 27). The initial capital cost for Pump B is $63,199 and it will cost $8,685/month to run on a continuous basis, assuming a 23.32 kg/s flow rate and $0.10/KWh power price (Table 19). Set depth will be contingent on the permeability of the well and be limited to a maximum depth of 15 meters from the base of the production casing.

Table 18. Pump A components and estimated cost.

ESP for 225 GPM @ 575'

Item	Qty.	PN#	Description	Price	Comments
BOH	1	T492231	HEAD: BOLT ON DISCHARGE PMP, 540, RLOY, 3.50 OD 8RD EUE		
Pump	1	100393814	PUMP: S8000N CR-CT 12 STG 538/540 30 CS BTHD, 1.00 HS MON, M-TRM, AFL, ARZ-SS, FACT SHIM		
Intake	1	102775454	INTAKE: BOI, 540/540 RLOY 1.18 INC 718, M-TRM, A		
Protector	1	102978027	PROTECTOR: MAXIMUS, BPBSL, 540/540, KTB/HL, 1.18		
Motor	1	100373216	MOTOR: 562 2, F022, MAXIMUS, RA-S, CS,		75HP/1272V/36A
Motor Lead	1	100714601	MLE:562 MAXLOK-400, 75FT, KELB M, 5KV, 4/1, P/I		Motor Connection
Cable	575'	L5651047	CABLE:REDAMAX400 #4, 5KV(4/1 EE G5R)		Main Cable
MISC	1		(Coupings, Splice, Shipping Boxes, etc)		
Field Service			Assembly of ESP (including travel, lodging, etc)		Estimate
				Estimated Total	$63,985.00

Table 19. Pump B components and estimated cost.

ESP for 500 GPM @ 725'

Item	Qty.	PN#	Description	Price	Comments
BOH	1	10006261	HEAD: BOLT ON DISCHARGEPMP, 675, CS, 5.50 OD 8R		
Pump	1	100053733	PUMP: JN21000 C-LT 14 STG 675/738 50 CS BTHD, 1.18 HS MON, M-TRM, HSN, ITGL I		
Protector	1	102978027	PROTECTOR: MAXIMUS, BPBSL, 540/540, KTB/HL, 1.18		
Motor	1	102763050	MOTOR: 562, 5, F053, MAXIMUS, RA-S, CS, M-TRM, AS, AFLAS, HL, GRB, MAXJOINT		188HP/2424V/47.4A
Motor Lead	1	100714601	MLE:562 MAXLOK-400, 75FT, KELB M, 5KV, 4/1, P/I		Motor Connection
Cable	825'	L5651047	CABLE REDAMAX400 #4, 5KV(4/1 EE G5R)		Main Cable
MISC	1		(Coupings, Splice, Shipping Boxes, etc)		
Field Service			Assembly of ESP (including travel, lodging, etc)		Estimate
				Estimated Total	**$63,199.00**

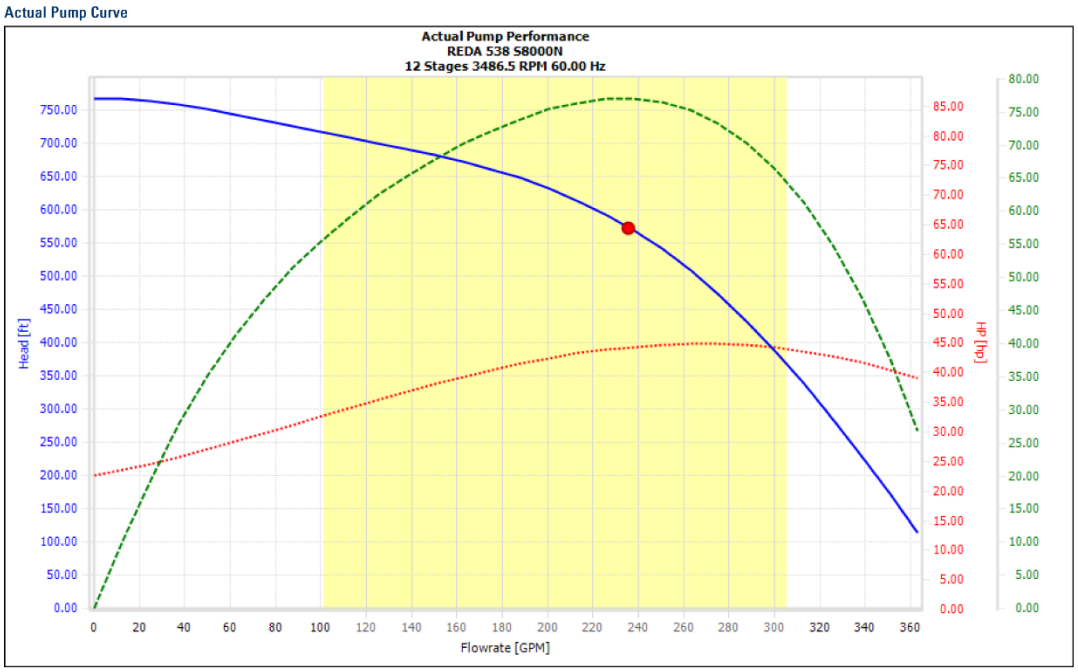

Figure 27. Dashed green line is pump efficiency. 200-260 gpm, Peaks at 75%, >55% from 100-320 gpm

Pumping during the summer months is contingent on solar irradiance levels. This means that pumping will only occur during select hours of the day during summer months. Given this, it may be advantageous to have a larger pump in the down gradient well and smaller pump in the upgradient well. This will allow the system to handle large flows during peak solar hours in the summer months but pump efficiently at low volumes during the rest of the year, when heat is being taken out of storage. The determining factor for the pump size of each well is the inlet temperature required by the OHSU building/buildings and the total heat required to meet the winter heating load of the selected buildings.

A Variable Frequency Drive (VFD) will be needed if project engineers determine that the installed pump should operate at multiple flow rates. With a VFD installed, the pump will still have to operate within its defined acceptable range presented in Figure 27, but it will be able to change pumping rates to adapt to potential changes in conditions encountered by the system. This will require additional costs but will allow for more operational flexibility. Installing VFD's

may also require additional maintenance cost, but such cost will be minor in comparison to the larger maintenance requirements. Frequency of larger scale maintenance requirements will be contingent on the specific use case of each well. Pumps that are being ramped up and down frequently will require more maintenance than pumps being run continuously at one speed. While EPS's are robust, conducting maintenance on these pumps can be difficult. This is because ESP's need to be removed from the well in order to be fully tested and/or repaired. Frequent monitoring of pump diagnostics to inform preventative maintenance is suggested, and such monitoring can largely be automated using software.

Piping

The pipe to be used for this project will be 254mm steel underground insulated piping. This is relatively oversized for the requirements of the initial project but will allow for the potential expansion of the ATES system in the future. A 254mm diameter schedule 40 Steel pipe will have 0.016 bar pressure loss for every 30.5 m of pipe length at a flow rate of 63 kg/s. This is a low enough head loss that it will not impede the overall efficiency of the system. Smaller diameter pipe, while cheaper, may be problematic. If the project were to use 152.4 mm pipe at this same flow rate for example, there would be 0.2 Bar head loss for every 30.5 m of pipe. For the lateral length between well A and B, a 3.1 Bar loss in head is expected, which would significantly impact the efficiency of the overall system. The pipe selected for the pipeline connecting well A and B has a High-Density Polyethylene (HDPE) jacket and a polyurethane insulating layer and steel pipe interior. A HDPE jacket prevents water infiltration, extending the life and insulating properties of the pipe. For long pipe lengths and/or slow flow rates, heat loss to the ground can be significant if insulation is not used (Figure 28).

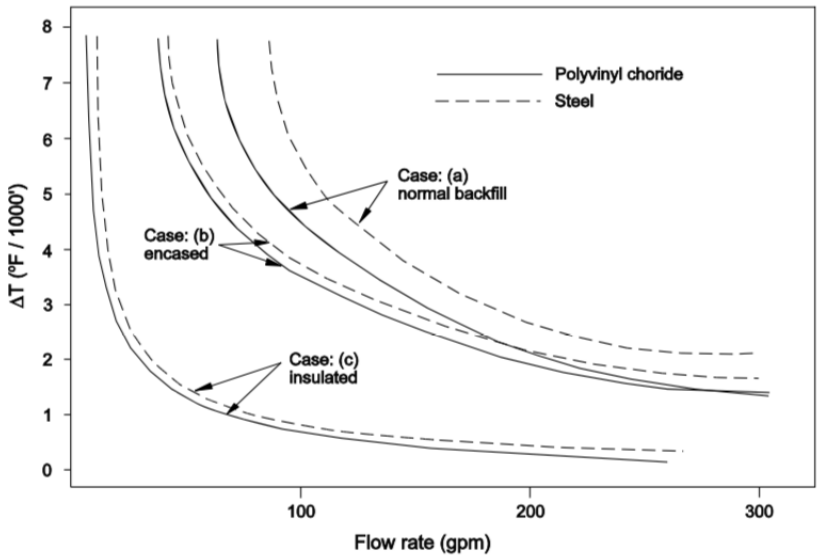

Figure 28. Relative heat loss as a function of flow rate and piping used for fluid transport (Ryan, 1981).

Assuming that Well A and B will be used as the heating doublet well pair, trenching costs should be around $30,000 according information from Washington State Department of Transportation (WADOT, 2015). Tangshan Xingbang Pipeline Engineering Equipment Co. put the cost of 254 mm underground insulated piping at $50/meter, for a total project cost of $22,850. Both wells are located on OHSU land and permits to trench on private or city land should be minimal. A utility locator will be hired to identify the location and depth of various utilities, ensuring no damage done to existing utilities during excavation. Once the various utilities are located, trenching will commence using a standard excavator.

OHSU New Build

This feasibility study focuses on meeting the heating requirements for KCRB at OHSU. KCRB is six stories, 10,400 m^2 and consists of office and laboratory space. It is located in climate zone 4C, which is defined as mixed-marine. The HVAC system is a VAV air handler with thermal inputs supplied by chilled and hot water. This study proposes that chilled and hot water into the HVAC system be supplied by a mixture of solar heating and heat pulled from RTES.

During KCRB design, energy consumption for a typical year was simulated using the eQuest/DOE2.2 software, resulting in hourly estimates of heat exchanger temperatures and pumping rates (PAE, 2017). It was estimated that the heating loop for the HVAC would consume 1.88 GWh of thermal energy annually. Inlet temperature for the heating coils is 49.3 °C and the estimated average return temperature for the hot water loop is 33.8 °C. Average flow of the system is estimated to be 3 l/s (47.6 gpm) and the maximum flow is estimated to be 15.6 l/s (247 gpm). The system must be run at a minimum of 2.3 l/s (36.5 gpm) during operation. Total volume of water cycled through the heating loop is estimated to be 94.6 million liters / year (25 million gallons / year). Flow rates will vary based on water temperature and building demand.

A more granular analysis of the simulation data shows that the energy consumption over the course of the day is highly variable. Peak energy consumption occurs at 7:00 am, when the ambient air temperature is low, and people begin arriving at the KCRB (Figure 29).

The largest variation in energy usage between seasons also occurs in the morning, where there is a 540 KWh difference between summer and the winter. Mid-day energy usage is far less variable between seasons, with a difference in energy usage between summer and winter of 130 KWh. While energy usage rises at night, it is not to the levels seen in the morning hours. Energy usage is at its lowest point at 11:00 pm after most staff members have gone home. These demand profiles imply that pumping requirements for the system will vary significantly during each day, not just on a seasonal basis. This means that a Variable Speed Drive (VFD) will be required for the well pump. In addition, it may be advantageous to have insulated surface storage for hot water. This would allow the heating system to nimbly respond to demand fluctuations and reduce the maintenance requirements on the Electric Submersible Pump (ESP).

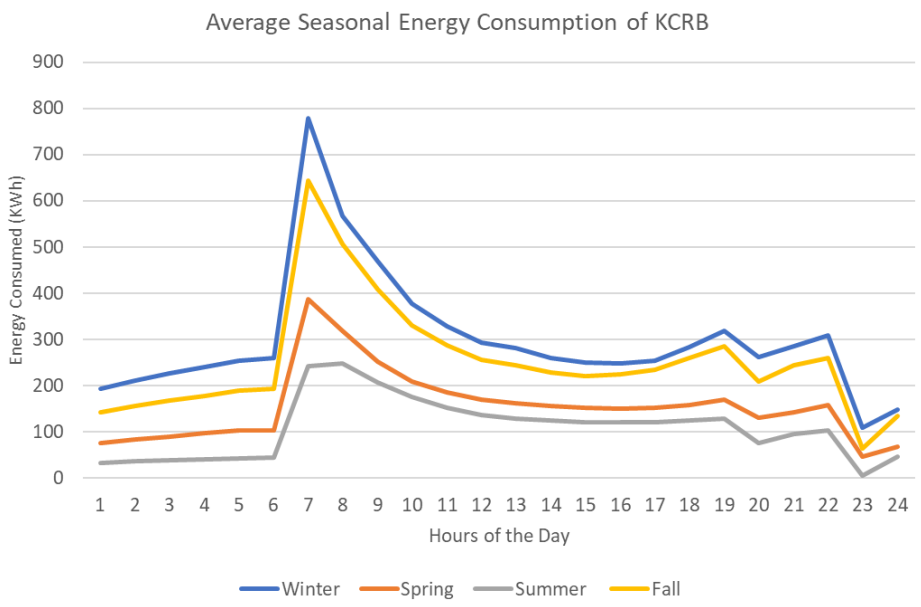

Figure 29. Average hourly energy consumption on a seasonal basis

Solar Infrastructure

The solar system design for this study considered four unique scenarios:

1. Solar system will meet 75% of the annual heating demand from KCRB and inject water into storage at a temperature of 80 °C
2. Solar system will meet 75% of the annual heating demand from KCRB and inject water into storage at a temperature of 60 °C
3. Solar system will meet 125% of the annual heating demand from KCRB and inject water into storage at a temperature of 80 °C
4. Solar system will meet 125% of the annual heating demand from KCRB and inject water into storage at a temperature of 60 °C

The temperature of the fluid to be injected does not affect the size of the solar system, however, it does affect the pumping and pipe insulation requirements. Therefore, in the four the scenarios considered only two different sized systems are required, one that meets 75% of KCRB heating demand and one which meets 125% of demand.

There are four major solar thermal heating technologies which are commercially available: Unglazed EPDM Collector, Flat Plate Collector, Evacuate Tubes and Parabolic Trough (Figure 30). One of the first ideas considered were solar troughs, which are highly efficient and can generate fairly high temperatures. However, these systems have high O&M costs, they are difficult to install on roofs and they can experience significant efficiency losses due to rain and wind, which are common occurrences Portland. The other option explored was flat panel solar collectors. These systems are less complex, have no moving parts, and are far

easier to install in difficult environments, such as roofs. For these reasons, flat panel solar collectors represent 90% of the solar heating market in the United States (NREL, 2016). After a survey of the available solar thermal technology, it was clear that high efficiency flat panel collectors or vacuum tube collectors were the best technological choice for the use case defined in this study.

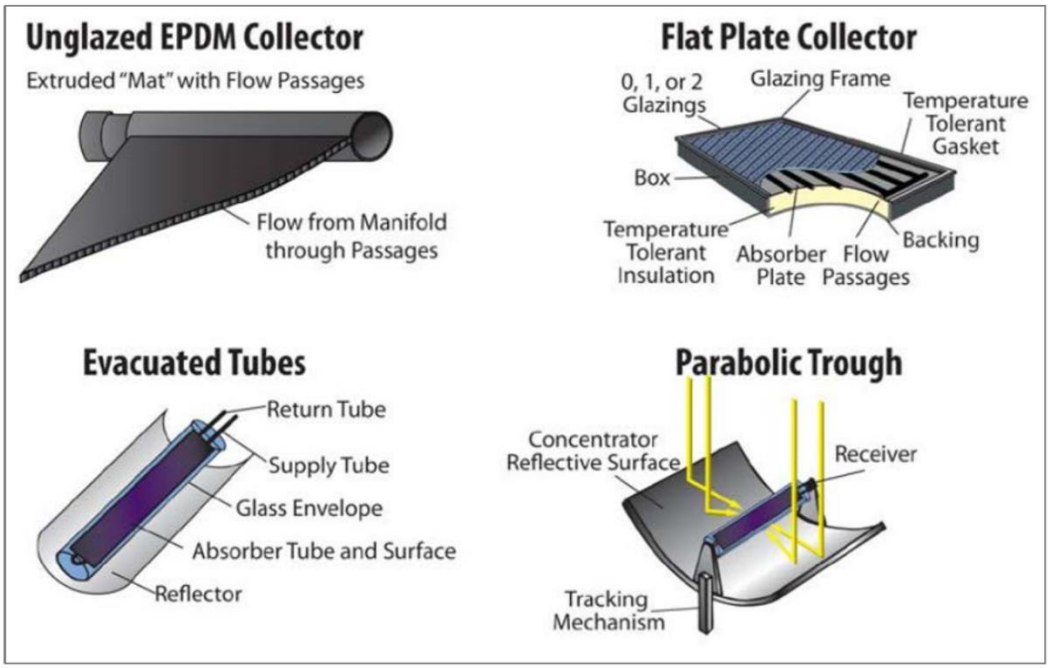

Figure 30. Types of solar thermal collectors that are commercially available (NREL, 2016)

There are two main types of Flat Plate Collectors, Honeycomb Solar Thermal Collectors (HSTC) or conventional glazed Flat Panel Collectors. HSTC's have been optimized to provide high efficiency heating throughout the year. If OHSU were not employing seasonal storage, this technology would likely be the best be the best option. However, conventional systems are better when seasonal storage is available because they can collect more heat during the summer months (Figure 31). In addition, the proposed system will be extracting heat from the ground in the winter, minimizing the need for solar heating during this time. Winter months in the Portland area are also characterized by short and cloudy days, meaning that very little solar energy is available during the winter months. For these reasons a conventional Flat Plate Collector called ThermoRay, designed by SunEarth, has been chosen as representative technology to be used at this project. The cost quoted for this system, $\$1345/m^2$ also happens to be slightly below the average cost for a conventional system, which is $\$1{,}538/m^2$ (NREL, 2016). These rates are for total footprint, which includes necessary inter-panel spacing to reduce shade.

The solar installation in this study is sized relative to KCRB. Total thermal load for this building is 1.88 Gwh of heat. The full load the building can be met with 477 units covering 3010 m^2 in area given a 3m spacing between rows of panels. The optimal angle inclination of the panel

for the Portland area was determined to be 45° and the efficiency of the panel is ~75%. This means that the panel can capture 75% of the radiation incident on its surface as heat.

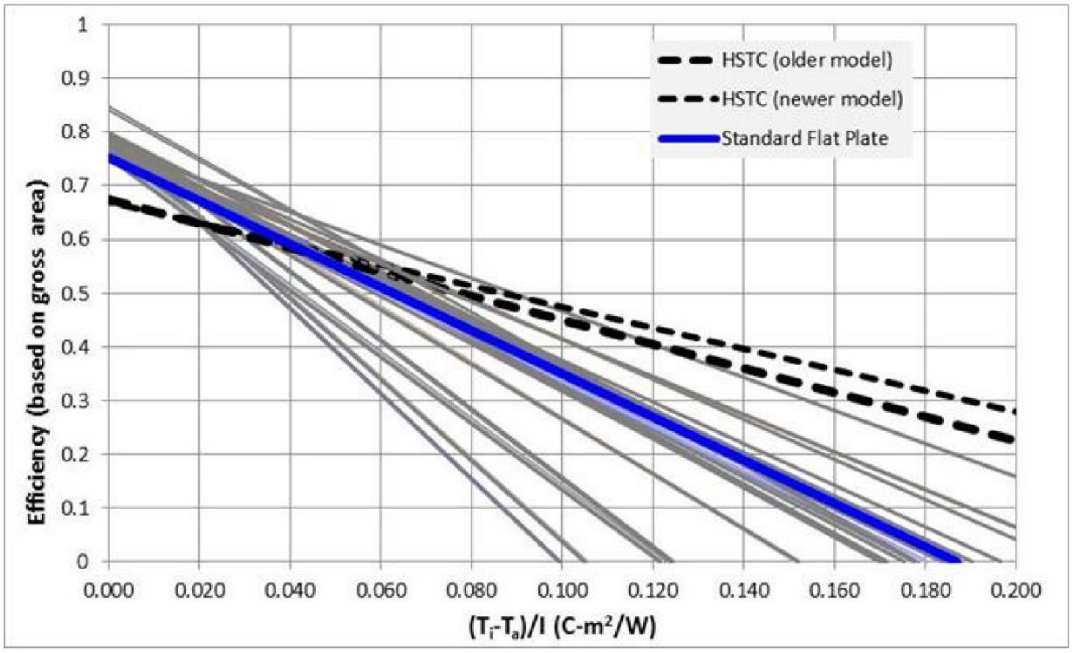

Figure 31. Efficiency of different solar thermal flat panel systems. Flat panel being proposed is characterized by the blue line. Ti is average collector temperature, Ta is ambient air temperature and I is solar radiation incident on the panel. Roughly speaking summer months are represented by the left of the graph and winter months are represented by the right of the graph (NREL 2016).

The first step in designing the system is to determine the total amount of solar radiation that can potentially be captured in the Portland region. NREL collects solar radiation data for different regions in the United States and allows the public to access the data at the National Solar Radiation Database (NREL, 2019). Three years with high quality data hourly data, 2007-2009, were used to determine what a typical year may look like. The model created is shown in Figure 32. During the month of June, the average radiation in a 24-hour period is ~250 W/m^2 while the average radiation high is ~655 W/m^2. This compares Phoenix, Arizona where the average radiation in a 24-hour period is 345 W/m^2 with an average high of 1000 W/m^2 (Mahmoud et al., 2016). Found in northern latitudes and with cloudy winters, Portland has comparatively less potential than many other cities in the Unites States. However, there is a large differential in solar radiation between summer and winter, which means that seasonal thermal storage may be crucial to implementing solar thermal systems within the city.

The planned solar array will be restricted to the rooftop of buildings to account for potential impact of shade from surrounding buildings and vegetation, as well as land use constraints. This design choice means that the height of a building will be an important factor when considering where to install the rooftop array.

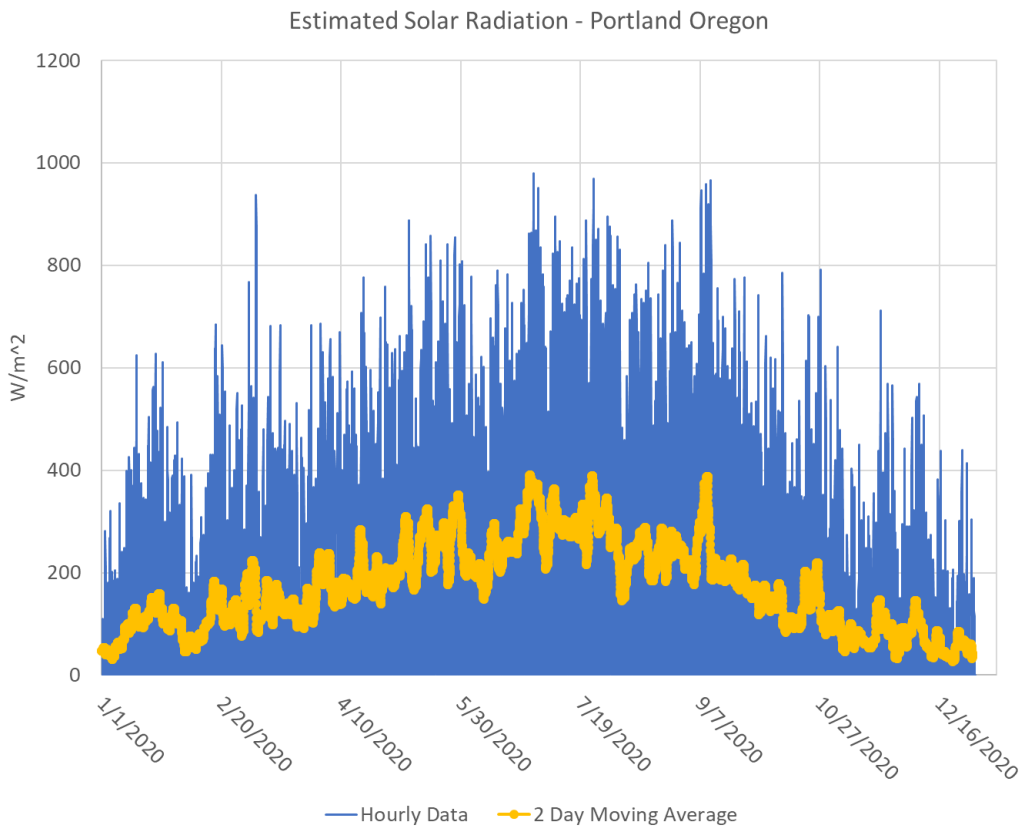

Figure 32. Projected hourly solar radiation over the course of a typical year. Raw data as well as a two day moving average are shown.

Water being fed into the array will have to pumped to the top of a selected building, or buildings, using either the well pump or a booster pump located at the base of the building. Taller buildings will impose larger energy demands on the pumps within the system, leading to lower overall efficiency. When detailed project planning begins, careful consideration will need to be taken with regards to the height of buildings on which the solar array is installed.

Using rooftops will mean that the overall space available for the project will be highly restricted. Solar arrays typically have an optimal row spacing, where one row of panels will not cast a shadow on another during productive parts of the day. For buildings of a certain size, project planners may have to design the array so that panels are more closely packed together than is optimal. Smaller than optimal spacing will generate more energy per unit area of rooftop, but will increase the marginal cost of the overall system. This relationship between row spacing and overall cost of the system is explored in Figure 33. What becomes apparent is that an inflection point exists at 3-meter spacing between rows. This means that any system that is built in the Portland area should not have less than 3-meter spacing, or the costs will become uneconomic. Given this, it becomes clear that in order to meet the demands of either 75% or 125% of the KCRB heating load, more rooftop space will be required than available at KCRB, which only has around 1,500 m^2 of useable rooftop space. At a minimum, one would need

roughly double the rooftop space available at KCRB to meet 75% of the heat load for the building.

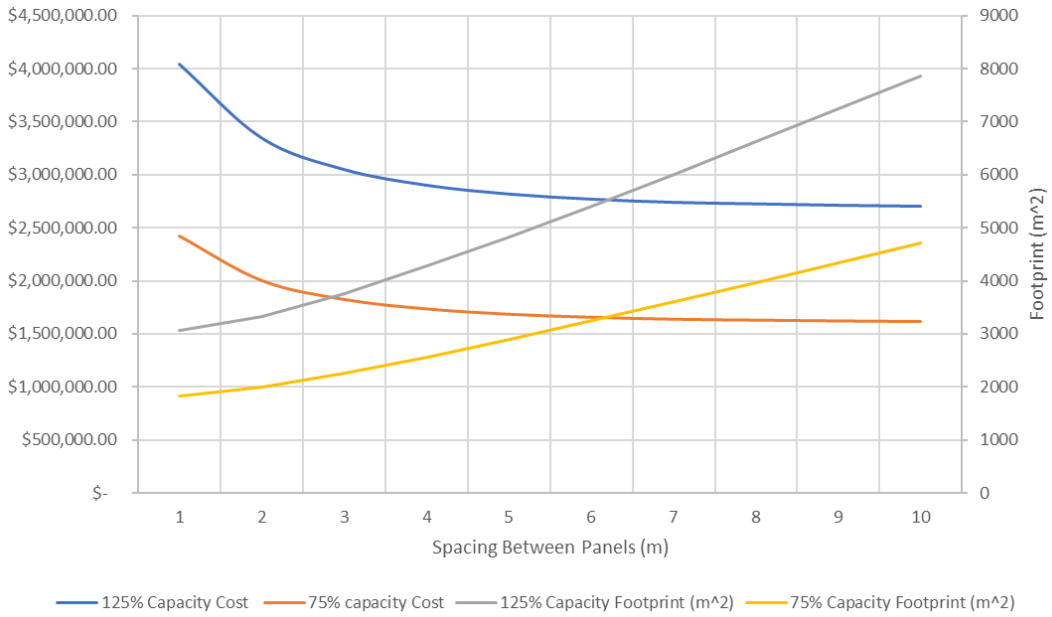

Figure 33. The effect of row spacing on system cost and footprint.

The outlet temperature of the solar array is another important factor to consider during for the RTES system. Higher outlet temperatures require less pumping and smaller diameter piping. This will have a significant impact on operational and capital costs, especially in cases where solar arrays are located on tall buildings. Other advantages to higher outlet temperatures include less potential for advective loss of stored heat and more efficient transfer of heat within heat exchangers. A major drawback to higher temperatures is an increased potential for mineral precipitation in the aquifer, which could damage permeability and reduce storage capacity. Such temperatures could also lead to precipitation within the piping system (discussed in Part 1.3). If higher temperatures are used, the piping system will have to be designed so that operators can gain access to different sections and clean out scale.

Priming the system may reduce costs over the life of the project. Priming involves heating reservoir derived water using the solar thermal system and then injecting it back into the ground without passing it through the building infrastructure. This could be done anywhere between one to three years after installation. KCRB's heating infrastructure requires a 49.3 °C inlet temperature and has an average outlet temperature of 33.8 °C, which means that the only waters above 33.8 °C can be considered useful. The temperature of the aquifer is 12 °C, which means that significant energy is needed just to get a sufficient quantity of water to the baseline of 33.8 °C. This can be done in one of two ways: 1) either the system can be oversized by ~300%, or 2) the system can be sized to ~125% and undergo a period of priming. If project developers were to build an oversized system, it would mean 3 times higher initial capital costs as well as

inefficient utilization, generating far more heat than is consumed on a yearly basis. However, any system designed to meet the full load of the building will have to be slightly oversized to mitigate cooling of stored water. Cooling will be reduced with time as injected hot water warms the reservoir and diminishes the thermal gradient between the fluid filled fractures and the surrounding rock.

Considering the thermal losses of the storage system, the heat generated by the solar array in the course of the year and the heating demands of the KCRB, an optimal pumping strategy has been determined for a system sized at 125% capacity. Analysis shows a system sized for 125% capacity should be storing thermal energy April through October and withdrawing energy from storage during November through March, Figure 34. The assumption that is being made during this analysis is that no supplemental heating will be used, and therefore there will be sufficient surface storage to meet the peak heating demand around 7:00 am.

Hour	Jan	Feb	Mar	Apr	May	Jun	Jul	Aug	Sep	Oct	Nov	Dec
1	-245.65182	-206.48044	-162.07651	-112.01399	-76.804663	-47.288139	-36.476591	-31.658291	-32.088809	-67.956127	-136.09703	-246.48789
2	-263.17731	-224.10759	-182.64858	-124.00627	-85.337964	-50.664659	-40.228013	-37.03078	-36.678392	-77.547835	-148.62582	-266.0937
3	-274.90001	-239.41192	-200.36901	-134.5643	-93.917778	-53.787868	-41.103984	-35.722343	-41.61353	-86.926418	-159.34712	-284.01892
4	-287.6279	-250.95529	-217.63638	-143.16284	-102.86135	-58.466795	-43.884064	-38.362141	-46.205294	-95.023431	-170.32015	-297.42546
5	-298.64182	-263.07221	-234.97768	-152.25845	-107.06006	-52.647121	-40.713456	-35.530507	-50.14777	-102.30648	-177.7029	-322.57719
6	-303.45491	-268.89457	-243.32227	-145.24876	-21.381512	31.5817298	51.2728807	-15.517418	-45.475555	-106.29766	-183.25937	-323.3427
7	-845.72906	-818.74699	-764.02301	-440.09051	-152.56325	-5.7561133	73.4881616	-76.735715	-223.99649	-452.71631	-646.70641	-927.49824
8	-642.05242	-583.62985	-450.47872	-128.99346	153.205749	229.836286	316.219589	148.033971	4.08295009	-254.74767	-470.39979	-765.93804
9	-474.8001	-383.08885	-172.26608	149.737103	479.8867	513.900672	691.93307	420.63162	336.962904	-22.798486	-289.81649	-565.59946
10	-239.11918	-129.98808	131.688397	468.698656	725.294551	673.711985	941.661868	728.120519	713.002839	237.743648	-80.827629	-337.03454
11	-81.841097	48.9506408	278.233959	549.787788	765.813358	801.869854	996.758617	885.335744	843.795202	418.3039	33.2081535	-186.04273
12	43.9216057	191.643428	350.523585	596.791347	853.468454	929.270545	1169.85002	920.496957	973.533976	602.649929	120.339721	-96.872872
13	65.5419026	233.557754	434.333159	598.220374	929.669818	896.728662	1217.928	1045.8689	980.07439	619.89867	169.11567	-49.584155
14	46.1910771	236.548335	427.134279	664.794317	909.387658	917.416134	1236.66264	1047.94799	961.140792	522.047649	129.551004	-71.870955
15	-16.466146	99.9984589	410.696799	597.878271	809.988588	852.475233	1144.39657	980.396986	926.396134	393.557541	4.26947125	-152.28098
16	-124.84637	26.8793936	260.458813	601.535793	783.671894	824.638322	1120.05547	957.500929	691.499729	226.971587	-80.596818	-230.82915
17	-264.86506	-140.15542	37.1296819	269.280601	513.509086	641.50722	894.815753	603.613431	347.100133	-27.373731	-211.73711	-328.50726
18	-345.62574	-284.2092	-166.32983	16.3255176	207.302586	318.561697	515.345655	246.550653	47.5660265	-154.80157	-267.13252	-378.77391
19	-385.1564	-335.38531	-268.07581	-167.96313	-19.278163	57.4827769	166.329424	-18.157466	-126.6481	-185.55227	-294.88641	-411.81437
20	-330.37484	-282.75013	-238.06071	-174.44578	-124.35841	-70.129744	-46.805856	-78.76906	-99.383933	-143.83385	-230.49419	-345.40321
21	-353.47325	-306.5789	-258.11481	-186.73438	-145.8718	-120.37496	-93.278738	-95.567664	-108.73952	-160.05751	-257.48279	-364.9165
22	-371.93872	-330.22825	-281.52814	-206.48023	-163.8858	-130.69543	-99.653991	-104.20311	-115.16846	-168.17729	-268.12084	-389.77133
23	-154.69362	-120.14517	-95.531985	-79.883935	-62.876653	-13.938193	-17.348413	-12.399125	-12.368341	-30.692444	-62.479699	-170.28457
24	-199.82937	-163.37194	-122.11428	-89.353167	-58.117662	-64.695091	-48.894803	-47.880919	-49.842626	-81.829242	-132.41257	-213.84919
Energy Stored	-6348.6106	-4493.6221	-1727.3551	2227.85056	5916.88337	7020.53701	10028.3298	7356.96315	5836.79826	802.534588	-3811.9616	-7726.8173
Pumping Direction	PFS	PFS	PFS	HWS	HWS	HWS	HWS	HWS	HWS	HWS	PFS	PFS

PFS	Pump From Storage
HWS	Heat With Solar

Figure 34. Cells in the table above show energy generated by the solar array minus the energy demands of KCRB. Additionally, months where energy is being stored or pulled out of storage are shown.

We consider solar arrays that are designed to generate 125% and 75% off the energy consumed by the building. This was done to get a look at the changes in cost and infrastructure required as the technology is scaled. Cost for each scenario is shown in Table 20. The 75% capacity design has lower upfront costs but will require heat exchangers and supplemental heating units in order to be properly integrated into the building infrastructure. The 125% capacity system will not require supplemental heating and may not require a heat exchanger as

well. However, meeting peak demand at 7:00 am only using a solar array may pose a significant engineering challenge.

It could require surface storage and pumping that can meet the demand peak to be economically viable. We identify this as a challenge given that any storage system being considered must store hot water up to 16 hours, through the night, minimizing heat loss. The cost of a storage system has not been calculated as part of this feasibility study.

If the project wishes to meet the full load of the build using only solar energy, which is possible in the 125% scenario, priming the storage system will be necessary. Priming involves heating reservoir derived water with the solar thermal system, and injecting it back into the ground without passing it through the building infrastructure. This could be done anywhere between one to three years after installation. KCRB's heating infrastructure requires a 49.3 °C inlet temperature and has an average outlet temperature of 33.8 °C, which means that the only waters above 33.8 °C can be considered useful. The temperature of the aquifer is 12 °C, which means that significant energy is needed to get the stored water in the aquifer to the target baseline of 33.8 °C.

Table 20. The cost of solar arrays that meet 75% and 125% of the heat demand of KCRB, assuming a 3-meter row spacing and at least 1.5 years of priming.

Output (Calculated) 125% Capacity	
Number of Panels needed	596
m^2 of footprint	3763
Cost	$ 3,046,798

Output (Calculated) 75% Capacity	
Number of Panels needed	358
m^2 of footprint	2258
Cost	$ 1,828,079

PART 4: MARKET TRANSFORMATION

Introduction

The overall objective of this report is to analyze the economic feasibility of Deep Direct-Use coupled with Reservoir Thermal Energy Storage (RTES) for district (or large facility) heating needs in areas underlain with permeable, low-flow aquifers (e.g., brackish or saline aquifers). In particular, this part aims to evaluate and document the market potential and economic feasibility for RTES technology implementation in Portland at a high level. We focus on understanding the market potential for application of RTES in the high population-density Portland downtown area, using the OHSU (Oregon Health Sciences University) campus as a case study to investigate the possible advantages and disadvantages.

This analysis will consider not only the costs of existing energy options in comparison to RTES, but also the potential environmental benefits/impacts and resiliency and reliability characteristics related to natural catastrophes. In addition to estimating the economic feasibility of a RTES system as part of an OHSU case study, we extend these results at a high level to ascertain the general market potential of applying geothermal technology to commercial buildings within Portland.

4.1 Geothermal Market Potential

Here, we explore the potential demand for geothermal energy in Portland's heating and cooling market. We look at both heating and cooling intensity and type of energy generation for different building types in various locations across Portland to guide our analysis surrounding the economic viability of geothermal as an alternative energy source for heating and cooling. Specifically, we use data from the Energy Information Administration's (EIA) Commercial Energy Building Consumption Survey (CBECS) to understand how each type of energy is used in commercial buildings within the Western United States, and then apply this data to different commercial building types in Portland using the Portland Commercial Energy Reporting (CER) survey.

Data Sources & Methodology

In 2015, Portland City Council approved a policy requiring owners of commercial buildings over 20,000 square feet to track and report annual energy usage. The program requires all buildings to use Energy Star Profile Manager to calculate energy use intensity (EUI), obtain an Energy Star score, estimate carbon emissions, and then report these findings to the City of Portland. The policy covers nearly 80 percent of the commercial square footage in Portland. The report does not include residential properties, places of worship, K-12 school buildings, or buildings that were granted exemptions. In the two years since reporting began, the city's Commercial Energy Report has collected data on building site and use characteristics, and energy use profiles on over 700 commercial properties.

For our analysis of geothermal market potential, we focus on two primary measures of energy use by buildings: site EUI and source EUI. Both measures are represented in thousand British thermal units (kBtu) per square foot of building space. Site and source EUI measures provide information on two aspects of building energy use: site EUI includes all energy used at the building's site while source EUI adds any additional energy required to transmit energy from the power generation source to the building. For example, site heating EUI measures the efficiency of the building's heating system, efficiency characteristics of the building such as insulation, and overall heating use. A building with a higher site heating EUI indicates a potentially less efficient heating system or a building that requires a higher heat output to maintain the desired temperature. As such, site EUI is the overall measurement of within-building energy demand. On the other hand, source heating EUI measures the efficiency of the system that provides energy to the building, including any energy lost through transmission, in addition to the within-building energy efficiency.

In this analysis, we consider both site and source EUI for heating and cooling. While the CER includes measurements of total EUI, it does not collect data on the amount of energy used specifically for temperature regulation. To analyze heating and cooling use, we make assumptions based on information collected by the US Energy Information Administration (EIA).

Most recently conducted in 2012, the EIA Commercial Energy Building Consumption Survey (CBECS) gathers information on the energy consumption of 6,720 commercial buildings from across the US. Along with building characteristics, the survey gathers information on the end uses of four potential energy sources within the building: electricity, natural gas, fuel oil, and district heat. Usage from each source is then separated into the amounts used for different purposes. These purposes include lighting, heating, water heating, cooling, refrigeration, ventilation, cooking, office equipment, computing, and miscellaneous. In our analysis, we only include energy categorized as heating and cooling, excluding any potential crossover between cooling and ventilation or refrigeration. From this data, we calculate the share of energy used specifically for heating and cooling buildings from each energy source. To ensure the information from the CBECS is representative of the climate in Portland, Oregon, we limit the sample to buildings in the Western US Census region. Assuming that similar types of buildings (e.g., offices buildings or hospitals) have similar energy profiles, we incorporate the shares of energy used for heating and cooling by building type into the CER data. For example, if office buildings in the Western US use 65% of their natural gas and 5% of their electricity for heating, we assume office buildings in Portland use energy in similar proportions. By scaling energy use with the share of energy used for heating or cooling, we get an estimate of the total amount of energy that buildings within Portland's CER use for these purposes, and thus the heating and cooling EUI.

Incorporating the CBECS use statistics into the CER data required matching the classifications of building types across the two data sources. Because of inconsistencies between

building type definitions or insufficient sample size of buildings within certain building classifications to calculate representative averages, we limit our building energy profile analysis to six types – offices, hospitals, colleges, hotels, groceries and retail, with all other types combined into an Other category.

Limitations

We would like to note a few potential issues in our combined analysis of the Portland CER data and the EIA CBECS data. While the CBECS collects data on energy consumption from four sources, the CER collects data only on electricity and natural gas consumption. However, the shares of energy used for heating and cooling are similar whether using the two sources available in the CER or all four sources. This suggests that the EUI calculated using the CER's available data are representative of actual heating and cooling use as analyzed in the CBECS.

The second potential issue arises in the conversion factors for site and source EUIs. According to the Energy Star program, the standard factors for converting site EUI to source EUI are 1.05 for natural gas and 2.80 for electricity. These indicate that for every unit of energy transferred to the site, 0.05 units are lost for natural gas and 1.8 units are lost for electricity. However, our analysis of CER data suggests that the factors for Portland are 1.13 for natural gas and 3.13 for electricity, indicating that Portland's energy transmission systems are less efficient than Energy Star's stated national average. To remain consistent with the industry standard and avoid overestimation, we use the values provided by Energy Star to calculate source EUI, which is site EUI adjusted for energy lost in transmission to the building. If the higher factors are preferred, the CER's site-to-source factors suggest a 7.5-12.5% increase in source EUI from what our analysis states below.

Finally, a number of buildings were left out of our analysis due to missing information on energy usage of electricity, natural gas, or both. The majority of these buildings were missing information on natural gas use. One possible result of this missing information is that our analysis more heavily represents buildings with both natural gas and electricity access. However, the site-to-source EUI factors above indicate a large disparity in efficiency between electricity and natural gas systems. As such, any building with heating and cooling systems primarily powered with electricity is a good candidate for a more efficient system.

Building Energy Usage Analysis

Our analysis includes 613 commercial buildings within Portland with over 20,000 square feet of Gross Floor Area (GFA). Table 21 presents the overall averages of site and source EUI and share of energy used for heating and cooling, as well as these values across building type. The average building uses 20.4% of its energy for heating and 8% for cooling. The average site EUI for heating and cooling are 22 and 5.2, respectively, indicating that heating demand greatly exceeds cooling demand. However, comparing site and source EUI, the large difference between

Table 21. Summary Statistics of Energy used for Heating and Cooling Purposes by Building Type

Category	Number of Buildings	Share of Total Energy Usage		Site EUI (kBtu/sqft)		Source EUI (kBtu/sqft)	
		Heating	Cooling	Heating	Cooling	Heating	Cooling
Offices	253	20.0%	10.0%	17.8	5.5	20.5	15.5
Hospitals	5	23.9%	10.8%	37.7	15.3	40.1	38.1
Colleges	41	35.3%	7.0%	20.2	4.0	22.7	10.9
Hotels	57	4.9%	5.0%	5.9	3.8	7.5	10.6
Groceries	41	10.7%	1.7%	36.6	3.2	40.2	8.8
Retail	38	24.0%	8.1%	14.9	4.0	17.5	11.2
Other	178	23.7%	8.5%	31.2	5.7	35.5	16.1
Overall	613	20.4%	8.2%	22.0	5.2	25.1	14.4

site and source EUI for cooling and relatively smaller difference for heating, suggest that the majority of cooling energy comes from electricity and a majority of heating comes from natural gas.

Colleges have the largest share of energy used for heating, consistent with previous research outcomes. In a study of campus energy consumption, Jafary et al. (2016) found that around 28% of college campus energy usage goes toward heating. Generally, college campuses have similar energy use to office buildings and retail spaces (other locations where people spend large amounts time), but are generally closed in the late evening and early morning. Hospitals and retail buildings also have relatively high heating use. Hospitals typically operate during all hours of the day, and seek to maintain a comfortable temperature for patients and staff. This type of continuous operation directly contributes to higher heating energy use.

With site and source EUI values nearly double that of other building types, both hospitals and grocery stores either keep their spaces much warmer than other building types or have inefficient systems. For hospitals this could speak to the need for comfortable spaces for long hours, but a heating source EUI of 40.1 also indicates room for efficiency improvement. Grocery stores high EUI values could stem from their need to heat large open spaces, but, as with hospitals, a source EUI above 40 indicates room for improved efficiency. Contrary to our expectations, hotels have a remarkably low share of energy used for heating. One possible explanation for this finding is that a large amount of energy at hotels is dedicated to laundering or heating pools. However, we also find that hotel source heating EUI is much lower than that of

other building types. As such, we hesitate to draw any conclusion based on these findings until we have a better explanation for this low statistic from the CBECS data.

In the West Census region, cooling accounts for a significantly lower share of total energy than heating. Cooling share accounts only for energy used for space cooling, while other types of cooling such as refrigeration receive their own category. Hospitals, office buildings, and retail spaces, respectively, use the highest portion of their total energy use on cooling, but each use less than half the amount on cooling as they do on heating as is expected in a temperate climate. All building types, outside of hospitals, have site EUI under 6, suggesting low levels of cooling need compared to heating. All building types have cooling source EUI more than double cooling site EUI, indicating inefficient cooling systems relative to heating.

Figure 35 displays average site heating EUI across the Portland area by neighborhood. The average heating site EUI for all commercial buildings in Portland is 22 kBtu/ft^2. All green areas on the map indicate lower than average EUIs and more efficient heating, while orange and red indicate less efficiently heated buildings. Most notably, site EUI is highest in the industrial areas south of the Portland International Airport, including the Sunderland, Cully, Concordia, Roseway, and Sabin neighborhoods. Other high EUI neighborhoods include South Tabor, Cathedral Park, and Homestead. These areas contain low numbers of commercial buildings, and their EUI is dominated by either a few unique outliers, such as higher than average reported energy use in grocery stores and hotels.

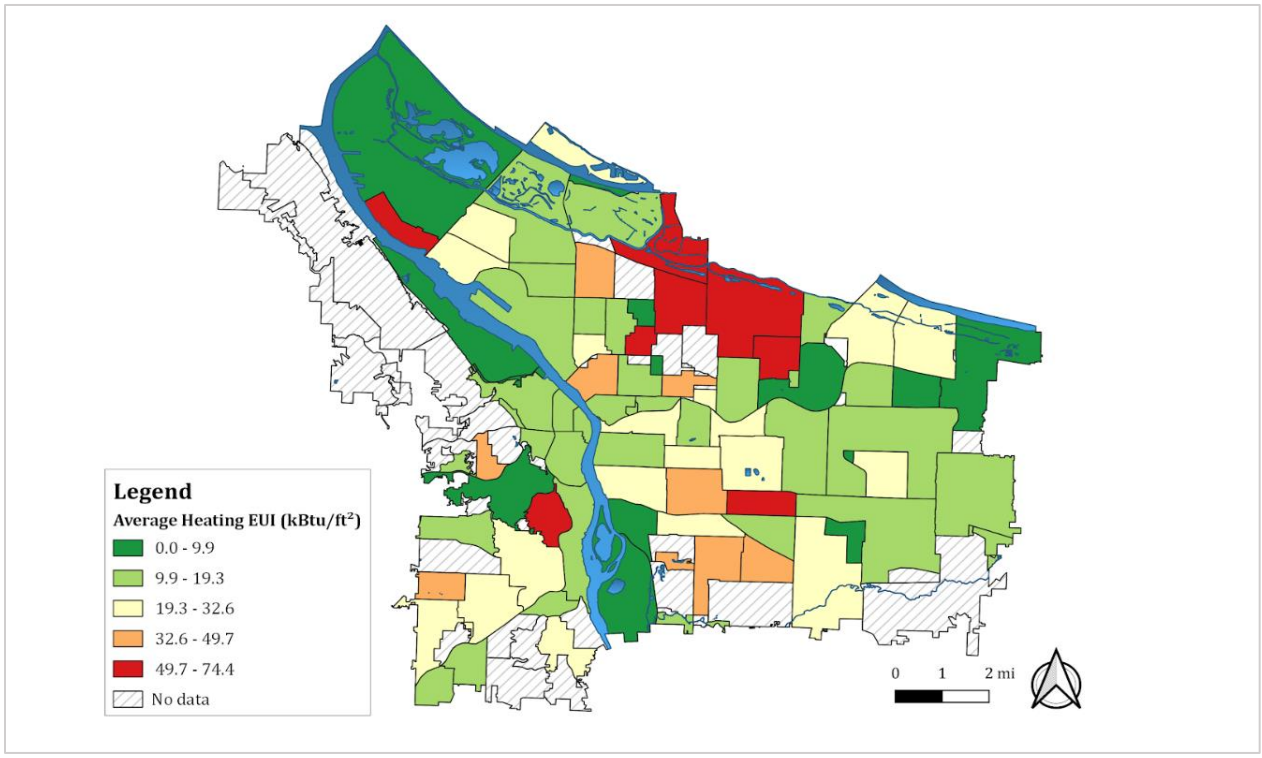

Figure 35. Average Site Heating EUI by Neighborhood

Figure 36 includes source heat EUI by neighborhood, displaying the total energy required for building heating. This adjustment increases the average from the site EUI average of 22 kBtu/ft^2 to the source EUI average of 25.1 kBtu/ft^2. This is largely due to the relative inefficiency of electrical transmission. The largest change is for the Mt. Scott-Arletta neighborhood. The high site EUI visible from neighborhoods in Figure 1 change only slightly, suggesting higher amounts of natural gas use.

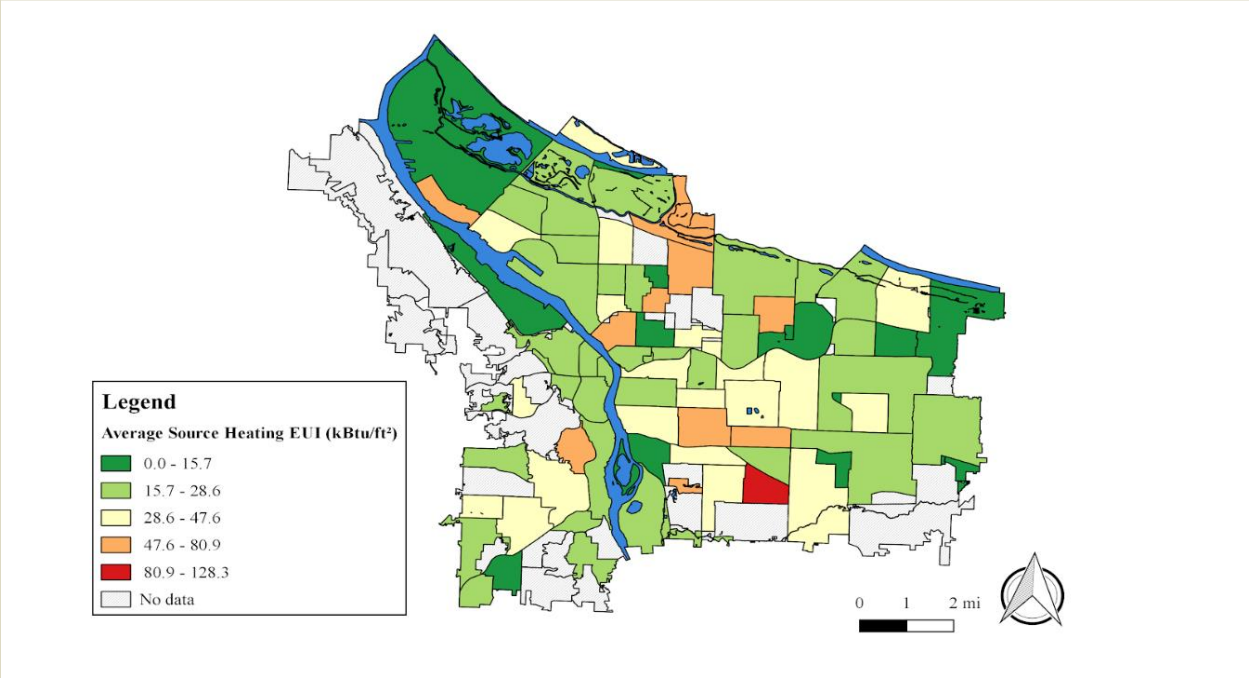

Figure 36. Average Source Heating EUI by Neighborhood

Figure 37 shows the distributions of site heating EUI by building types. As mentioned above, site heating EUI represents the three factors of within-building heating demand: system efficiency, building efficiency, and heating use. Average site heating EUI is highest for hospitals and grocery stores. Except for these types and the Other category, the average site EUI is below the overall average of 22 kBtu/ft², falling around 14 kBtu/ft². The lowest average source EUI is for hotels, at 5.9 kBtu/ft².

While site heating EUI for other types are closer to the average, site heating EUI for hospitals and grocery stores remains 10 kBtu/ft² higher than any other type. Furthermore at 37.7 kBtu/ft², heating EUIs for hospitals are nearly double the average. The abnormally high EUI for hospitals, coupled with higher than average square footage, suggests that they may be the well suited for geothermal systems. On the other end of the spectrum, heating EUI for hotels is 5.9 kBtu/ft². This is an interesting finding, considering that heating rooms would seem to be the largest use of energy for hotels. Possible explanations for the low share of energy used for heat could be that laundry machines or heating pools make up the majority of energy used.

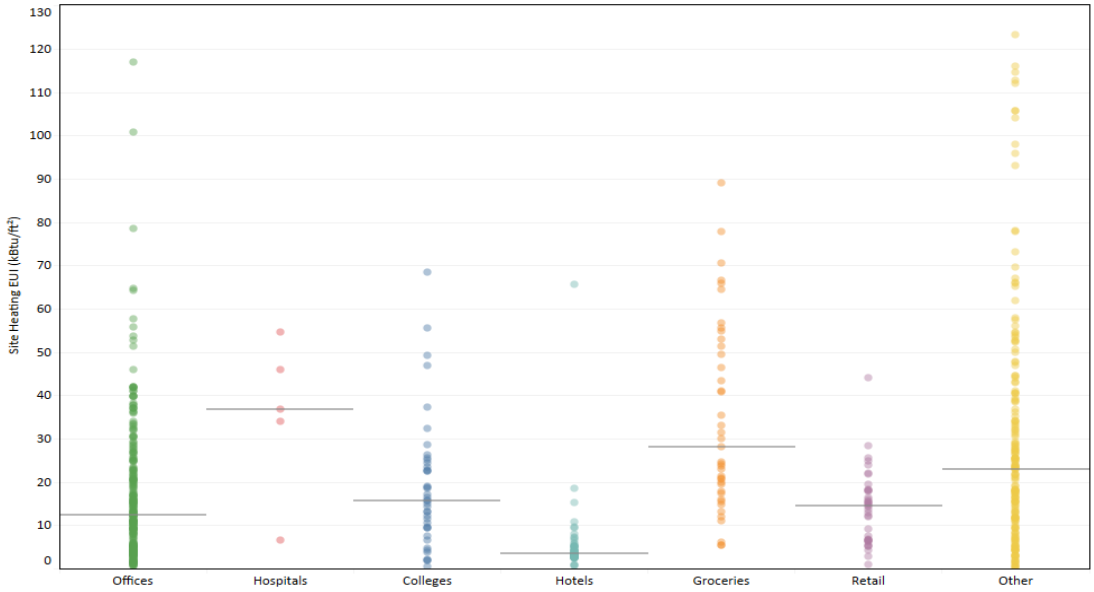

Figure 37. Site Heating EUI by Building Type.

However, this does not explain the disparity between hotels and similarly occupied building types such as offices, with over three times the heating EUI of hotels.

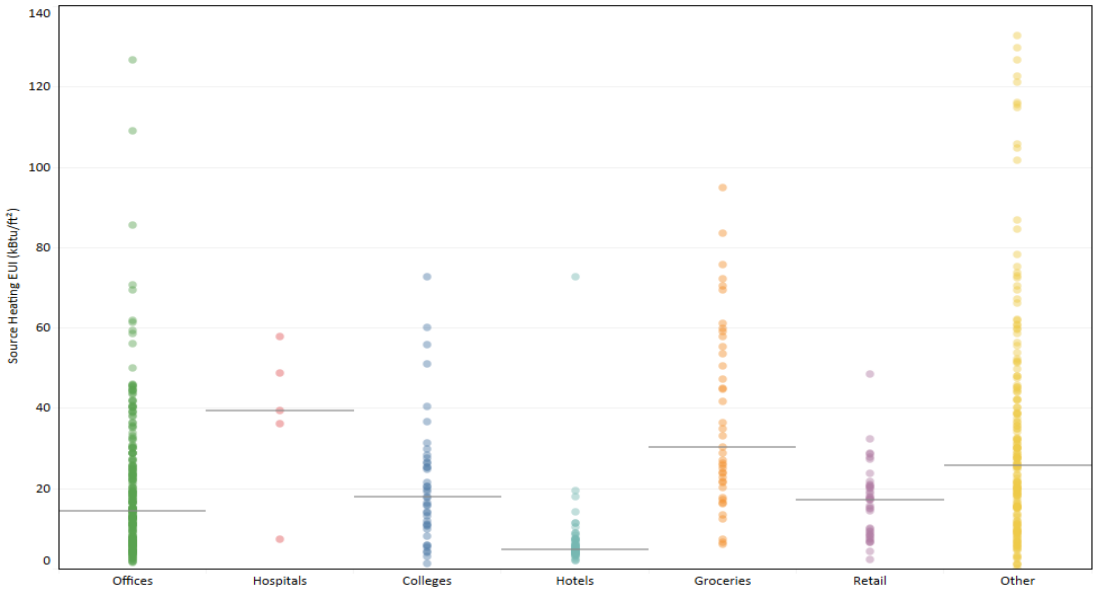

Figure 38. Source Heating EUI (kBtu/sqft) by Building Type.

Adjusting the heating EUI for energy loss from source to site results in little difference between Figure 37 and Figure 38. This is largely due to the majority of heating energy coming from natural gas. The largest shift comes in the hotel building type, which have the highest natural gas-to-electricity use ratio. The other types have a nearly uniform shift of between 2 and

3 kBtu/ft^2. As there are only minor changes and to account for all factors of energy use, we report on only source heating EUI in all proceeding figures.

Figure 39 displays heating EUI distributions by building size (categorized by square-footage). While the graph generally points toward a larger grouping and wider distribution of buildings in the 25,000-50,000 ft^2 category, the mean of the category is near the overall average. The means of source EUI for each category do not tend to increase with building GFA. This suggests that buildings with higher square footage do not require higher energy usage per square foot of space. Figure 40 shows the comparison of source heating EUI across the year in which the building was constructed. Though there are slight variations in average heating EUI over time, all fluctuations lie within one or two standard deviations. We conclude that there has been no increase in the heating requirements per square foot of the building space. When considering only hospitals, the trend suggest a decrease in heating requirements. However, a smaller sample size of hospitals limits the statistical significance of this finding. For all building types with enough buildings to establish significance, there is no relationship between building age and heating requirements. While this finding seems counterintuitive considering recent trends in energy efficient buildings, older buildings with less efficient heating systems may be the first to be retrofit with a new heating system, leading to little difference across time.

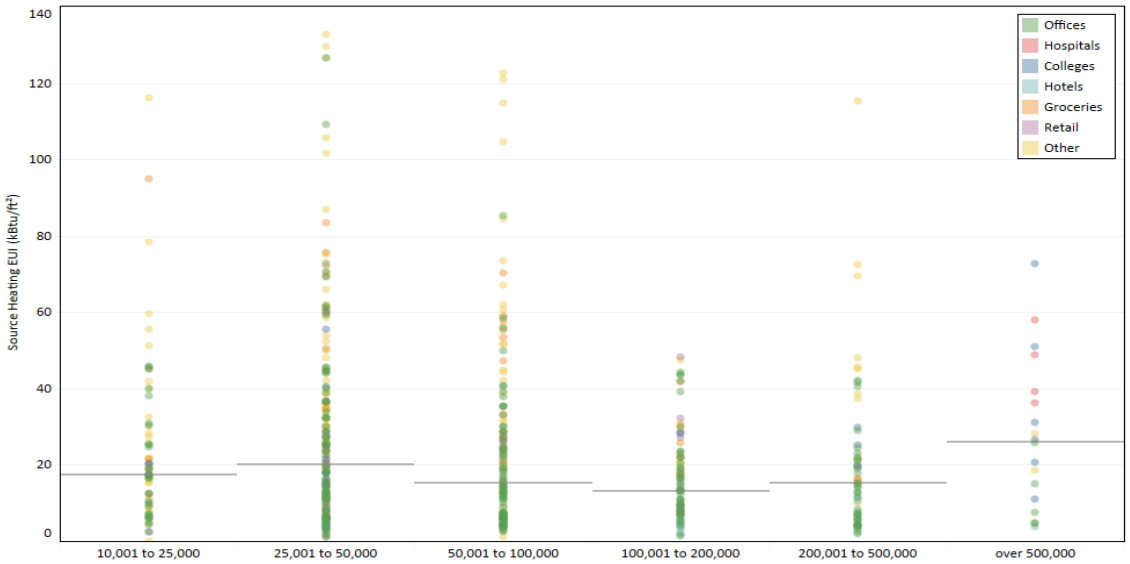

Figure 39. Source Heating EUI by GFA (Gross Floor Area – square feet)

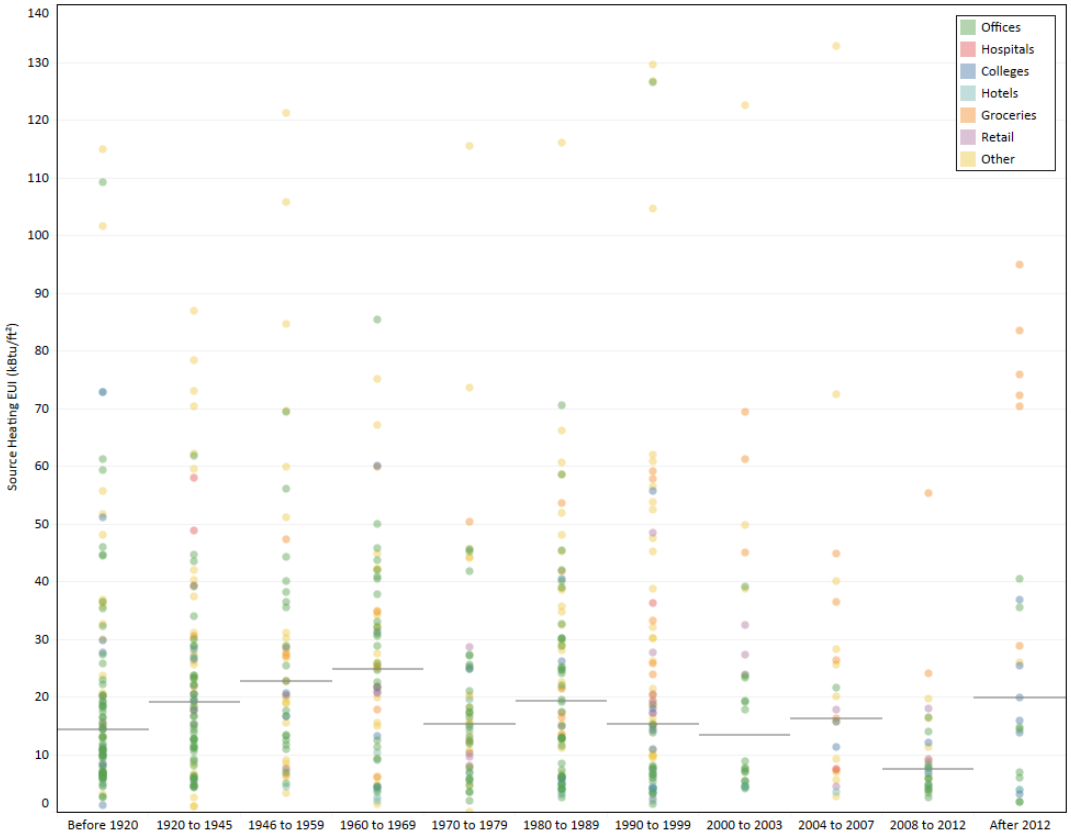

Figure 40. Source Heating EUI by Year Built.

Figure 41 displays heating energy use and Energy Star score, a measure of how the building is expected to perform, relative to their averages. As a result, the four sections of the graph separate the buildings into categories based on their predicted and actual energy use. The upper-left quadrant are those buildings that were more efficient and were predicted to be more efficient (i.e. low heating EUI and high Energy Star scores). In total, 50.3% of buildings were within this favorable category, largely made up of lower energy use building types such as office buildings. Conversely, 11.9% of buildings were predicted to perform poorly, and actually did perform poorly. Over half of grocery stores and five of the six hospitals within the Portland area fall into this category.

The other two categories are buildings that performed differently than their Energy Star score predicted. While 14.3% had a low Energy Star score and a better than average EUI, indicating better performance than expected, 23.6% of buildings had high EUI despite having a higher Energy Star score. One possible explanation for this finding is that buildings given a higher Energy Star score may do less to reduce their actual energy use.

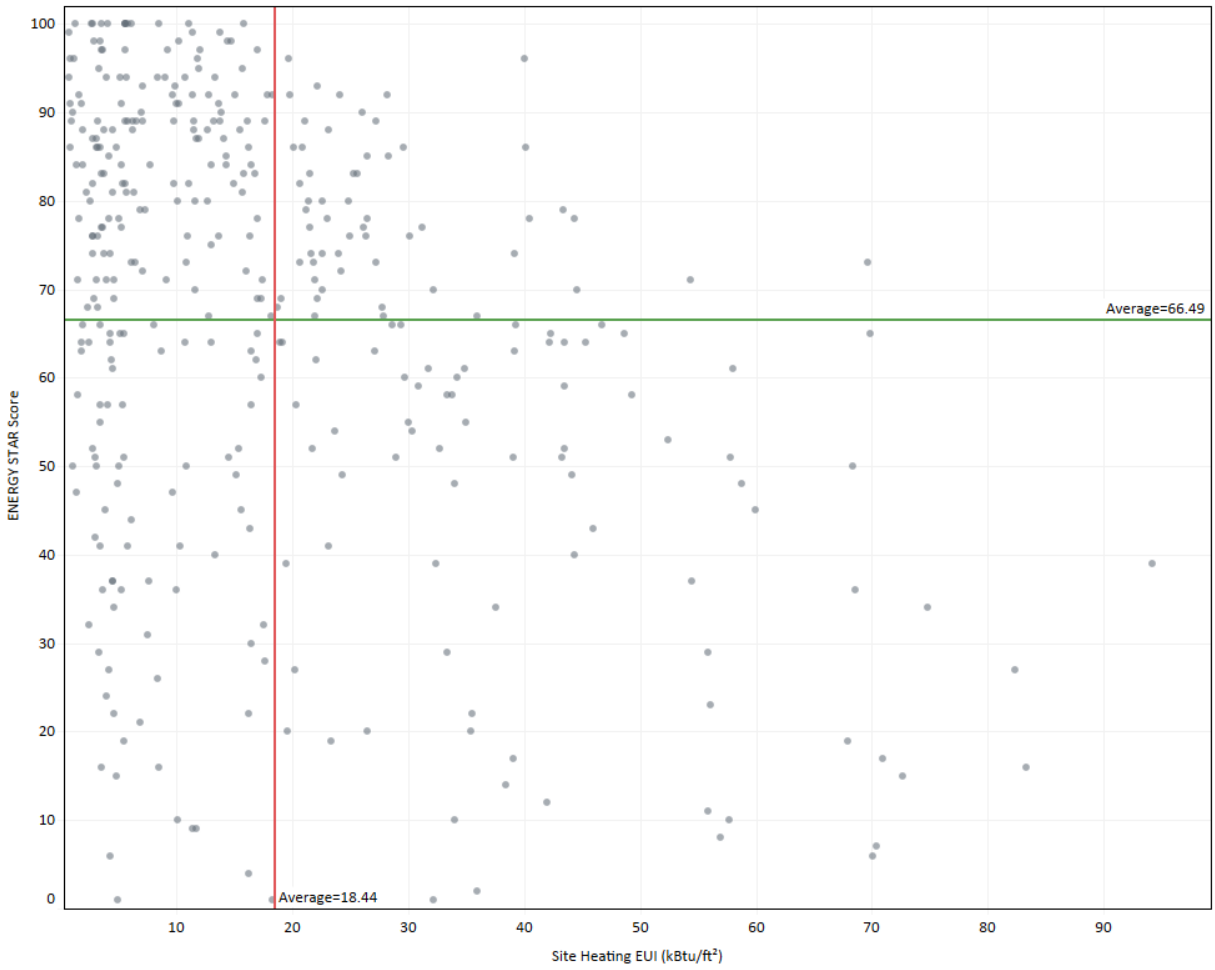

Figure 41. Energy Star Score and Site Heating EUI (kBtu/sqft)

Depending on the capability of the system, geothermal energy systems may also be able to provide cooling to the buildings. To evaluate potential improvements in cooling energy use, we compare source cooling EUI across building types and year built. As mentioned above, there is a substantial increase in source cooling EUI due to cooling systems being powered with electricity. This is most notable for hospitals. Despite having much lower site cooling EUI than site heating EUI, source cooling and heating EUI for hospitals comparable at 38.1 and 40.1, respectively. The next highest source cooling EUI for building types is 40% of that of hospitals, again supporting the finding that hospitals are a primary candidate for system improvements.

Figure 42 presents source cooling EUI grouped by year built. Similar to the across-time analysis conducted for source heating EUI above, we find that cooling energy use is not clearly related to the age of the building.

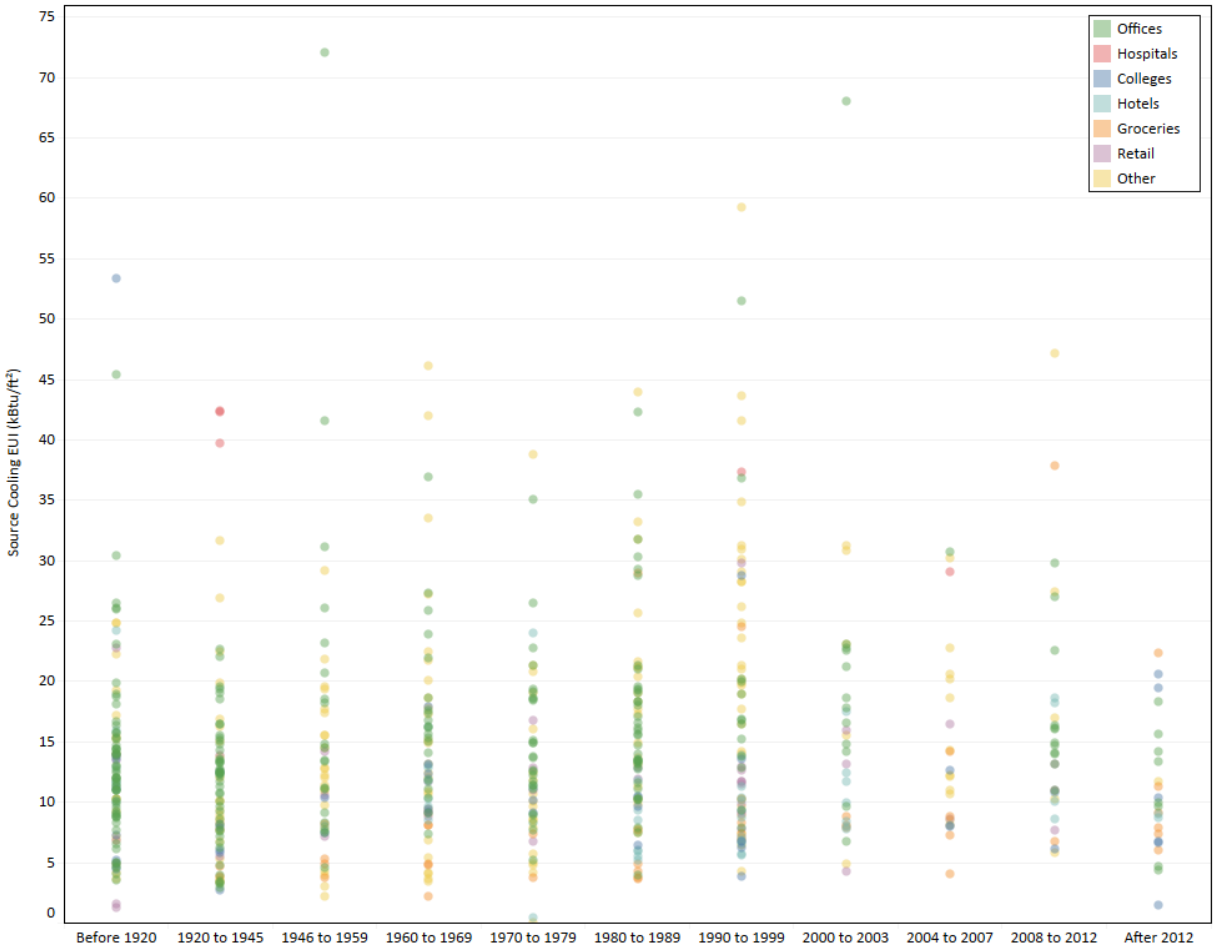

Figure 42. Source Cooling EUI by Year Built

Geothermal Market Potential

Any conclusions for the market potential of geothermal largely depend on the potential geothermal heat or cooling output for each location. However, even without information on each location's energy potential, our findings suggest a general framework on the types of buildings with possible efficiency improvements that could be met with a RTES system. The majority of the variation in energy use is determined by the building type. In particular, building types with high energy demand to keep occupants comfortable, namely hospitals, colleges, and grocery stores, appear to be good candidates for geothermal projects. Buildings or campuses over 500,000 square feet in size may also benefit from a more efficient energy system, especially considering the cost of improvements may be smaller relative to the value of the building(s). Economies of scale may further benefit campuses or groups of buildings where one geothermal system (or a district geothermal system) can feed into multiple buildings, sharing large fixed costs. Furthermore, any building with predominantly electric heating and cooling systems could see substantial improvements to efficiency with a geothermal system.

4.2 Economic Feasibility Analysis

This section assesses the viability of deep direct-use reservoir thermal energy storage (RTES) in the Portland Metro area by comparing it with the most common methods of building heating and cooling currently in use. We first outline and explain the most common metric for energy cost comparisons - levelized cost of energy (LCOE), how it is typically calculated, and why it is important for comparing different types of energy use and storage projects. Then, we compare the environmental impacts, reliability and resiliency, and market barriers between RTES and other heating methods.

Levelized Cost of Energy (LCOE)

To compare deep geothermal to other types of heating systems, a uniform metric is needed. The most common metric for comparing energy systems in both the academic and professional literature is known as levelized cost of energy (LCOE). This calculation allows decision makers to compare lifetime costs of different types of energy generation systems (solar, geothermal, coal). The most basic form of an LCOE calculation is the sum of all of the costs of installing and operating a system over the expected life of the system divided by the lifetime energy generation of a system. An example of a general LCOE equation can be seen in Equation [1], similar to Equation [2] from GEOPHIRES v2.0 (Beckers and McCabe, 2018) which assumes that all capital costs occur in the first year.

$$LCOE = \frac{\sum_{t=1}^{n} \frac{I_t + M_t + F_t}{(1+r)^t}}{\sum_{t=1}^{n} \frac{E_t}{(1+r)^t}} \qquad [1]$$

where t = years, I = investment expenditure, M = operating & maintenance expenditure, F = fuel expenditure, E = energy generation and r = the real discount rate.

$$LCOE \text{ or } LCOH = \frac{C_{cap} + \sum_{t=1}^{LT} \frac{C_{O\&M,t} - R_t}{(1+d)^t}}{\sum_{t=1}^{LT} \frac{E_t}{(1+d)^t}} \quad [\text{¢}\, kWh^{-1} \text{ or } \$\, MMBtu^{-1}] \qquad [2]$$

where C_{cap} = Capital Cost ($), $C_{O\&M}$ = O&M Cost ($), d = Real discount rate (%), E_t = Energy Production (MWh), LT = System Lifetime (years), R_t = Secondary Revenue Stream ($) and t = Time (years).

Levelized cost of energy (LCOE) and levelized cost of heating (LCOH) are present value calculations to evaluate the per unit cost of energy or heat for a generation system over the course of an assumed lifetime (EIA, 2018). One kilowatt hour is equal to approximately 3,412 British thermal energy units (btu) (American Physical Society, 2018). Kilowatt hours are a more general measurement of energy while British thermal energy units refer specifically to heat. For the remainder of this report we will use LCOE using the conversion whenever necessary.

LCOE is an attractive tool for decision makers as it allows for direct comparison across various types of generation projects. It provides a single number—the per-unit cost of a particular energy source—that can be compared across all energy generation systems. It is one of the most common measurements used for such comparisons. The Energy Information Administration describes LCOE as, "an often cited measure of the overall competitiveness of different generation technologies." Additionally, both the National Renewable Energy Laboratory (NREL) and U.S. Department of Energy have LCOE calculators accessible on their websites. The LCOE of a geothermal system can be compared directly with the LCOE of a solar or coal generation system. Figure 43 and Figure 44 from Lazard (2018) "Levelized Cost of Energy Storage" provide a snapshot for comparing the LCOE's of various types of energy generation. Figure 43 compares the unsubsidized LCOEs of alternative and conventional energy sources while Figure 44 compares the LCOEs of alternative energy sources with their subsidized counterparts. Due to variability across projects for both cost and energy generation, the Lazard (2018) figures provide a range of LCOE possibilities for all energy generation types.

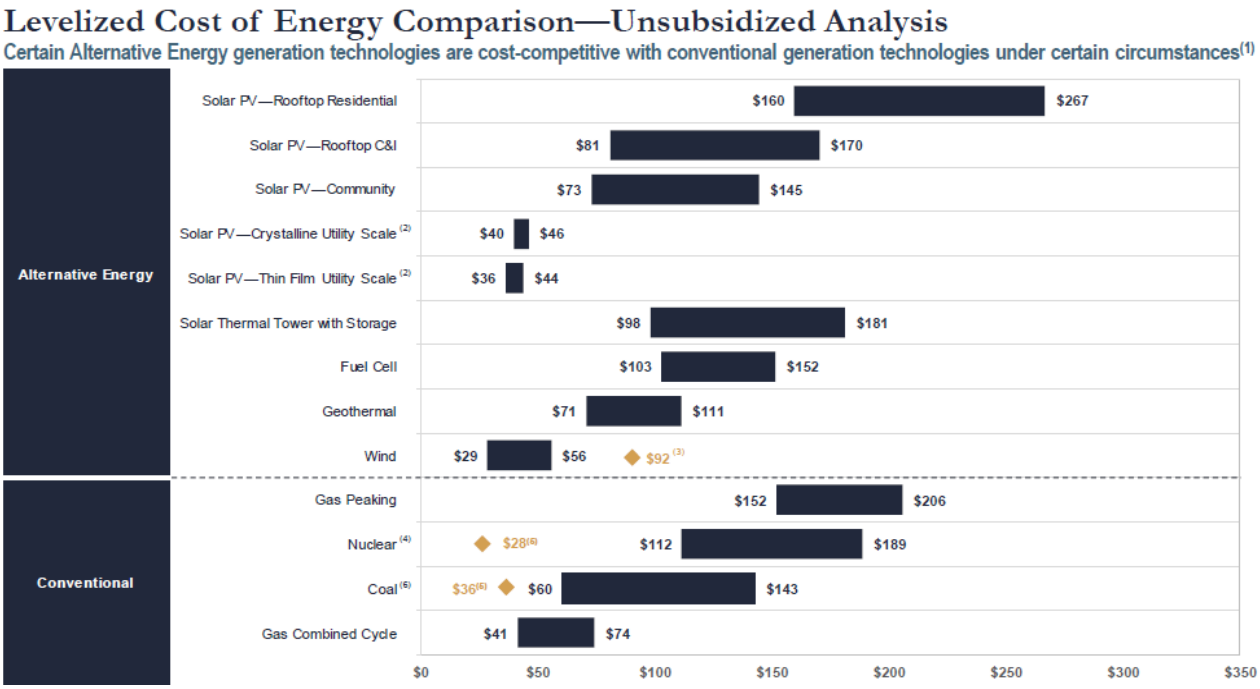

Figure 43. Levelized Cost of Energy Comparison ($/MWh) - Unsubsidized Analysis (Lazard, 2018)

There are a few tools currently available to perform LCOE calculations. NREL, has a basic tool where the user specifies only eight engineering and financial variables to estimate an LCOE for any time of generation project. They also have a dedicated team that has created a program called GEOPHIRES dedicated specifically to generating LCOE values for geothermal projects. GEOPHIRES has 96 variables, but according to Beckers and McCabe (2018), only a handful are likely to change from project to project.

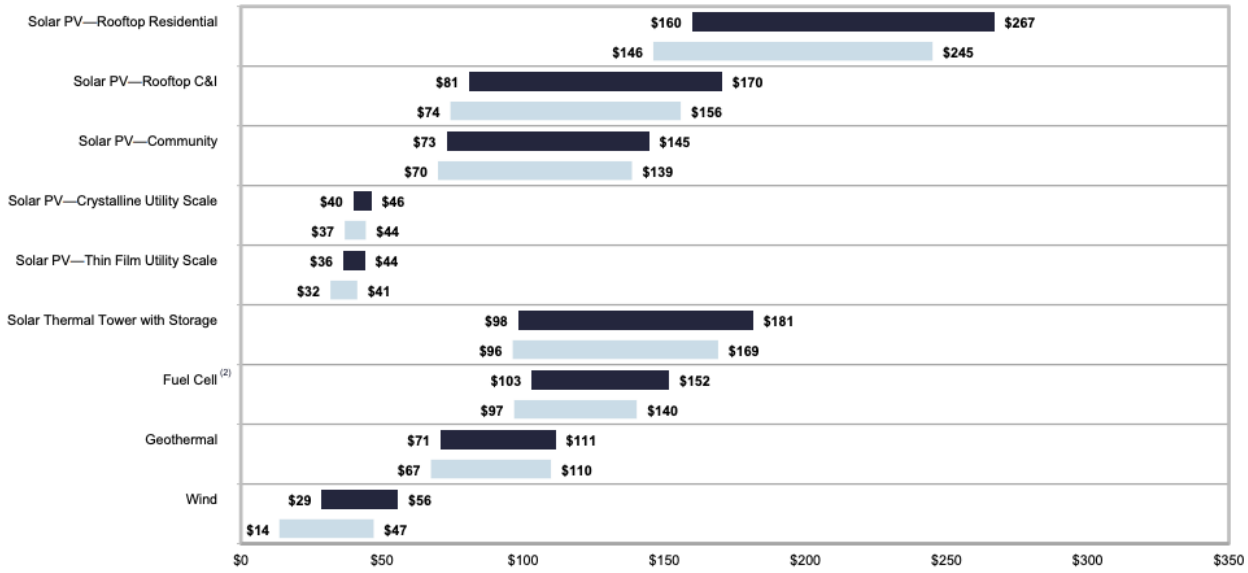

Figure 44. Levelized Cost of Energy Comparison ($/MWh) – Subsidized Analysis (Lazard, 2018)

A variety of stakeholders including engineers and project managers must collaborate to compile all of the relevant information for any LCOE calculation. Debt structures and other information about operating and capital costs are necessary to determine the lifetime cost, and information about the inputs necessary for energy generation are key for determining total output. Others use a simpler set of assumptions when calculating LCOE. The LCOE analysis in Lazard (2018) makes 9 key assumptions when calculating LCOE including total system output, total capital costs, fixed and variable operating costs, heat rate, capacity factor, fuel price, construction and facility life.

LCOE calculations require specific engineering information for each deep geothermal project to estimate the lifetime generation for a specific system. To calculate a more precise LCOE for a particular project details about the nature of both costs and energy generation are needed. For example, both debt from capital expenditures, equipment depreciation, and expected system life need to be accounted for in system costs, and the capacity factor, depth of the well, and heat of the earth at the specified depth need to be considered for energy generation.

While the estimation tools can provide adequate LCOE estimates, direct estimations from a project team can be used instead of built-in calculators. NERC uses a combination of financial and engineering inputs provided by project managers to calculate LCOE. Each input is given on an annual basis. The sum of all financial inputs over the expected lifetime of the system is divided by the sum of the annual net system energy output, calculated from project specific engineering inputs. Table 22 summarizes the required input variables and assumptions that our team used to calculate LCOE.

Table 22. Levelized Cost of Energy (LCOE) Calculation Input Variables

Variable	Units	Assumption	Source
Construction Time	Years	1	Team experts
System Lifetime	Years	25-35	Team experts
Nominal Discount Rate	%	3.00%	Li and Pizer (2019)
Expected Annual Inflation	%	2.20%	Federal Reserve 10-year inflation forecast (as of 11-2018)
Real Discount Rate	%	0.80%	Real Discount Rate = Nominal Discount Rate – Expected Annual Inflation
Base Energy Output	kWh per year	1,212,735 – 1,845,164	Solar providing 75% and 125% of building load
Nominal Operating Costs	$ / year	$34,764	Pumping rates vary according to flow rates. Assumes $0.10/kWh electricity cost
Nominal Capital Costs	$	$3,310,824 - $4,529,543	Varies based on solar capacity assumptions (75%-125% of heating)
Capital Cost Dispersion	Years	1	Team experts

Environmental Impacts

Deep direct-use geothermal is a renewable, environmentally friendly method of generating heat compared to conventional systems in the Portland Metro Area. The idea of using direct-use deep geothermal is not a new one. The Department of Energy (OEERE, 2) cites a paper by Tillman (1980) that notes as early as the 1980's that direct-use deep geothermal was "economically competitive with conventional fuels for use in direct heat applications." Not only is it starting to become more economically viable, but it also has less environmental impact than most common heat generation systems. The same Department of Energy article goes on to explain that deep geothermal could replace U.S. dependence on fossil fuels for heating and cooling. Although deep geothermal's potential has been known for years, it has not developed into a mainstream technology. Tester et al. (2006) conclude that large scale adoption of direct-use deep geothermal in the U.S. has been unrealized due to a combination of lack of institutional support and high capital costs. To explore geothermal's viability as a replacement for mainstream heating systems, we compare the environmental impacts, resilience, and reliability of common energy generation systems to that of deep geothermal in the following sections.

In Oregon, most heating systems run on direct natural gas, electricity, or some combination of the two. According to the Oregon Department of Energy (2018), electricity, natural gas, and petroleum make up over 90 percent of Oregon's energy dedicated to heating. Both natural gas and electricity generation have negative environmental impacts. While natural gas is often touted as a cleaner alternative to coal, and the largest portion of Oregon's electricity comes from hydro, a renewable resource, the Northwest Power and Conservation Council (2018) conclude that both sources of heat energy still create negative environmental impacts.

Both producing and burning natural gas can generate negative environmental impacts. Natural gas is a fossil fuel, and thus its combustion releases greenhouse gasses into the atmosphere. However, it is significantly less detrimental to the environment than coal. It emits 50 to 60 percent less carbon dioxide compared to coal (NREL, 2010), and when used in vehicles emits between 15 and 20 percent less heat trapping gasses than gasoline when used for fuel in cars (fueleconomy.gov, 2018). While natural gas for direct use and for electricity generation may be an improvement from coal, the amount of CO_2 emitted from natural gas combustion is still relatively high. A paper by Jaramillo et al. (2007) on comparative life cycles of various fuel types uses an emission factor of 120 pounds of CO_2 equivalent per MMBtu for natural gas compared to 205 pounds of CO_2 equivalent per MMBtu for coal. While the combustion of natural gas emits less CO_2 than that of coal, a sizeable amount is still released during combustion. However, the environmental impacts of natural gas come largely from its production.

In 2018, a once unconventional but now prominent form of producing natural gas called hydraulic fracturing or "fracking" accounts for a large portion of the detrimental environmental impacts. The EIA (2018) explains fracking as a process where chemically infused water is pumped into shale, sandstone, and other carbonate rock to release raw natural gas. They continue to explain that this process produces a variety of negative outcomes including: groundwater pollution, the release of hazardous chemicals, and the escape of natural gas directly into the atmosphere. Groundwater pollution, both by fracturing fluid and methane, the primary component of natural gas, reduces clean water availability. A paper by Haluszczak et al. (2013) published in Applied Geochemistry studying fracking in Pennsylvania concluded that improper disposal of fracking fluid can cause concentrations of harmful chemicals well above the threshold for legal drinking water. Fracking has also been associated with increased seismic activity. Researchers in both the U.S. and U.K. (2013, 2012) found that disposing hydraulic fracturing fluid into deep Class II injection wells has been associated with earthquakes large enough for detection at the Earth's surface (Royal & NRC, 2013). Methane leakages from fracking sites and transportation are also major environmental concerns. In 2011, Howarth et al. concluded that between 3.6 and 7.9 percent of natural gas escapes into the atmosphere during fracking, and that at this range the long run greenhouse-gas footprint of natural gas may be as environmentally detrimental as coal.

Electricity generation comes from a variety of sources in Oregon including natural gas, hydro, coal, wind, and solar (Figure 45). Each of these sources have drastically different levels of environmental impact. Hook and Tang (2013) are among the many who point out that fossil fuels emit greenhouse gases into the environment and are significant contributors to climate change. Hydro, wind, and solar power, while both clean and renewable in their uses come with other social and environmental impacts. The infrastructure for hydropower requires the construction of dams that often reshape landscapes affecting tangential communities and wildlife.

For example, according to Church et al. (2016), the 1957 construction of The Dalles Dam permanently submerged fisheries and land belonging to native communities that had been in use for hundreds of years. Dams negatively impact fish populations in a number of ways. A Northwest Power and Conservation Fish Division Report points out that dams inundate spawning grounds, change historical river flows, and raise water temperatures all of which make it harder for fish to spawn. Wind power also impacts wildlife. Erickson et al. (2014) estimated that hundreds of thousands of birds and bats die annually from accidental collision with wind turbines, especially during migration periods. As the area used for wind power expands, this could be a growing concern. Solar power has very few detrimental environmental impacts, but as of now is not a viable and reliable source for industrial electricity generation in Oregon. A 2018 report by the Northwest Power and Conservation Council concludes that in aggregate, the average electricity generation mix in Oregon produces slightly more CO_2 per kilowatt hour than using only natural gas.

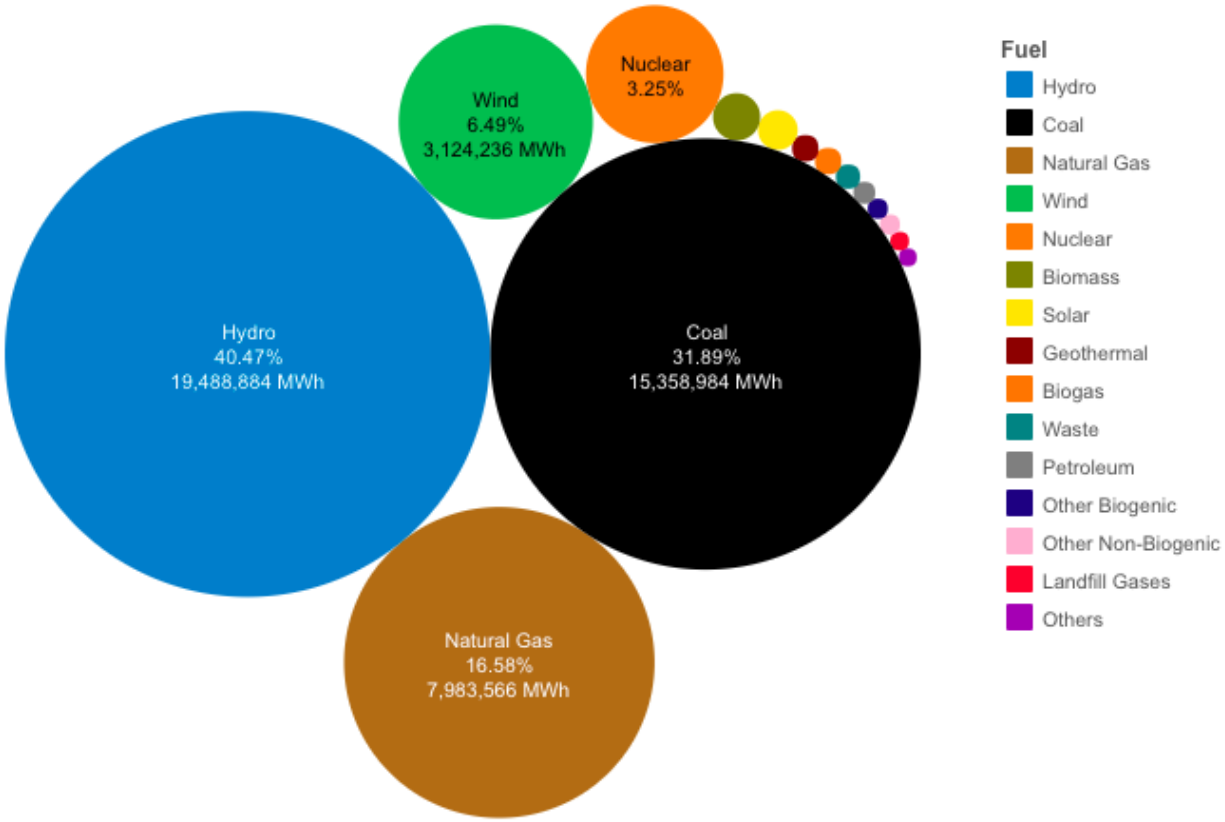

Figure 45. Fuels used to Generate Electricity in Oregon by percentage and MWh (2014-2016) (ODOE, 2018)

Deep geothermal environmental impacts are significantly lower than natural gas and the average electricity generation mix. While deep geothermal projects have occasionally been associated with releasing small amounts of harmful gasses from drilling as well as minor earthquakes, Fridleifsson (2003) finds that their environmental impacts are drastically less severe than other forms of energy used for heating and cooling. In addition to being less detrimental the

environmental impacts associated with RTES are also more controllable than those of other systems. Rybach (2003) concludes that proper planning and engineering can assure that these negative impacts are minimized, and others including Stumpf et al (2018) and Fridleifsson (2003) agree with the conclusion that the environmental impacts of geothermal are minor, controllable, or negligible.

Market and Implementation Barriers

While deep geothermal is one of the most environmentally friendly methods of heating and cooling it has yet to become mainstream due to market domination by electricity and natural gas, high capital costs, and a lack of product commercialization. Natural gas and electricity account for nearly all of the "thermal energy" or energy used for heating and cooling in Oregon. The Oregon Department of Energy states that, "Electricity, natural gas, and petroleum make up more than 90% of Oregon's thermal energy use." According to the EIA's Use of Heating Oil (2016), states in the "West" region use less oil for heating than any other region in the country indicating its minimal use compared with natural gas and electricity. Breaking into an energy market so thoroughly dominated by two products has proven difficult for deep geothermal and other types of clean energy.

RTES faces two key implementation barriers. First, despite having a competitive LCOE, deep geothermal projects have high upfront costs. For example, In Lazard's (2018) LCOE report they assume capital costs for geothermal projects to be between $4,000 and $6,400 per kW for capital cost while capital costs for natural gas combined cycle projects range from $700 to $1,300 per kW for capital costs (Figure 46). The Energy Information Administration supports these assumptions. Their 2016 report lists 2013 overnight capital costs for geothermal ranging from $4,600 to $6,600 per kWh while the same costs for various types of natural gas systems range from $719 to $2,200. The Environmental Protection Agency (2016) also agrees, and in a web page dedicated to different types of geothermal energy states, "Although (deep) geothermal steam requires no fuel and lower operational costs, the initial capital costs, especially drilling test wells and production wells, can be financially challenging."

The second implementation barrier is that deep geothermal technology is not fully mature. Tools used to harness geothermal energy for heating are continuously evolving making it difficult to produce a modular system that can be easily adjusted to fit the needs of different building types. Lazard (2018), EIA (2016), and Ellabban et al. (2014) all agree that geothermal is still developing as a direct use and electricity generating energy technology with potential far greater than its current use suggests. This has created a situation where commercialization and modularization of deep geothermal has yet to occur; as of now, they cannot be mass produced. Each system must be customized meaning more time and upfront costs for contractors, planners, and business owners compared with more modular electric or natural gas heating and cooling systems. An additional factor that makes customization necessary is that deep geothermal efficiency varies by location; different geologic situations provide different environments for

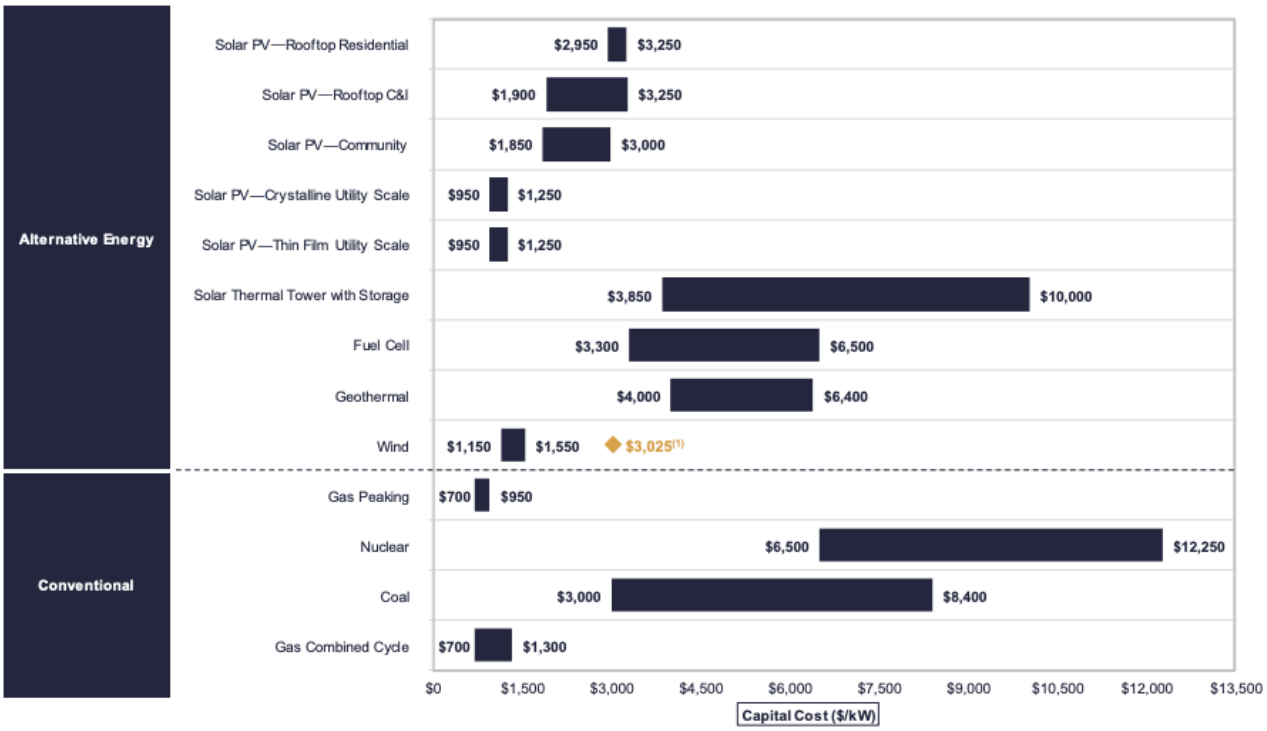

Figure 46. Capital Cost Comparison ($/kW) (Lazard, 2018)

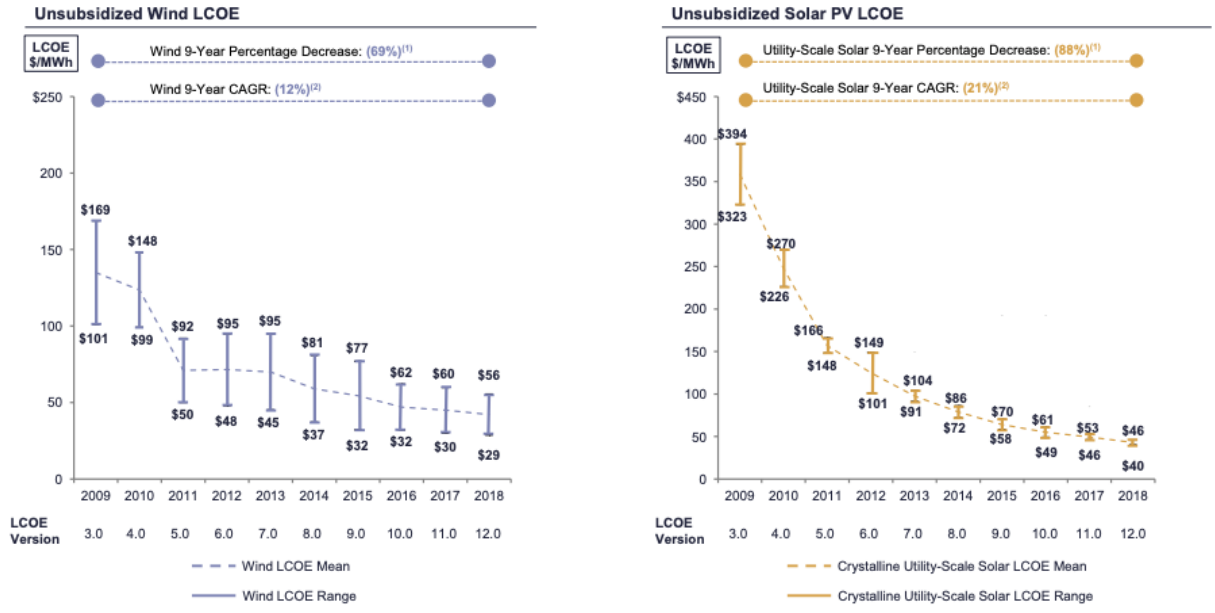

Figure 47. Levelized Cost of Energy Comparison - Historical Alternative Energy LCOE Declines, Unsubsidized Wind and Solar PV (Lazard, 2018)

geothermal use. Together, high capital costs and lack of commercial availability have stunted their commercial development and market growth. Two examples of emerging energy technologies facing similar barriers to geothermal are solar and wind. Both were seen as

alternative energy sources with high capital costs, but both have seen significant decreases in LCOE as technology has matured over the last decade.

According to Lazard (2018) the average LCOE for wind has fallen from $135 per kWh in 2009 to less than $43 per kWh in 2018 (Figure 47). Solar's LCOE has seen an even more drastic decrease. In 2009 the average cost per kWh was over $350, and in 2018 had fallen below $45 (Lazard, 2018). While the cost of deep geothermal projects vary with location, size, and well depth the cost of drilling per foot seems to falling. Lukawski et al. (2014) conclude in their paper that improved drilling technology has reduced the rate at which cost increases with depth. Schilling and Esmundo (2009) agree, and show that the cost of geothermal fell by more than half from 1980 to 2005. As the generation technologies mature, their relative prices have decreased historically.

Reliability and Resilience

The reliability of an energy system refers to how frequently it is able to produce the amount of energy it was constructed to. While specific definitions for reliability may vary, both the North American Electric Reliability Corporation reliability standards (2017) and the U.S. Department of Energy's (2017) definitions of energy reliability include measures of performance and risk management - do systems produce to the capacity they were built for on a consistent basis when conditions are typical? Common inputs that negatively affect the reliability of an energy system are fuel, energy leakages, and equipment failure. Deep geothermal is considered one of the most reliable types of energy generation due to its low cost and nearly unlimited fuel source.

First, geothermal harnesses energy from a reliable renewable source. The technology works because, at depth, the temperature of the Earth's crust fluctuates very little. Next, while both natural gas and electric systems could lose access to their fuel supply, geothermal systems pump water on or very near location, staying online in almost any situation. Geothermal systems are also known to have some of the most predictable costs. Fluctuation in natural gas and electricity prices could mean price uncertainty for systems that rely on those sources, but geothermal systems only face these constraints minimally due to its low electricity consumption. Yonk et al. (n.d.), Shortall et al. (2015), and the OEERE suggest geothermal systems as solutions that create more resilient energy systems citing their lack of susceptibility to climate change, constant interior temperatures of the earth, and the low cost of pumping water.

In the most recent quadrennial energy review (2015), multiple United States government entities defined energy resiliency as, "the ability to prepare for and adapt to changing conditions and withstand and recover rapidly from disruptions. Resilience includes the ability to withstand and recover from deliberate attacks, accidents, or naturally occurring threats or incidents." Geothermal is the one of the most resilient source of heating and cooling during and after a natural disaster. Gerner and Hansen provide evidence in their 2011 paper for the World Bank

that further development of geothermal systems in the Caribbean will be vital for increasing the regions resilience to climate change related disasters citing its ability to remain online after severe storms and in isolation. Others, NREL (2015) and Achieng Ogala (2013), discuss how its ability to provide baseload power and its low maintenance requirements make it a resilient resource when compared to others. This also applies to the risk of an earthquake in the Pacific Northwest with potential to disrupt traditional sources of heat (like natural gas), particularly crucial for critical infrastructure (like hospitals) directly after an event that could result in significant injuries and loss of life.

For the above mentioned reasons, deep geothermal energy in the RTES application can be considered as a high reliability and high resiliency option to providing heating and cooling building energy.

4.3 OHSU Case Study Economics

The Oregon Health Sciences University (OHSU) case study presented in this section applies our work in the market potential analysis and economic and operational feasibility analysis sections to the OHSU South Waterfront expansion (Figure 1). OHSU and its associated hospital are undergoing a period of growth, with six large new buildings and two major hospital expansions planned over the next two decades. First, we estimate a range of OHSU-specific levelized cost of energy (LCOE) given geologic, engineering and economic inputs and assumptions. Sensitivity analyses on a number of key assumptions, including discount rates, capital costs, water supply temperatures (and resulting energy output) and system lifetimes, are then conducted to ensure the robustness of the LCOE estimates. Then, we conduct a high-level extrapolation of the LCOE estimates to commercial buildings in Portland (using commercial buildings that are required to comply with Portland's Commercial Energy Reporting) to understand the general magnitude of RTES market potential. This case study will be a representative example of how urban critical infrastructure might be able to take advantage of RTES to substitute away from non-renewable, less resilient, or less reliable energy sources.

Levelized Cost of Energy (LCOE) Estimations

We utilize a form of the GEOPHIRES general LCOE Equation [15] for our estimation of an OHSU-specific LCOE, and assume that R_t (secondary revenue stream) is equal to zero in our specific case. The assumptions for each of the input variables into the LCOE equation are detailed in Table 22 along with the sources for each assumption, and the detailed capital cost assumptions are listed in Table 23, assuming a dual-well set up. One capital cost component that can vary significantly is the installation cost of the solar array, which will depend on the engineered heat desired. We include pricing that reflects a solar array that can accommodate model conditions at 75% and 125% of building heat load.

Table 23. OHSU Case Study Capital Cost Assumptions

Capital Cost Type	Cost	Quantity	Assumptions
Production Wells	$1,302,561	2	Two wells drilled < 400m (~1300 ft) depth to the target reservoir at the base of the CRBG
Pumps	$127,184	2	One pump will be installed in each well, enabling us to switch the direction of flow (cyclic operations).
Piping	$53,000	1,500 ft	Assume $30,000 trenching costs + $23,000 (25.4 cm diameter insulated piping at $15.33 / ft for 1,500 ft).
Subtotal (RTES only)	**$1,482,745**		
Solar Array	$2,437,439	3,000 m^2	This is the size of a solar array that can provide 100% of heating demand for conventional new build (220 ksf). Ranges from $1,828,079 for 75% to $3,046,798 for 125%.
Total Capital Cost	**$3,920,184**		Ranges from $3,310,824 (75%) to $4,529,543 (125%)

The annual heating energy demand for the modeled new build (220 sqft) based on KCRB at OHSU is determined to be 1.88 GWh. At RTES water supply temperatures of 80 C and solar array built to 75% capacity, the RTES system can supply a portion of the heating energy demand. With a solar array that can meet 125% of heating demand, the assumed RTES system will be able to meet the full energy demand within a few years (once the reservoir heats up). There are variations in operating costs depending on the heat available, as water pumping quantities and flow rates vary, resulting in a range of pumping electricity costs. However, while these annual operating costs vary, they are relatively minor, and do not contribute significantly to the LCOE calculation (approximately 0.10% to 0.13% of capital costs).

In our estimate of a baseline LCOE for OHSU, we are including the costs of the solar array (engineered heat) in addition to the costs of RTES infrastructure and maintenance, so these should be considered estimates of RTES plus solar heating, as the costs and benefits of both are included. We also assume a two-year period of "priming", where the reservoir is heated without extraction to establish the thermal mass necessary for efficient RTES operations. In addition, the base case assumes a solar array that can provide 125% of building heat demand, which comes to **$34.08 / MMBtu ($116.28 / MWh)**.

OHSU Case Study Sensitivity Analysis

Next, we conduct sensitivity analyses and additionally vary a number of key assumptions, including discount rates, capital costs, and system lifetimes, to ensure the robustness of the LCOE estimates. Table 24 summarizes all of the sensitivity analyses that were conducted. Each of

the analysis results incorporates the same baseline assumptions (except where noted) and a RTES water supply temperature of 80 C that supplies the heating demand of the OHSU model.

Table 24. OHSU Case Study Sensitivity Analyses Summary.

Variable	Units	Assumption	Sensitivity Analysis
System Lifetime	Years	30	25 and 35 years
Nominal Discount Rate	%	3.00%	5.00% and 7.00%
Real Discount Rate	%	0.80%	2.80% and 4.80% These real discount rates result from the nominal discount rate sensitivity analysis (Real Discount Rate = Nominal Discount Rate – Expected Annual Inflation)
Base Energy Output	kWh per year	1,212,735 - 1,845,164	TES water supply temperature of 80 C, and "engineered" heat (solar) varying from 75% to 125% of building heat load
Nominal Operating Costs	$ / year	$34,764	Annual pumping electricity varies according to RTES water supply temperatures and flow rates. Assumes $0.10/kWh electricity cost
Nominal Capital Costs	$	$3,310,824 - $4,529,543	Varies based on solar capacity assumptions (75%-125% of heating). See Table 23 for capital cost assumptions

1. *Nominal Discount Rate*
   The nominal discount rate is adjusted from the baseline assumption of 3% to 5% and 7% for this sensitivity analysis. Because real discount rate is equal to the nominal discount rate minus the estimated annual inflation rate (assumed to be 2.20%), the resulting real discount rates are 2.80% and 4.80%. The estimated LCOE at all water supply temperatures do not vary greatly from the baseline scenario, approximately 0.47% to 1.27% and 0.79% to 2.11% less than the baseline scenario at 5% and 7% nominal discount rates, respectively. These results are consistent with our expectations as the bulk of the costs associated with the RTES system are capital costs at the start of the project, and least affected by discount rate assumptions.

2. *System Lifetime*
   The system lifetime is assumed to be 30 years in the baseline scenario. We additionally estimate the LCOE using 25 and 35 years in this portion of our sensitivity analysis. Compared to the basecase LCOE of $34.08 per MMBtu ($116.28 per MWh), the LCOE becomes **$39.25 and $30.41 per MMBtu** at system lifetimes of 25 and 35 years, respectively. This is equivalent to an increase of 15% at the upper range (25 years), and a decrease of 12% at the lower range (35 years).

3. *Nominal Capital Cost*
As noted previously, the capital cost component that can vary significantly based on the cost of solar installation (engineered heat). This is equivalent to $3.311 million (75%) and $4.530 million (125%) in total nominal capital costs. We find that the LCOE is equal to **$40.38 MMBtu ($137.77 MWh)** with a solar array providing 75% of building heat demand, compared to **$34.08 per MMBtu ($116.28 per MWh)** with a solar array providing 125% of heat demand. This suggests that a larger system is ~18.5% more economic.

4. *System Lifetime and Nominal Capital Cost*
The system lifetime and nominal capital cost sensitivity analysis results indicate that these are two of the largest determinants of the LCOE estimates, whereas nominal discount rates appear to have minimal effects. We then alter both the system lifetime and nominal capital assumptions together to gauge the widest range of potential outcomes. Table 25 summarizes the resulting LCOE estimates. Compared with the baseline LCOE estimate in bold, the 35 year system lifetime yields the lowest LCOE of **$30.41 per MMBtu**, or 89% of the basecase. On the other end of the spectrum, the 25 year system lifetime running at 75% of total energy demand yields the highest LCOE of **$46.17 per MMBtu**, or 135% of the basecase.

Table 25. OHSU Case Study LCOE Estimates with System Lifetime and Nominal Capital Sensitivity Analysis. Costs in per MMBtu (per MWh).

System Lifetime	**Nominal Capital Cost**	
	$3.311 million (**75%** Energy Supply via Solar)	$4.530 million (**125%** Energy Supply via Solar)
25 years	$46.17 ($157.54)	$39.25 ($133.94)
30 years	$40.38 ($137.77)	**$34.08 ($116.28)**
35 years	$36.27 ($123.76)	$30.41 ($103.77)

Portland RTES Market Potential Analysis

The previous analysis, combining the Portland Commercial Energy Reporting (CER) with EIA's Commercial Energy Building Consumption Survey (CBECS), allows us to roughly estimate the overall market potential for RTES technology. Table 26 summarizes the heating and cooling energy usage in Portland commercial buildings[1] by building type. While heating energy is dominated by natural gas in Portland, cooling is dominated by electricity as an energy source.

[1] Again, this is limited to commercial buildings subject to the Portland CER requirements as noted previously.

Table 26. Portland Commercial Building Heating and Cooling Energy Usage by Building Type.

Building Type	Building Space (sqft)	#	Heating and Cooling Energy Use (MWh)	Heating Energy		Cooling Energy
				Natural Gas	Electric	
College	12,602,725	41	218,060	61.53%	3.44%	35.03%
Grocery	3,109,924	41	37,638	69.51%	7.16%	23.33%
Hospital	4,530,421	5	118,955	53.84%	1.06%	45.10%
Hotel	7,257,720	57	37,624	27.70%	12.10%	60.20%
Office	26,929,766	253	269,951	41.95%	9.01%	49.04%
Retail	2,461,060	38	22,255	49.53%	10.77%	39.70%
Other	13,457,279	178	198,264	60.19%	8.39%	31.42%
Grand Total	70,348,895	613	902,747	52.99%	6.57%	40.43%

The base case LCOE for RTES geothermal system in the OHSU case study is equal to $116.28 per MWh. Natural gas rates (as of April, 2019) are $0.82281 per therm for residential and $0.77852 per therm for commercial customers, equivalent to $28.08 and $26.56 per MWh. Electricity rates (also as of April, 2019) in in the Portland region depend on the utility provider, ranging between $0.0685 per kWh for Portland General Electric residential customers to $0.1115 per kWh for residential customers served by Pacific Power. Commercial electricity rates are $0.07572 per kWh for Portland General Electric and $0.092 per kWh for Pacific Power. These electricity rates are equivalent to a range of $68.50 to $111.50 per MWh. While these rates are not the same as LCOE estimates, they provide useful proxies for us to understand the relative cost of these energy sources.

We use the commercial cost for natural gas ($26.56 per MWh) and electricity (average $84.86 per MWh) to roughly estimate that commercial buildings in the City of Portland spend approximately $12.97 million on natural gas and $35.17 million on electricity for heating, totaling $48.14 million annually. Suppose that it is geologically, technically and economically feasible to expand systems such as the OHSU case study RTES system to all commercial buildings in the City of Portland, this translates to approximately $62.53 million in overall cost, which is approximately 30% more than current spending on heating. It is likely that the cost of RTES will decrease in the future as the cost of solar continues to decrease (Lazard, 2018). The question for urban planners and government officials is whether this additional cost is worth the environmental, reliability and resiliency benefits.

4.4 Regulatory Considerations

The proposed RTES project at OHSU is within the Portland city limits. It is an urban area near downtown with significant commercial and retail development. The proposed project including infrastructure would be located on land owned by OHSU. However, it is possible that

some piping would need to be installed across public right-of-ways. Ensuring that project development would not adversely impact other activities in the area is a concern and potential challenge to feasibility. Therefore, we convened a regulatory meeting on March 6, 2018, with participation from relevant government agencies at both the city and state level to discuss potential environmental impacts on nature and existing development. We also discussed time and costs associated with permitting to integrate into our economic assessment. Organizations represented at the meeting included:

1. City of Portland Water Bureau
2. City of Portland Bureau of Environmental Services (BES)
3. City of Portland Office for Community Technology (OCT)
4. City of Portland Bureau of Transportation (PBOT)
5. City of Portland Bureau of Planning and Sustainability (BPS)
6. Oregon Department of Environmental Quality (DEQ)
7. Oregon Department of Energy (ODOE)
8. Oregon Water Resources Department (OWRD)
9. Oregon Department of Geology and Mineral Industries (DOGAMI)
10. Washington Department of Natural Resources (DNR)

Primary considerations that came out of this meeting can be summarized as follows with an overview of permitting considerations shown in Table 27.

1. The depth of wells will affect which regulations apply. If technology is to applied to whole region/city, we need to think about regulations both above and below 2,000 ft.
2. Many regulations do not apply to brackish waters.
3. There is federal support from the US DOE; Oregon has primacy here (groundwater rules 1988) and is more stringent than the EPA.
4. Local Wellhead Protection Areas established by municipal water suppliers may influence site selection.
5. Will need franchise agreement from City of Portland Office for Community Technology (CTO) and permits through PBOT if crossing public right-of-way.
6. Further agreements would need to be reached with City of Portland Water Bureau since there are currently no existing regulations for this type of system. However, they are open to working towards development if it can be shown that RTES is in the public interest.
7. Qualification as geothermal well dependent on temperature over 250 degrees or depth lower than 2000 ft; if deemed a geothermal well, it could have more regulations from DOGAMI.
8. Depth and temperature of well will also determine if need for non-consumptive water rights applies with OWRD.

Table 27. Notable Permitting & Monitoring Considerations

	Policy Concern	Agency	Time and/or Cost	Other Considerations	Link to Information
City of Portland	Permit for private property construction	Bureau of Development	Project specific Likely < $1,000	The Alternative Technology Advisory Committee can assist with building code navigation and/or appeal	https://www.portlandoregon.gov/bds/36664 https://www.portlandoregon.gov/bds/48661
	Right-of-way franchise agreement	Office for Community Technology	1-3 years, cost to be negotiated with city	Need to start process early, involve lawyers if crossing public land	https://www.portlandoregon.gov/revenue/58882
	Protection and risk-mitigation study	Water Bureau	Project specific Likely <$10,000	This is not a regulation *per se* but would be required	https://www.portlandoregon.gov/water/
State of Oregon	Possible geothermal well permitting and monitoring	DOGAMI	~$25,000	Dependent on temperature > 250 degrees F or depth > 2,000 ft	http://www.oregongeology.org/mlrr/geothermal.htm
	Possible Aquifer Storage Recovery (ASR) well permit	DEQ, OWRD	Project specific contact: Jen Woody, OWRD 503.986-0855; Jennifer.L.Woody@oregon.gov	5-year Limited License for Testing from OWRD, DEQ input on water quality, then can apply for a permit. Likely will not apply due to intent, but need legal review	https://www.oregon.gov/owrd/pages/mgmt_asr.aspx
	Possible Underground Injection Control (UIC) system permit	DEQ	$125	Need legal review	http://www.oregon.gov/deq/wq/wqpermits/Pages/UIC.aspx
	Possible consideration as Class 5 injection system	DEQ	Flexible	Need to further consult with DEQ and lawyers, special process for "experimental purposes"	http://www.oregon.gov/deq/wq/wqpermits/Pages/UIC-Permit-Template.aspx
	Low temperature geothermal project registration	OWRD	None, include form with water right permit application.	Dependent on temp < 250 degrees F and < 2,000 ft deep	http://www.oregon.gov/owrd/pages/gw/forms.aspx
State of Oregon	Industrial / commercial water-right	OWRD	Water right application fees	If < 250 degrees F and < 2,000 ft deep,	http://www.oregon.gov/owrd/pages/pubs/forms.

	permit		are based on permitted rate; $1,350 base fee plus $350 per cfs and a $520 recording fee. Processing time is 6-12 months.	administrative rules for OWRD permitting apply: OAR 690-230 and OAR 690-310. Consult with Darrick.E.Boschmann@oregon.gov (the low-temperature geothermal program lead).	aspx#water_right
	Energy generation facility guidelines	ODOE	ODOE siting requirements apply to energy generation projects, not energy storage.	No tax credits available	http://www.oregon.gov/energy/Pages/index.aspx

Outside of the OHSU location, it was determined that implementing RTES in an established well field may encounter significant hurdles. This may be relevant for development of RTES at the Portland International Airport (PDX), as it is located near a consumptive-use water well field in the Columbia Slough. Regardless of RTES location, we need to consider neighboring jurisdictions and their wells, because local municipalities use groundwater. Specifically, there are federally designated aquifers in Clark County Washington, Tigard, and Milwaukie. The goal is to use water from a reservoir that does not impact others. Using brackish water opposed to saline or fresh water will be helpful for public perception.

If system is installed on private property, then the permit review will go through the City of Portland's Bureau of Development Services (BDS). This is preferable as it would be lower cost and less time. If the system crosses the public right-of-way (pipes under road, between buildings, etc.) then we will need a franchise agreement with the City from the Office for Community Technology (OCT), Revenue Division. Note that the franchising process is slow (1-3 years), one needs to begin early, and have lawyers involved. Right-of-way use compensation to the City of Portland would be negotiated. On the other hand, the Water Bureau has no existing regulations for this type of system. Only written protections and risk mitigation studies would need to be conducted for approval. The Bureau of Environmental Services (BES) may be less concerned because environmental impacts are unlikely from relatively deep wells.

State regulatory agency jurisdiction depends largely on whether or not the system qualifies as a geothermal well which are regulated by DOGAMI. A well is defined as geothermal if temperatures are over 250 degrees F or depths are greater than 2,000 ft. For the OHSU location, this is not the case. However, for locations near the Portland International Airport, depths may exceed 2,000 ft. If triggered, this will most likely require geothermal permitting (pending Department of Justice consultation). Additionally, ongoing monitoring for the life of

the well would be mandated, specifically focused on the geochemistry of water produced, monitoring of surrounding water wells, seismology, and production casing for injection and production wells. Land-use approval would also be required.

If the well was determined to be a low temperature geothermal project (bottom hole temperature less than 250 deg F and well less than 2000 feet deep), it would require an industrial / commercial water right permit and a low-temperature geothermal well registration via the Oregon Water Resources Department (OWRD). They suggest highlighting the intention to reinject groundwater for a non-consumptive water right in the application which will lower costs and scrutiny.

From the Oregon DEQ's perspective, the system could be considered Aquifer Storage Recovery (ASR) wells. However ASR artificial recharge permitting is likely not appropriate for RTES due to intent. Alternatively, it could be considered an Underground Injection Control (UIC) system, and language in UIC rules may accommodate the system. If it is determined to qualify as a UIC system, we would only need to file a permit that costs $125 to file. Generally, the regulatory focus is on keeping groundwater drinkable. A standard MIT test will need to occur every 5 years as well as other monitoring including: temperature, production, system integrity, etc. Also, this project could potentially be considered a Class 5 injection system (fluid return system), used for experimental purposes.

Ultimately, it is likely that the well would be regulated by OWRD for low temperature, non-consumptive use. We should avoid installing infrastructure on public right-of-ways if possible as this is expensive and time-prohibitive. Lastly, drilling near the Columbia Slough (near the Portland International Airport) would need additional assurances that the shallower, usable aquifer would not be affected.

Market Transformation Summary

The overall objective of this report is to evaluate and document the market potential and economic feasibility for RTES technology implementation in Portland at a high level. We start with an overview of Portland's energy usage profile through the analysis of Portland's Commercial Energy Reporting (CER) survey, particularly focusing in on understanding how heating and cooling energy intensities may be different for buildings with different characteristics. We find that the majority of energy use variation to be determined by the building type, and the building types with high energy demand, namely hospitals, colleges, and grocery stores, appear to be good candidates for geothermal projects. Buildings or campuses over 500,000 square feet in size may also benefit from a more efficient energy system, especially considering the cost of improvements may be smaller relative to the value of the building(s) and economies of scale benefits. Furthermore, buildings with predominantly electric heating and cooling systems could see substantial improvements to efficiency and economic outcomes with a geothermal system.

Then, we consider the costs of existing energy options in comparison to RTES, and review the potential environmental benefits/impacts and relevant resiliency and reliability characteristics with an examination of the literature. The research indicates that environmental impacts from deep geothermal are significantly lower than natural gas and the average electricity generation mix. While deep geothermal projects have occasionally been associated with releasing small amounts of harmful gasses from drilling as well as minor earthquakes, researchers generally conclude that these impacts are drastically less severe and more controllable than other energy sources used for heating and cooling. Researchers also suggest that the lack of susceptibility to climate change, constant interior temperatures of the earth, the low cost of pumping water, and localized provision of energy as reasons why deep geothermal energy in the RTES application can be considered as a high reliability and high resiliency option to providing heating and cooling building energy. We identify the main market implementation barriers for geothermal technology as high fixed capital costs and lack of commercial availability, but also note that these barriers can be overcome as the technology matures and research or pilot projects similar to this one are conducted.

Finally, we apply the common metric for energy cost comparisons—levelized cost of energy (LCOE)—to assess the economic feasibility of a RTES system as part of an OHSU case study. In addition to estimating a range of OHSU-specific levelized cost of energy (LCOE) using geologic, engineering and economic inputs and assumptions, we conduct sensitivity analyses on a number of key assumptions, including discount rates, capital costs, water supply temperatures (and resulting energy output) and system lifetimes, to ensure the robustness of the LCOE estimates. We find that the OHSU case study LCOH to be equal to **$34.08 per MMBtu** (LCOE is $116.28 per MWh) in the baseline scenario, and ranges between **$30.41 and $46.17 per MMBtu** ($103.77 and $157.54 per MWh respectively) in the sensitivity analyses. The magnitude of LCOE fluctuations depend on the specific assumptions being varied, with the system lifetime and nominal capital cost assumptions contributing to the largest ranges of variations.

CONCLUSIONS

RTES is shown to be a viable option for heating conventional buildings at Oregon Health Sciences University (OHSU) along the South Waterfront expansion district, suggesting significant potential for large facilities (e.g., the Portland International Airport) or district heating across the Portland Basin. The simplifying assumptions of RTES are robust, and paired with other low-carbon sources of energy like solar, hold tremendous promise for many large cities in the USA which overly brackish reservoirs at depth. That said, this is a Phase 1 study, so significant uncertainty remains regarding the ability to efficiently inject and produce heated (or cooled) water seasonally. More work needs to be done to better understand heterogeneity in the subsurface and the economics of seasonal cooling, which may prove more beneficial than heating.

Key Take-aways:

1. We find that the most important factors that influence RTES efficacy are operational schedule, well spacing, the amount of summer heat stored (in our model, a function of solar array size), and longevity of the system.
2. Key risks in implementing RTES include reservoir heterogeneity (e.g. faults and fractures) and scaling (mineral precipitation) due to high temperatures involved (in this study, up to 80 C).
3. Preheating of the reservoir and higher injection temperatures shorten the period until thermal loads can be met, with heat recovery efficiency continuing to increase over time.
4. Use of the brackish waters of the CRBG for RTES represents a previously unidentified beneficial non-consumptive use of this resource, suggesting great potential for brackish reservoirs across the USA.
5. Our basecase levelized cost of heat (LCOH) estimate ($34.08 per MMBtu or $116.28 per MWh) suggests RTES is comparable to unsubsidized solar and nuclear, but more expensive than natural gas.
6. We suggest RTES holds additional benefits in energy resiliency, particularly for critical infrastructure in the event of a natural disaster, in addition to reducing our carbon footprint in heating and cooling of large infrastructure.
7. The Portland Basin has a large thermal energy storage capacity (reaching ~43,400 GWh) for both heating and cooling, suggesting tremendous potential to expand RTES throughout the Portland Metropolitan Area.
8. Cooling is also likely viable, but specially constructed building cooling systems may need to be utilized. Heating and cooling in the same vicinity will result in a reduction in thermal recovery efficiency. But if other renewables (e.g., wind, solar, ambient air/water temperature, etc.) are used as the reservoir heating/cooling sources, the tradeoff with thermal recovery can be evaluated.

Recommended future work for the Portland Basin:

1. Develop non-conventional building designs that use heating and cooling systems that are optimized for RTES (e.g., radiant floor cooling) to improve the economics (lower LCOH).
2. Cooling needs are more significant than heating in most cities across the USA (including Portland), with cooling demand anticipated to grow in the coming decades as buildings become better insulated and global climate continues to warm. This presents a great opportunity to evaluate the potential for RTES to provide building cooling for critical infrastructure.
3. Conduct a detailed investigation of RTES for cooling at the Portland International Airport (PDX), located in the center of the Portland Basin (contrasting OHSU which is on the basin edge), where seasonal cooling may be achieved through heat exchange with Columbia River water.
4. Develop a "risk-reward" map of the Portland Basin that integrates RTES heating and cooling resource potential with geologic risk and estimated capital costs.
5. Conduct hydrogeologic or geophysical tests that demonstrate the likelihood that sufficient connectivity exists under the South Waterfront expansion district to install a well doublet. Conduct tests that quantify the effect of heterogeneity, and run simulations that account for the actual heterogeneity of the system. This might include tracer tests to evaluate early breakthrough, and reservoir tests that identify lateral boundaries (e.g., faults).

SPECIAL TERMS AND CONDITIONS

- *Acknowledgment:* This material is based upon work supported by the U.S. Department of Energy's Office of Energy Efficiency and Renewable Energy (EERE) under the Geothermal Technologies Office Award Number DE-EE0008104.

REFERENCES

Abdelhamid, Mahmoud & Pilla, Srikanth & Singh, Rajendra & Haque, Imtiaz & Filipi, Zoran. (2016). A comprehensive optimized model for on-board solar photovoltaic system for plug-in electric vehicles: Energy and economic impacts. International Journal of Energy Research. 40. 10.1002/er.3534.

Achieng Ogala, P.F. (2013). The power to change: Creating lifeline and mitigation-adaptation opportunities through geothermal energy utilization. Faculty of Life and Environmental Sciences School of Engineering and Natural Sciences, University of Iceland. Retrieved from https://skemman.is/bitstream/1946/14022/5/Creating%20lifeline%20and%20mitigation-adaptation%20opportunities%20through%20geothermal%20energy%20utilisation-Ch.5.pdf.

American Physical Society. (2018). Energy Units. https://www.aps.org/policy/reports/popa-reports/energy/units.cfm.

Ames, L.L., and McGarrah, J.E. 1980. Hanford basalt flow mineralogy: Battelle Pacific Northwest Labs, Richland, Washington. Report PNL-2847, 469 p.

Aradóttir, E.S.P., Sonnenthal, E.L., and Jónsson, H. (2012). Development and evaluation of a thermodynamic dataset for phases of interest in CO_2 mineral sequestration in basaltic rocks. Chemical Geology. v. 304–305, p. 26–38. doi:10.1016/j.chemgeo.2012.01.031.

Auch, T. (2016). Oklahoma and Kansas Class II Injection Wells and Earthquakes, Fractracker. https://www.fractracker.org/2016/12/oklahoma-kansas-injection-wells/.

Baker, L.L. (2016). Nontronite Occurrences in Columbia River Basalts: Implications for Mars. Geological Society of America: Rocky Mountain Section, 68th Annual Meeting. https://gsa.confex.com/gsa/2016RM/webprogram/Paper275883.html.

Baker, L.L. and Neill, O.K. (2017). Geochemistry and mineralogy of a saprolite developed on Columbia River Basalt: Secondadry clay formation, element leaching, and mass balance during weathering. American Mineralogist. v. 102, p. 1632-1645.

Balsillie, J. H., & Benson, G. T. (1971). Evidence for the Portland Hills Fault. The Ore Bin, v. 33.

Banks, D. (2009). Thermogeological assessment of open-loop well-doublet schemes: A review and synthesis of analytical approaches. Hydrogeology Journal. 17, 1149-1155.

Banks, D. (2011). The application of analytical solutions to the thermal plume from a well doublet ground source heating or cooling scheme. Quarterly Journal of Engineering Geology and Hydrogeology. 44, 191-197.

Bar, K., Welsch, B., Schulte, D., Ruhaak, W., and Sass, I. (2017). Seasonal High Temperature Heat Storage with Middle Deep Borehole Heat Exchangers – a Coupled-Modeling Study. Proceedings: 42nd Workshop on Geothermal Reservoir Engineering, Stanford University, Stanford, CA.

Barbour, A.J., Norbeck, J.H. and Rubinstein, J.L. (2017). The effects of varying injection rates in Osage County, Oklahoma, on the 2016 M w 5.8 Pawnee earthquake. Seismological Research Letters. 88(4), pp.1040-1053.

Barker, J.A. (2012). Discussion on 'The application of analytical solutions to the thermal plume from a well doublet ground source heating/cooling scheme'. Quarterly Journal of Engineering Geology and Hydrogeology. Vol. 44, 191–197.

Bauer, W., Burns, W.J., and I.P. Madin. (2018). Open-File Report O-18-02, Earthquake Regional Impact Ananlysis for Clackamas, Multnomah, and Washington counties, Oregon. Oregon Department of Geology and Mineral Industries Open-File Report O-18-02, 90 p.

Beckers, K. F., Lukawski, M. Z., Reber, T. J., Anderson, B. J., Moore, M. C., & Tester, J. W. (2013). Introducing GEOPHIRES v1.0: Software Package for Estimating Levelized Cost of Electricity and/or Heat from Enhanced Geothermal Systems, 8. https://pangea.stanford.edu/ERE/pdf/IGAstandard/SGW/2013/Beckers.pdf.

Beckers, K. F., McCabe, K. (2018). Introducing GEOPHIRES v2.0: Updated Geothermal Techno-Economic Simulation Tool. https://pangea.stanford.edu/ERE/pdf/IGAstandard/SGW/2018/Beckers.pdf.

Benson, L.V., and Teague, L.S. (1982). Diagenesis of basalts from the Pasco Basin, Washington – I – Distribution and composition of secondary mineral phases. Journal of Sedimentary Petrology. 52:595-613.

Bethke, C. M. (2008). Geochemical and Biogeochemical Reaction Modeling. Cambridge, Cambridge University Press. 543 p.

Beeson, M.H., K.R. Fecht, S.P. Reidel, and T.L. Tolan. (1985). Regional correlations within the Frenchman Springs Member of the Columbia River Basalt Group: New insights into the middle Miocene tectonics of northwestern Oregon. Oregon Geology. 47 no. 8, 87-96.

Beeson, M.H., T.L. Tolan, and J.L. Anderson. (1989a). The Columbia River Basalt Group in western Oregon; geologic structures and other factors that controlled flow emplacement patterns. Reidel, SP and Hooper, PR, Volancism and Tectonism in the Columbia River Flood-Basalt Province. Spec Pap Geol Soc Am. 239, 223-246.

Beeson, M.H., Tolan, T.L., and Madin, I.P. (1989b). Geologic map of the Lake Oswego quadrangle, Clackamas, Multnomah, and Washington Counties, Oregon. State of Oregon Geological Map Series. GMS-59, 1 sheet, scale 1:24,000.

Beeson, M.H., T.L. Tolan, and I.P. Madin. (1991). Geologic map of the Portland quadrangle, Multnomah and Washington Counties, Oregon, and Clark County, Washington, State of Oregon. Department of Geology and Mineral Industries.

Benson, L. V, and Teague, L.S. (1982). Diagenesis of Basalts from the Pasco Basin, Washington I: Distribution and Composition of Secondary Mineral Phases. https://pubs.geoscienceworld.org/sepm/jsedres/article-pdf/52/2/595/2808695/595.pdf.

Bethke, C. M. (2008). Geochemical and Biogeochemical Reaction Modeling. Cambridge, Cambridge University Press. 543 p.

Bielo, D. (2008). Deep Geothermal: The Untapped Renewable Energy Source. https://e360.yale.edu/features/deep_geothermal_the_untapped_energy_source.

Blackwell, D. D., D. A. Hull, R. G. Bowen, and J. L. Steele. (1978). Heat flow of Oregon. Oregon Dept. of Geology and Mineral Industries. Special Paper 4, 42 p.

Blackwell, D.D. and J.L. Steele. (1987). Geothermal data from deep holes in the Oregon Cascade Range. Geothermal Res. Council Trans. v. 11, pp. 317-322.

Blackwell, D.D., J.L. Steel, M.K. Frohme, C.F. Murphey, G.R. Priest, and G.L. Black. (1990). Heat flow in the Oregon Cascade Range and its correlation with regional gravity, curie point depths, and geology. J. of Geophys. Res. 95, 19475-19493.

Blakely, R.J., Wells, R.E., Yelin, T.S., and Beeson, M.H. (1995). Tectonic setting of the Portland-Vancouver area, Oregon and Washington – constraints from low-altitude aeromagnetic data. Geological Society of America Bulletin. v.107, p.1051-1062.

Blakely, R.J., K. Cruikshank, K, A. Johnson, M. Beeson, K. Walsh, and R.E. Wells. (1997). A gravity study through the Tualatin Mountains, Oregon—Understanding crustal structure and earthquake hazards in the Portland urban area. Geological Society of America Abstracts with Programs. 29, no. 5, 5.

Blakely, R. J., R.E. Wells, T.L. Tolan, M. H. Beeson, A.M. Trehu, and L.M. Liberty. (2000). New aeromagnetic data reveal large strike-slip (?) faults in the northern Willamette Valley, Oregon. Geol. Soc. Am. Bull. 112, no. 8, 1225-1233. doi: https://doi.org/10.1130/0016.

Bloemendal, M., Olsthoorn, T., and Boons, F. (2014). How to achieve optimal and sustainable use of the subsurface for Aquifer Thermal Energy Storage. Energy Policy. 66, (2014), 104-114.

Bozkaya, B., Li, R., Labeodan, T., Kramer, R., and Zeiler, W. (2017). Development and evaluation of a building integrated aquifer thermal storage model. Applied Thermal Engineering. 126, 620-629.

Bridger, D.W., and Allen, D.M. (2005). Designing Aquifer Thermal Energy Storage Systems Building for the Future. A Supplement to ASHRAE Journal. S32-S38.

Burns, E.R, Snyder, D.T, Haynes, J.V., and Waibel, M.S. (2012). Groundwater status and trends for the Columbia Plateau Regional Aquifer System, Washington, Oregon, and Idaho. U.S. Geological Survey Scientific Investigations Report 2012–5261. 52 p. http://pubs.er.usgs.gov/publication/sir20125261.

Burns, E.R., Williams, C.F., Ingebritsen, S.E., Voss, C.I., Spane, F.A., and DeAngelo, J. (2015). Understanding heat and groundwater flow through continental flood basalt provinces: insights gained from alternative models of permeability/depth relationships for the Columbia Plateau, USA. Geofluids. v. 15, p. 120–138. doi:10.1111/gfl.12095.

Burns, E.R., Ingebritsen, S.E., Manga, M., and Williams, C.F. (2016a) Evaluating geothermal and hydrogeologic controls on regional groundwater temperature distribution. Water Resour. Res. 52, 1328–1344. doi:10.1002/2015WR018204.

Burns, E.R., Williams, C.F., Tolan, T., and Kaven, J.O. (2016b). Are the Columbia River Basalts, Columbia Plateau, Oregon and Washington, USA, a Viable Geothermal Target? A Preliminary Analysis. Proceedings: 41st Workshop on Geothermal Reservoir Engineering. Stanford University, Stanford, California, February 22-24, 2016.

Burns, E.R., Cladouhos, T.T., Williams, C.F. and Bershaw, J. (2018). Controls on Deep Direct-Use Thermal Energy Storage (DDU-TES) in the Portland Basin, Oregon, USA. GRC Transactions. Vol. 42.

Burns, E. R., Bershaw, J., Williams, C. F., Wells, R., Uddenberg, M., Scanlon, D., ... & Van Houten, B. (2020). Using saline or brackish aquifers as reservoirs for thermal energy storage, with example calculations for direct-use heating in the Portland Basin, Oregon, USA. Geothermics. 88, 101877.

Camp, V.E., Price, S.M., and Reidel, S.P. (1978). Descriptive summary of the Grande Ronde Basalt type section. Columbia River Basalt Group Rockwell International. https://www.osti.gov/servlets/purl/6162969.

Church, J., Ekechi, C., Hoss, A., & Larson, A. (2016). Tribal Water Rights: Exploring Dam Construction in Indian Country. Journal of Law and Medical Ethics, 43(1). https://www.ncbi.nlm.nih.gov/pmc/articles/PMC4699571/.

Cummings, M.L., Trone, P.M., and Pollock, J.M. (1989). Geochemistry of colloidal silica precipitates in altered Grande Ronde Basalt, northeastern Oregon, U.S.A. Chemical Geology. v. 75, p. 61–79. doi:10.1016/0009-2541(89)90021-1.

Dagan, G. (1984). Solute transport in heterogeneous porous formations. J. Fluid. Mech. 145, 151-177.

Darling, S. B., You, F., Veselka, T., & Velosa, A. (2011). Assumptions and the levelized cost of energy for photovoltaics. Energy & Environmental Science. 4(9), 3133-3139. https://doi.org/10.1039/c0ee00698j.

Deutsch, W.J., Jenne, E.A., and Krupka, K.M. (1982). Solubility equilibria in basalt aquifers: the Columbia PLateau, eastern Washington, U.S.A. Chemical Geology. v. 36, p. 15–34.

Dickinson, J.S., Buik, N., Matthews, M.C., and Snijders, A. (2009). Aquifer thermal energy storage: theoretical and operational analysis. Geotechnique. 59, 249-260.

Doughty, C., Hellstrom, G., and Tsang, C.F. (1982). A Dimensionless Parameter Approach to the Thermal Behavior of an Aquifer Thermal Energy Storage System. Water Resour. Res. 18, 571-587.

Dyer, B.; Schanz, U.; et al. (2008). Microseismic imaging of a geothermal reservoir stimulation. The Leading Edge. 27 (7) 856–869. doi:10.1190/1.2954024.

Eaton, L., J. Melady. (2007). City of Beaverton – Year 2006 ASR Pilot Test Results. GSI Water Solutions, Inc. http://apps.wrd.state.or.us/apps/planning/owsci/view_project_image.aspx?project_type=GW&related_document_id=35.

Ellaban, O., Abu-Rub, H., Blaabjerg, F. (2014). Renewable energy sources: Current status, future prospects and their enabling technology. Renewable and Sustainable Energy Reviews. 39, 748-764. https://www.researchgate.net/profile/...to.../Renewableenergyressources.pdf.

Ely, D.M., Burns, E.R., Morgan, D.S., and Vaccaro, J.J. (2014). Numerical simulation of groundwater flow in the Columbia Plateau Regional Aquifer System, Idaho, Oregon, and Washington. U.S. Geological Survey Scientific Investigations Report 2014–5127. 90 p. http://dx.doi.org/10.3133/sir20145127.

Erickson, W., Wolfe, M., Bay, K., Johnson, D., & Gehring, J. (2014). A comprehensive analysis of small-passerine fatalities from collision with turbines at wind energy facilities. PLoS One. 15(9). https://www.ncbi.nlm.nih.gov/pubmed/25222738.

Evarts, R.C., J.E. O'Connor, R.E. Wells, and I.P. Madin. (2009). The Portland Basin: A (big) river runs through it. GSA Today. 19 no. 9, 4-10.

Fleuchaus, P., Godschalk, B., Stober, I., and Blum, P. (2018). Worldwide application of aquifer thermal energy storage – A review. Renewable and Sustainable Energy Reviews. 861-876.

Fortis Construction. (2009). Oregon University System Fifth Amendment to CM/GC Contract, Contract #OUS00204.

Fridleifsson, I. (2003). Status of geothermal energy amongst the world's energy sources. Geothermics. 32(4). https://www.sciencedirect.com/science/article/pii/S0375650503000798.

fueleconomy.gov. (2018). Compare (vehicles) Side-By-Side. https://www.fueleconomy.gov/feg/Find.do?action=sbs&id=33504&id=33503&id=33324.

Ganguly, S., Kumar, M.S.M, Date, A., and Akbarzadeh, A. (2017). Numerical investigation of temperature distribution and thermal performance while charging-discharging thermal energy in aquifer. Applied Thermal Engineering. 115, 756–773.

Gannett, M.W. (1985). Ground water heat pump use in downtown Portland - resource considerations. Solar Energy Association of Oregon, SEOGRAM. v. 4, n. 2, p. 6-9.

Gannett, M., and Caldwell, R.. (1998). Geologic framework of the Willamette Lowland aquifer system, Oregon and Washington. U.S. Geological Survey.

Gelhar, L.W., and Axness, C.L. (1983). Three-Dimensional Stochastic Analysis of Macrodispersion in Aquifers. Water Resources Research. 19, 161-180.

Gelhar, L.W., Gutjahr, A.L., and Naff, R.L. (1979). Stochastic Analysis of Macrodispersion in a Stratified Aquifer. Water Resources Research. 15, 1387-1397.

Geomatrix Consultants, Inc. (1995). Seismic design mapping, State of Oregon. Technical report to Oregon Department of Transportation, Salem, Oregon, under Contract 11688. 5 pls., scale 1:1,250,000.

Gerner, F., and Hansen, M. (2011). Caribbean Regional Electricity Supply Options: Toward Greater Security, Renewables and Resilience. World Bank. https://openknowledge.worldbank.org/handle/10986/2738.

Gislason, S.R., and Oelkers, E.H. (2003). Mechanism, rates, and consequences of basaltic glass dissolution: II. An experimental study of the dissolution rates of basaltic glass as a function of pH and temperature. Geochimica et Cosmochimica Acta. v. 67, p. 3817–3832. doi:10.1016/S0016-7037(03)00176-5.

Goebel, T. H. W., Weingarten, M., Chen, X., Haffener, J., & Brodsky, E. E. (2017). The 2016 Mw5. 1 Fairview, Oklahoma earthquakes: Evidence for long-range poroelastic triggering at > 40 km from fluid disposal wells. Earth and Planetary Science Letters. 472, 50-61.

Gringarten, A.C., and Sauty, J.P. (1975). A Theoretical Study of Heat Extraction from Aquifers with Uniform Regional Flow. Journal of Geophysical Research. 80, 4956-4962.

Haluszczak, L., Rose, A., & Kump. (2013). Geochemical evaluation of flowback brine from Marcellus gas wells in Pennsylvania, USA. Applied Geochemistry, 28, 55-61. https://pennstate.pure.elsevier.com/en/publications/geochemical-evaluation-of-flowback-brine-from-marcellus-gas-wells.

Hanks, T.C., and W.H. Bakun. (2002). A bilinear source-scaling model for M-log A observations of continental earthquakes. Bull. Seismol. Soc. Am. 92 no. 5, 1841-1846.

Hart, D. H., & Newcomb, R. C. (1965). Geology and ground water of the Tualatin Valley, Oregon. No. 1697. USGPO.

Hearn, P.P., Steinkampf, W.C., Bortleson, G.C., and Drost, B.W. (1985). Geochemical Controls on Dissolved Sodium in Basalt Aquifers of the Columbia Plateau, Washington. https://pubs.usgs.gov/wri/1984/4304/report.pdf.

Hearn, P.P., Steinkampf, W.C., White, L.D., and Evans, J.R. (1990). Geochemistry of Rock-Water Reactions in Basalt Aquifers of the Columbia River Plateau. Proceedings of a U.S. Geological Survey workshop on environmental geochemistry. p. 63–68.

Hellevang, H., Pham, V.T.H., and Aagaard, P. (2013). Kinetic modelling of CO_2–water–rock interactions. International Journal of Greenhouse Gas Control. v. 15, p. 3–15. doi:10.1016/j.ijggc.2013.01.027.

Herrera, N.B., Burns, E.R., and Conlon, T.D. (2014). Simulation of groundwater flow and the interaction of groundwater and surface water in the Willamette Basin and Central Willamette subbasin, Oregon. U.S. Geological Survey Scientific Investigations Report 2014–5136. 152 p. http://dx.doi.org/10.3133/sir20145136.

Hincks, T., Aspinall, W., Cooke, R. and Gernon, T. (2018). Oklahoma's induced seismicity strongly linked to wastewater injection depth. Science. 359(6381), pp.1251-1255.

Hook, M., Tang, X., (2013). Depletion of fossil fuels and anthropogenic climate change--A review. Energy Policy. 52, 797-809. http://www.cup.edu.cn/peakoil/docs/20140408160524637170.pdf.

Horst, A. (2019). Seismic Source Characterization of faults in the Portland and Tualatin Basins and a Paleoseismic study of the Gales Creek fault, OR. Master's Thesis. Portland State University, Portland, Oregon.

Howarth, R. W., Ingraffea, A., & Engelder, T. (2011a). Natural gas: Should fracking stop? Nature. 477, 271–275. https://doi.org/10.1038/477271a.

Howarth, R. W., Santoro, R., & Ingraffea, A. (2011). Methane and the greenhouse-gas footprint of natural gas from shale formations: A letter. Climatic Change. 106(4), 679–690. https://doi.org/10.1007/s10584-011-0061-5.

Hoyt, T. (2018). Industrial Sales, Schlumberger Artificial Lift / REDA, 12131 Industry Street Garden Grove, CA 92841.

Jaramillo, P., Griffin, W., & Matthews, H. (2007). Comparative life-cycle air emissions of coal, domestic natural gas, LNG, and SNG for electricity generation. Environmental Science & Technology. 41(17), 6290-6296. https://www.ncbi.nlm.nih.gov/pubmed/17937317.

Jayne, R.S., and Pollyea, R.M. (2018). Permeability correlation structure of the Columbia River Plateau and implications for fluid system architecture in continental large igneous provinces. Geology. v. 46. doi:10.1130/G45001.1.

Johnson, J., Anderson, G., & Parkhurst, D. (2000). Database "thermo. com. V8. R6. 230" Rev. 1-11. Lawrence Livermore Natl. Lab., Livermore, California.

Kangas, M.T., and Lund, P.D. (1994). Modeling and simulation of aquifer storage energy systems. Solar Energy. 53, 237-247.

Keranen, K. M., Savage, H. M., Abers, G. A., & Cochran, E. S. (2013). Potentially induced earthquakes in Oklahoma, USA: Links between wastewater injection and the 2011 Mw 5.7 earthquake sequence. Geology. 41(6), 699-702.

Kim, J., Lee, Y., Yoon, W.S., Jeon, J.S., Koo, M.-H., and Keehm, Y. (2010). Numerical modeling of aquifer thermal energy storage system. Energy. 35, 4955-4965.

Lachenbruch, A.H., and Sass, J.H. (1977). Heat Flow in the United States and the Thermal Regime of the Crust. The Earth's Crust: Geophysical Monograph Series. 20, 626-675.

Lazard. (2018). Levelized Cost of Energy Analysis—Version 12.0. https://www.lazard.com/media/450784/lazards-levelized-cost-of-energy-version-120-vfinal.pdf.

Lee, K.S. (2010). A Review on Concepts, Applications, and Models of Aquifer Thermal Energy Storage Systems. Energies. 3, 1320-1334.

Li, Q., & Pizer, W. A. (2019). Discounting for Public Cost–Benefit Analysis. Working Paper 19-02. Resources for the Future. https://www.rff.org/documents/1976/WP-19-02-Li-Pizer-f.pdf.

Liberty, L.M., M.A. Hemphill-Haley, and I.P. Madin. (2003). The Portland Hills Fault: uncovering a hidden fault in Portland, Oregon using high-resolution geophysical methods. Tectonophysics. 368 no. 1-4, 89-103. https://doi.org/10.1016/S0040-1951(03)00152-5.

Liberty, L.M., A.M. Trehu, R.J. Blakely, and M.E. Dougherty. (1999). Integration of high-resolution seismic and aeromagnetic data for earthquake hazards evaluations—An example from the Willamette Valley, Oregon. Bull. Seismol. Soc. Am. 89, no. 6, 1473-1483.

Lukawski, M., Anderson, B., Agustine, C., Capuano Jr, L. E. (2014). Cost Analysis of Oil, Gas, and Geothermal Well Drilling. Journal of Petroleum Science and Engineering. (03)12. https://www.researchgate.net/publication/261373850_Cost_Analysis_of_Oil_Gas_and_Geothermal_Well_Drilling.

Lund, J. W. (2010). Direct Utilization of Geothermal Energy. Energies. 3(8), 1443–1471. https://doi.org/10.3390/en3081443.

Madin, I.P. (1990). Earthquake-hazard geology maps of the Portland metropolitan area, Oregon—Text and map explanation: State of Oregon. Department of Geology and Mineral Industries Open-File Report 0-90-2. 21 p., 8 pls., scale 1:24,000.

Madin, I.P., G.R. Priest, M.A. Mabey, S. Malone, T.S. Yelin, and D. Meier. (1993). March 25, 1993, Scotts Mills earthquake— Western Oregon's wake-up call. Oregon Geology. 55, no. 3, 51-57.

McCaffrey, R., R.W. King, S.J. Payne, and M. Lancaster. (2013). Active tectonics of northwestern US inferred from GPS-derived surface velocities. J Geophys Res B Solid Earth Planets. 118 no. 2, 709-723. doi:10.1029/2012JB009473.

McGarr, A., Bekins, B., Burkardt, N., Dewey, J., Earle, P., Ellsworth, W., Ge, S., Hickman, S., Holland, A., Majer, E. and Rubinstein, J. (2015). Coping with earthquakes induced by fluid injection. Science. 347(6224), pp.830-831.

McPhee, D.K., Langenheim, V.E., Wells, R.E., and Blakely, R.J. (2014). Tectonic evolution of the Tualatin basin, northwest Oregon, as revealed by inversion of gravity data. Geosphere. v.10, p.264-275.

Mercer, J.W., Faust, C.R., and Miller, W.J. (1982). Review of Simulation Techniques for Aquifer Thermal Energy Storage (ATES). Advances in Hydroscience. 13, 1-129.

Molson, J.W., Frind, E.O., and Palmer, C.D. (1992). Thermal Energy Storage in an Unconfined Aquifer 2. Model Development, Validation, and Application. Water Resources Research. 28, 2857-2867.

Molz, F.J., Melville, A.D., Parr, A.D., King, D.A., and Hopf, M.T. (1983). Aquifer Thermal Energy Storage: A Well Doublet Experiment at Increased Temperatures. Water Resources Research. 19, 149-160.

Molz, F.J., Parr, A.D., and Andersen, P.F. (1981). Thermal Energy Storage in a Confined Aquifer: Second Cycle. Water Resources Research. 17, 641-645.

Mundorff, M. J. (1964). Geology and ground-water conditions of Clark County Washington, with a description of a major alluvial aquifer along the Columbia River. (No. 1600). USGPO.

Mustafa Omer, A. (2008a). Ground-source heat pumps systems and applications. Renewable and Sustainable Energy Reviews. 12(2), 344–371. https://doi.org/10.1016/j.rser.2006.10.003.

National Energy Technology Laboratory. (2010). Cost and performance baseline for fossil energy plants. Volume 1: Bituminous coal and natural gas electricity. https://www.netl.doe.gov/energy-analyses/pubs/BitBase_FinRep_Rev2.pdf.

National Research Council. (2013). Induced Seismic Potential in Energy Technologies. Washington, DC: The National Academic Press. https://doi.org/10.17226/13355.

Northwest Power and Conservation Council. (2018). Avoided Carbon Dioxide Production Rates in the Northwest Power System. https://www.nwcouncil.org/sites/default/files/2018-1.pdf.

Northwest Power and Conservation Council. (2018). Dams: impacts on salmon and steelhead. Retrieved from https://www.nwcouncil.org/reports/columbia-river-history/DamsImpacts.

NREL. (2018). Levelized Cost of Energy Calculator, Energy Analysis. https://www.nrel.gov/analysis/tech-lcoe.html.

Office of Energy Efficiency and Renewable Energy. (2018). Low Temperature Deep Direct-Use Program Draft White Paper. https://www.energy.gov/eere/geothermal/low-temperature-deep-direct-use-program-draft-white-paper.

Oklahoma Corporation Commission directive. (2015). http://occeweb.com/News/DIRECTIVE-2.pdf.

Oregon Department of Energy. (2018). Power Production Oregon April 2018 Revisions. https://www.oregon.gov/energy/energy-oregon/Pages/Electricity-Mix-in-Oregon.aspx.

PAE. (2017). Energy Analysis Report – Energy Trust Project #2014347.

Paksoy, Halime Ö., ed. (2007). Thermal energy storage for sustainable energy consumption: fundamentals, case studies and design. NATO science series. Series II, Mathematics, physics, and chemistry.

Palandri, J.L., and Kharaka, Y.K. (2004). A Compilation of Rate Parameters of Water-Mineral Interaction Kinetics for Application to Geochemical Modeling. https://pubs.usgs.gov/of/2004/1068/pdf/OFR_2004_1068.pdf.

Parkhurst, D. L. (1995). User's guide to PHREEQC-A computer program for speciation, reaction-path, advective-transport, and inverse geochemical calculations. Water-resources investigations report. 95(4227), 1-143.

Personius, S.F. (2002a). Fault number 715, Beaverton fault zone, in Quaternary fault and fold database of the United States. U.S. Geological Survey website. https://earthquakes.usgs.gov/hazards/qfaults.

Personius, S.F. (2002b). Fault number 874, Bolton fault, in Quaternary fault and fold database of the United States. U.S. Geological Survey website. https://earthquakes.usgs.gov/hazards/qfaults.

Personius, S.F. (2002c). Fault number 716, Canby-Molalla fault, in Quaternary fault and fold database of the United States. U.S. Geological Survey website. https://earthquakes.usgs.gov/hazards/qfaults.

Personius, S.F. (2002d). Fault number 876, East Bank fault, in Quaternary fault and fold database of the United States. U.S. Geological Survey website. https://earthquakes.usgs.gov/hazards/qfaults.

Personius, S.F. (2002e). Fault number 714, Helvetia fault, in Quaternary fault and fold database of the United States. U.S. Geological Survey website. https://earthquakes.usgs.gov/hazards/qfaults.

Personius, S.F. (2002f). Fault number 880, Lacamas Lake fault, in Quaternary fault and fold database of the United States. U.S. Geological Survey website. https://earthquakes.usgs.gov/hazards/qfaults.

Personius, S.F. (2002g). Fault number 717, Newberg fault, in Quaternary fault and fold database of the United States. U.S. Geological Survey website. https://earthquakes.usgs.gov/hazards/qfaults.

Personius, S.F. (2002h). Fault number 875, Oatfield fault, in Quaternary fault and fold database of the United States. U.S. Geological Survey website. https://earthquakes.usgs.gov/hazards/qfaults.

Personius, S.F., and Haller, K.M. (2017a). Fault number 718, Gales Creek fault zone, in Quaternary fault and fold database of the United States. U.S. Geological Survey website. https://earthquakes.usgs.gov/hazards/qfaults.

Personius, S.F., and Haller, K.M. (2017b). Fault number 877, Portland Hills fault, in Quaternary fault and fold database of the United States. U.S. Geological Survey website. https://earthquakes.usgs.gov/hazards/qfaults.

Personius, S.F., Lidke, D.J., and Haller, K.M. (2014). Fault number 873, Mount Angel fault, in Quaternary fault and fold database of the United States. U.S. Geological Survey website. https://earthquakes.usgs.gov/hazards/qfaults.

Popowski, T.A. (1996). Geology, structure, and tectonic history of the Tualatin Basin, northwestern Oregon. M.S. Thesis. Oregon State University. 126 pp.

Possemeiers, M., Huysmans, M., and Batelaan, O. (2014). Influence of Aquifer Thermal Energy Storage on groundwater quality: A review illustrated by seven case studies from Belgium. Journal of Hydrology. Regional Studies. 2, 20-34.

Pratt, T.L., J. Odum, W. Stephenson, R. Williams, S. Dadisman, M. Holmes, and B. Haug. (2001). Late Pleistocene and Holocene tectonics of the Portland Basin, Oregon and Washington, from high-resolution seismic profiling. Bull. Seismol. Soc. Am. 91 no. 4, 637-650.

Reidel, S.P., Tolan, T.L., Hooper, P.R., Beeson, M.H., Fecht, K.R., Bentley, R.D., and Anderson, J.L. (1989). The Grande Ronde Basalt, Columbia River Basalt Group; Stratigraphic descriptions and correlations in Washington, Oregon, and Idaho. Geological Society of America Special Paper. v. 497, p. 21–54. doi:10.1130/SPE239-p21.

Rockenbaugh, C., Dean, J., Lovullo, D., Lisell, L., Barker, G., Hanckock, E., Norton, P. (2016). High Performance Flat Plate Solar Thermal Collector Evaluation. National Renewable Energy Lab. (NREL), Golden, CO (United States).

Rubinstein, J.L. and Mahani, A.B. (2015). Myths and facts on wastewater injection, hydraulic fracturing, enhanced oil recovery, and induced seismicity. Seismological Research Letters. 86(4), pp.1060-1067.

Ryan, G. P. (1981). Equipment Used in Direct Heat Projects. Geothermal Resources Council Transactions, Vol. 5, Davis, CA. pp. 483-486.

Rybach, L. (2003). Geothermal energy: sustainability and the environment. Geothermics. 32(4–6), 463–470. https://doi.org/10.1016/S0375-6505(03)00057-9.

Sauty, J.P., Gringarten, A.C., Menjoz, A., and Landel, P.A. (1982). Sensible Energy Storage in Aquifers 1. Theoretical Study. Water Resources Research. 18, (1982), 245-252.

Schilling, M., & Esmundo, M. (2009). Technology S-curves in renewable energy alternatives: Analysis and implications for industry and government. Energy Policy. 37(5), 1767-1781. https://www.sciencedirect.com/science/article/pii/S0301421509000111.

Schlicker, H.G., and C.T. Finlayson. (1979). Geology and geologic hazards of northwestern Clackamas County, Oregon. State of Oregon, Department of Geology and Mineral Industries Bulletin. 99, 79 p., 10 pls., scale 1:24,000.

Schlicker, H.G., R.J. Deacon, and N.H. Twelker. (1964). Earthquake geology of the Portland area, Oregon. The Ore Bin. 26, no. 12, 209-230.

Schulze-Makuch, D. (2005). Longitudinal Dispersivity Data and Implications for Scaling Behavior. Ground Water. v. 43, p. 443–456. doi:10.1111/j.1745-6584.2006.00166.x.

Schwartz, F. W., & Zhang, H. (2003). Fundamentals of Groundwater. John Wiley & Sons. New York. 583 p.

Shortall, R., Davidsdottir, B., & Axelsson, G. (2015). Geothermal energy for sustainable development: A review of sustainability impacts and assessment frameworks. Renewable and Sustainable Energy Reviews. 44, 391–406. https://doi.org/10.1016/j.rser.2014.12.020.

Snyder, D.T. (2008). Estimated depth to ground water and configuration of the water table in the Portland, Oregon area. U.S. Geological Survey Scientific Investigations Report 2008–5059. 40 p. http://pubs.usgs.gov/ sir/2008/5059/.

Sommer, W.T., Doornenbal, P.F., Drijver, B.C., van Gaans, P.F.M., Leusbrock, I., Grotenhuis, J.T.C., and Rijnaarts, H.H.M. (2014). Thermal performance of and heat transport in aquifer thermal energy storage. Hydrogeology Journal. 22, 263-279.

Stanton, J.S., Anning, D.W., Brown, C.J., Moore, R.B., McGuire, V.L., Qi, S.L., Harris, A.C., Dennehy, K.F., McMahon, P.B., Degnan, J.R., and Böhlke, J.K. (2017). Brackish groundwater in the United States. U.S. Geological Survey Professional Paper 1833. 185 p., https://doi.org/10.3133/pp1833.

State of Oregon (2018). Energy in Oregon - How Oregon Uses Energy. https://www.oregon.gov/energy/energy-oregon/Pages/How-Oregon-Uses-Energy.aspx.

Stats.oecd.org. (2001). Primary Energy Consumption. https://stats.oecd.org/glossary/detail.asp?ID=2112.

Steele, J. L., D. D. Blackwell, and J. H. Robison. (1982). Heat flow in the vicinity of the Mount Hood volcano, Oregon. Geology and Geothermal Resources of the Mount Hood area, Oregon, eds. G. R. Priest, and B. F. Vogt, Ore. Dept. Geol. Min. Ind. Sp. Pap. 31-42.

Stillings, L.L., Drever, J.I., Brantley, S.L., Sun, Y., and Oxburgh, R. (1996). Rates of feldspar dissolution at pH 3-7 with 0-8 m M oxalic acid. Chemical Geology. v 132, p. 79-89.

Strawn, D.G., Baker, L.L., Sprenke, K.F., and Rember, W.C. (2012). Celadonite in continental flood basalts of the Columbia River Basalt Group. American Mineralogist. v. 97, p. 1284–1290. doi:10.2138/am.2012.4129.

Stumpf, A., Damico, J., Okwen, R., Stark, T., Elrick, S., Nelson, W., & Lin, Y. (2018). Feasibility of a Deep Direct-Use Geothermal System at the University of Illinois Urbana-Champaign. GRC Transactions. 42. https://www.osti.gov/biblio/1462352.

Tangshan Xingbang Pipeline Engineering Equipment Co. (2018). bella@tsxb-pipeline.com.cn.

Tester, J., Livesay, B., Anderson, B., Moore, M., Batchelor., Nichols, K., . . . & Murphy, E., (2006). The Future of Geothermal Energy: Impact of Enhanced Geothermal Systems (EGS) on the United States in the 21st Century. Idaho National Laboratory. https://energy.mit.edu/wp-content/uploads/2006/11/MITEI-The-Future-of-Geothermal-Energy.pdf.

Tenma, N., Yasukawa, K., and Zyvoloski, G. (2003). Model study of the the thermal storage system by FEHM code. Geothermics. 32, 603-607.

The Oklahoma Register. (2018). Title 165. Corporate Commission Chapter 5. Rules of Practice, Vol. 35, No. 24, p. 705-2322.

The Royal Society. (2012). Shale gas extraction in the UK: a review of hydraulic fracturing. https://royalsociety.org/~/media/policy/projects/shale-gas-extraction/2012-06-28-shale-gas.pdf.

The Sydney Morning Herald. (2007). Hot firm rock looks at Earthquake risk. https://www.smh.com.au/business/hot-rock-firm-looks-at-earthquake-risk-20070102-gdp5ro.html.

Thomas, G.C., R.S. Crosson, D.L. Carver, T.S. and Yelin. (1996). The 25 March 1993 Scotts Mills, Oregon, earthquake and aftershock sequence: Spatial distribution, focal mechanisms, and the Mount Angel fault. Bull. Seismol. Soc. Am. 86, no. 4, 925–935.

Tillman, J.E., (1980). Eastern geothermal resources: should we pursue them? Science. 210(4470), 595-600. https://www.ncbi.nlm.nih.gov/pubmed/17815134.

Toda, Shinji, Stein, R.S., Sevilgen, Volkan, and Lin, Jian. (2011). Coulomb 3.3 Graphic-rich deformation and stress-change software for earthquake, tectonic, and volcano research and teaching—user guide. U.S. Geological Survey Open-File Report 2011-1060. 63 p. http://pubs.usgs.gov/of/2011/1060/.

Tolan, T.L., Lindsey, K., and Porcello, J. (2009). A Summary of Columbia River Basalt Group Physical Geology and its Influence on the Hydrogeology of the Columbia River Basalt Aquifer System. Columbia Basin Ground Water Management Area of Adams, Franklin, Grant, and Lincoln Counties.

Tsang, C.F., Buscheck, T. Mangold, D., and Lippmann, M. (1979). Mathematical modeling of thermal energy storage in aquifers. Proceedings of Thermal Energy Storage in Aquifers Workshop, May 10-12, 1978, Lawrence Berkeley Laboratory, Berkeley, CA. 37-45.

Tsang, C.F., and Hopkins, D.L. (1982). Aquifer Thermal Energy Storage: A Survey. Geological Society of America Special Paper 189. 427-441.

University of Southampton. (2018). Oklahoma's Earthquakes Strongly linked to wastewater injection depth.

University of Washington. (1963). Pacific Northwest Seismic Network. International Federation of Digital Seismograph Networks. Dataset/Seismic Network. 10.7914/SN/UW

Unruh, J.R., Wong, I.G., Bott, J.D.J., Silva, W.J., and Lettis, W.R. (1994). Seismotectonic evaluation, Scoggins Dam, Tualatin Project, northwestern Oregon. Final Report prepared for U.S. Department of the Interior, Bureau of Reclamation. 206 p., 4 pls., scale 1:500,000.

U.S. Department of Energy. (2018). Levelized Cost of Energy (LCOE). https://www.energy.gov/sites/prod/files/2015/08/f25/LCOE.pdf.

U.S. Energy Information Administration. (2016). Capital Cost Estimates for Utility Scale Electricity Generating Plants. https://www.eia.gov/analysis/studies/powerplants/capitalcost/pdf/capcost_assumption.pdf.

U.S. Energy Information Administration. (2017). Use of Heating Oil - Energy Explained, Your Guide To Understanding Energy. https://www.eia.gov/energyexplained/index.php?page=heating_oil_use.

U.S. Energy Information Administration. (2019). Levelized Cost and Levelized Avoided Cost of New Generation Resources in the Annual Energy Outlook 2019. https://www.eia.gov/outlooks/aeo/pdf/electricity_generation.pdf.

U.S. Energy Information Administration. (2018). Natural Gas and the Environment - Energy Explained, Your Guide To Understanding Energy. https://www.eia.gov/energyexplained/?page=natural_gas_environment.

U.S. Environmental Protection Agency. (2014). Geothermal Heating and Cooling Technologies [Overviews and Factsheets]. https://www.epa.gov/rhc/geothermal-heating-and-cooling-technologies.

U.S. Geological Survey (2006). Quaternary fault and fold database for the United States. http//earthquake.usgs.gov/hazards/qfaults/.

U.S. Office of Energy Efficiency & Renewable Energy. (2016). Heat from Beneath the Ground. Working to Advance Deep Direct-Use Geothermal. https://www.energy.gov/eere/articles/heat-beneath-ground-working-advance-deep-direct-use-geothermal.

Van Pham, T.H., Aagaard, P., and Hellevang, H. (2012). On the potential for CO_2 mineral storage in continental flood basalts - PHREEQC batch- and 1D diffusion-reaction simulations. Geochemical transactions. v. 13, p. 5. doi:10.1186/1467-4866-13-5.

Vlassopoulos, D., Goin, J., Zeliff, M., Porcello, J., Tolan, T., and Lindsey, K. (2009). Groundwater Geochemistry of the Columbia River Basalt Group Aquifer System: Columbia Basin Ground Water Management Area of Adams , Franklin , Grant , and Lincoln Counties, WA.

Voss C.I., and Provost A.M. (2002). SUTRA, A model for saturated-unsaturated variable-density ground-water flow with solute or energy transport. U.S. Geological Survey Water-Resources Investigations Report 02-4231. 291 pp.

Waitt, R.B. (1985). Case for Periodic, Colossal Jökulhlaups from Pleistocene Glacial Lake Missoula. Geological Society of America. 96, 1271-1286.

Wang, Z., and I.P. Madin. (2001). Mount Angel fault characteristics using SH-wave refraction and reflection methods. Technical report to United States Geologic Survey (NEHRP).

Ward, J.D., Simmons, C.T., and Dillon, P.J. (2007). A theoretical analysis of mixed convection in aquifer storage and recovery: How important are density effects? Journal of Hydrology. 343, 169-186.

Washington Department of Transporation (WADOT). (2015). Final Report: Airport Investment Solutions.

Wells, D. L., & Coppersmith, K. J. (1994). New empirical relationships among magnitude, rupture length, rupture width, rupture area, and surface displacement. Bulletin of the seismological Society of America. 84(4), 974-1002.

Wells, R.E., Weaver, C.S., and Blakely, R.J. (1998). Fore-arc Migration in Cascadia and its Neotectonic Significance. Geology. 26, 759-762.

Wells, R. E., R.J. Blakely, D.K. McPhee, and V.E. Langenheim. (2009). The Gales Creek fault accommodates large dextral offset in the Oregon forearc. Geological Society of America Abstracts with Programs. 41, no. 7, 702.

Wells, R., Bukry, D., Friedman, R., Pyle, D., Duncan, R., Haeussler, P., & Wooden, J. (2014). Geologic history of Siletzia, a large igneous province in the Oregon and Washington Coast Range: Correlation to the geomagnetic polarity time scale and implications for a long-lived Yellowstone hotspot. Geosphere. 10(4), 692-719.

Wells, R.E., R. Haugerud, R.C. Evarts, A. Niem, W.A. Niem, L. Ma, J.E. O'Connor, and I.P. Madin. (2017). Geologic map of the greater Portland metropolitan area, Oregon and Washington. Geological Society of America Abstracts with Programs. 49, no. 6. doi: 10.1130/abs/2017AM-299799.

Wells, R.E., Haugerud, R., Niem, A., Niem, W., Ma, L., Madin, I., and Evarts, R. (2018). New Geologic Mapping of the Northwestern Willamette Valley, Oregon, and its American

Viticultural Areas (AVAs) – A Foundation for Understanding Their Terroir. U.S. Geological Survey Open-File Report 2018-1044.

Wells, Ray E., Haugerud, R.A., Niem, A.R., Niem, W.A., Ma, Lina, Evarts, R.C., O'Connor, J.E., Madin, I.P., Sherrod, D.R., Beeson, M.H., Tolan, T.L., Wheeler, K.L., Hanson, W.B., and Sawlan, M.G. (2019). Geologic map of the greater Portland metropolitan area and surrounding region, Oregon and Washington. U.S. Geological Survey Scientific Investigations Map 3443, scale 1:63,360, with 127 p.

Welsch, B., Ruhaak, W., Schulte, D.O., Bar, K., and Sass, I. (2016). Characteristics of medium deep borehole thermal energy storage. International Journal of Energy Research. 40, 1855-1868.

Werner, K.S. (1990). I. Direction of maximum horizontal compression in western Oregon determined by borehole breakouts II. Structure and tectonics of the northern Willamette Valley, Oregon. M.S. Thesis. Oregon State University. 159 pp.

Williams, C.F., and DeAngelo, J. (2008). Mapping Geothermal Potential in the Western United States. Transactions of the Geothermal Resources Council. 32.

Wong, I.G. (1997). The Historical Earthquake Record in the Pacific Northwest: Applications and Implications to Seismic Hazard Assessment. Converging in Cascadia, Symposium Proceedings: Association of Engineering Geologists Special Publication. 10, 19-36.

Wong, I., Silva, W., Bott, J., Wright, D., Thomas, P., Gregor, N., Li, S., Maybe, M., Sojourner, A., and Y. Wang. (2000). Earthquake Scenario and Probabilistic Ground Shaking Maps for the Portland, Oregon Metropolitan Area, Portland Hills fault M 6.8 Earthquake Peak Horizontal Acceleration (g) at the Ground Surface. Oregon Department of Geology and Mineral Industries Open-File Report IMS-15.

Wong, I.G., M.A. Hemphill-Haley, L.M. Liberty, and I.P. Madin. (2001). The Portland Hills fault: an earthquake generator or just another old fault. Oregon Geology. 63 no. 2, 39-50.

Yeats, R.S., E.P. Graven, K.S. Werner, C. Goldfinger, and T.A. Popowski. (1996). Tectonics of the Willamette Valley, Oregon. U.S. Geological Survey Professional Paper 1560. 1, 183-222.

Yeck, W. L., Weingarten, M., Benz, H. M., McNamara, D. E., Bergman, E. A., Herrmann, R. B., ... & Earle, P. S. (2016). Far-field pressurization likely caused one of the largest injection induced earthquakes by reactivating a large preexisting basement fault structure. Geophysical Research Letters. 43(19), 10-198.

Yelin, T. S., and H.J. Patton. (1991). Seismotectonics of the Portland, Oregon, region. Bull. Seismol. Soc. Am. 81 no. 1, 109-130.

Yelin, T. S. (1992). An earthquake swarm in the north Portland (Oregon) Hills: more speculations on the seismotectonics of the Portland Basin. Geological Society of America Abstracts with Programs. 24, no. 5, 92.

Yonk, R., Simmons, R., & Lofthouse, J. (2018). Reliability of Renewable Energy: Geothermal. Institute of Political Economy at Utah State University. https://www.usu.edu/ipe/wp-content/uploads/2015/11/Reliability-Geothermal-Full-Report.pdf.

Zakharova, N. V., Goldberg, D. S., Sullivan, E. C., Herron, M. M., and Grau, J. A. (2012). Petrophysical and geochemical properties of Columbia River flood basalt: Implications for carbon sequestration. Geochemistry, Geophysics, Geosystems. v. 2, p. 1-22.

APPENDICES

Appendix A1. Fault Characteristics for individual faults in the Seismic Source Characterization

Beaverton Fault			
	Data	**Type of Data**	**References**
Location	Fault extends at least 7 km north of the Farmington Hills	Well water logs correlating with a magnetic boundary	Popowski, 1996
	Fault continues >3 km east of Cooper Mountain, with down to the north	Water well data	Madin, 1990
Length	15 km	QFFD	Personius, 2002a
Strike	E-W	Aeromagnetics	Blakely et al., 2000
	N86°E	QFFD	Personius, 2002a
Dip	North-verging	Inversion of gravity data	McPhee et al., 2014
	South	Based on sense of movement	Wells, personal comm., 2018
	70° S	Focal Mechanisms from microseismicity	University of Washington, 1963
	Down to the north	Water wells	Madin, 1990
Sense of Movement	Thrust/reverse, responding to north-south maximum horizontal compressive stress of the region	Inversion of gravity data	McPhee et al., 2014
	The Beaverton fault and other contractional structures in the region such as the Cooper Mountain anticline and Parrett Mountain uplift are interpreted to be a left compressional step between the right-lateral Canby-Molalla fault and the Gales Creek fault zone.	Aeromagnetic data	Blakely et al., 2000
Slip Rate	<0.2 mm/yr	QFFD	Personius, 2002a
Displacement	Top of CRBG offset	Water well logs	Madin (1990)
	CRBG offset ~350 m down to the north	Seismic reflection data	Popowski, 1996
	Fault offsets Eocene basement >1km	Inversion of gravity data	McPhee et al., 2014
Age	Late Miocene to Pleistocene. Water well goes into 292 m of Grande Ronde basalt, indicative of a topographic low in early to middle Miocene.	Cooper Mountain well	Popowski, 1996
	Fault growth likely occurred during deposition of lower Miocene to Pliocene sediments, suggested by the lower portion of sedimentary sequence being thickened closest to the fault.	Seismic reflection data	Popowski, 1996

Other	Beaverton fault offsets Eocene Basement, displacing it >1km down to the north; and also displaces the overlying CRBG by ~200 m.	3D gravity inversion of the Tualatin Basin	McPhee et al., 2014

Bolton Fault			
	Data	**Type of Data**	**References**
Location	Exposed south of Lake Oswego	Low-altitude aeromagnetic data	Blakely et al., 1995
Length	9km	Earthquake scenario and probabilistic ground shaking maps	Wong et al., 2000
Strike	NW	Aeromagnetic data	Blakely et al., 1995
	N53°W	QFFD	Personius, 2002b
Dip	70° N	Earthquake scenario and probabilistic ground shaking maps	Wong et al., 2000
	SW	Geologic mapping	Beeson et al., 1989b
	West	Based on sense of motion	Wells, personal comm.
Slip Rate	<0.2 mm/yr	QFFD	Personius, 2002b
Sense of Movement	Reverse, right lateral	Geologic mapping	Beeson et al., 1989b

Canby-Molalla Fault			
	Data	**Type of Data**	**References**
Length	51 km	Earthquake scenario and probabilistic ground shaking maps	Wong et al., 2000
	50 km	QFFD	Personius, 2002c
Strike	N34°W	QFFD	Personius, 2002c
Dip	70° NE	Earthquake scenario and probabilistic ground shaking maps	Wong et al., 2000
	67° NE	Focal Mechanisms from microseismicity	University of Washington, 1963
	75° NE	Focal Mechanisms from microseismicity	University of Washington, 1963
Slip Rate	<0.2 mm/yr.	QFFD	Personius, 2002c
	Poor geomorphic expression (based on offsets from Blakely et al., 2000) suggests low slip rates in late Quaternary.	QFFD	Personius, 2002c
Displacement	4km right-lateral separation of underlying Eocene bedrock, and minimum of 150m of vertical offset in CRBG	Aeromagnetic data	Blakely et al., 2000
Sense of Movement	Right-lateral	Aeromagnetic data	Blakely et al., 2000
	Right-lateral, reverse	QFFD	Personius, 2002c

East Bank Fault			
	Data	**Type of Data**	**Reference**
Location	Parallel Portland Hills Fault, 2-3 km to the east.	QFFD	Personius, 2002d
Length	29 km	QFFD	Personius, 2002d
	55 km	Earthquake scenario and probabilistic ground shaking maps	Wong et al., 2000
Strike	N46°W	QFFD	Personius, 2002d
	N42°W	Low-altitude aeromagnetic data	Blakely et al., 1995
Dip	SW	QFFD	Personius, 2002d
	NE	Low-altitude aeromagnetic data	Blakely et al., 1995
	70-90° NE	Earthquake scenario and probabilistic ground shaking maps	Wong et al., 2000
	65°	Focal Mechanisms from microseismicity	University of Washington, 1963
Sense of Movement	Reverse	QFFD	Personius, 2002d
	High angle normal fault	Geologic mapping	Madin, 1990; Beeson et al., 1991
	Reverse slip	Low-altitude aeromagnetic data	Blakely et al., 1995
Slip Rate	< 0.2 mm/yr	QFFD	Personius, 2002d
	Estimated rates 0.05-0.4 mm/yr	Earthquake scenario and probabilistic ground shaking maps	Wong et al., 2000
Offset	60-120 m of down to the west vertical displacement of Miocene CRBG volcanic rocks and 60-90 m of vertical displacement of Miocene-Pliocene Troutdale Formation across the fault.	Cross-sections and geologic mapping	Beeson et al., 1991
Most Recent Activity	Late Pleistocene or Holocene vertical displacement, observed in seismic reflectors.	Shallow seismic reflection	Pratt et al., 2001

Gales Creek Fault			
	Data	**Type of Data**	**References**
Location	Fault forms the southwest margin of the Tualatin Basin	Geologic mapping	Popowski, 1996
	Bounding Coast Range uplift	Aeromagnetic data	Blakely et al., 2000
Length	31 km	Earthquake scenario and probabilistic ground shaking maps	Wong et al., 2000
	73 km	QFFD	Personius and Haller, 2017a
Strike	N41°W	QFFD	Personius and Haller, 2017a
Dip	Steeply dipping to the west	Structural and geologic mapping	Wells, personal comm., 2018
	70° NE	Earthquake scenario and probabilistic ground shaking maps	Wong et al., 2000
Sense of Movement	Reverse and right-lateral	QFFD	Personius and Haller, 2017a
	Dextral	Geologic mapping and gravity data	Wells, 2009
	Dextral strike-slip and vertical separation apparent along fault zone	Seismic design mapping	Geomatrix Consultants Inc., 1995
	Dextral slip indicated by: subhorizontal slickensides, vertical offsets varying along strike, dextral separation of Coast Range fold axes, and 6km dextral separation of CRBG beds between Dundee Hills and Parrett Mountain.	Aeromagnetic data	Blakely et al., 2000
Slip Rate	0.1-0.4 mm/yr	Earthquake scenario and probabilistic ground shaking maps	Wong et al., 2000
	<0.2 mm/yr	QFFD	Personius and Haller, 2017a
	0.24 mm/yr since 50 Ma and 0.6 mm/yr since 15 Ma	Structural and geologic mapping	Ray Wells, 1997 (personal comm. With Wong, 2000
Other	If part of the larger Gales Creek-Mount Angel fault zone, the vertical separation may have reverse sense of displacement	Seismic design mapping	Geomatrix consultants Inc., 1995

Helvetia Fault			
	Data	**Type of Data**	**References**
Location	Extends from the McKay Creek valley SE to Orenco	Water well logs	Popowski, 1996
Length	10 km	Earthquake scenario and probabilistic ground shaking maps	Wong et al., 2000
	7 km	QFFD	Personius, 2002e
Strike	N25°W	Water well logs	Popowski, 1996
	N26°W	QFFD	Personius, 2002e
Dip	70° W	Earthquake scenario and probabilistic ground shaking maps	Wong et al., 2000
Slip Rate	<0.2 mm/yr	QFFD	Personius, 2002e
Sense of Movement	Right-lateral, reverse	QFFD	Personius, 2002e
Displacement	100m CRBG is much thicker to the west	Well logs	Popowski, 1996
Most Recent Activity	Fault displacement likely occurred in late Miocene to Pliocene.	Seismic reflection shows erosion and folding of basalt, but no vertical deformation in overlying sediments	Popowski, 1996

Lackamas Lake (Sandy River/Frontal) fault			
	Data	**Type of Data**	**References**
Location	Northern end of Lackamas Lake	Based on topography and evidence of fault gouge	Yelin and Patton, 1991
	Forms northeast boundary of Portland Basin.	Aeromagnetic data	Blakely et al., 1995
	Parallel Portland Hills fault, north of the Columbia River in Washington	Topography and focal mechanisms from microseismicity	Yelin and Patton, 1991
Length	7 km southeast from northern end of Lackamas lake.	Topography	Yelin and Patton, 1991
	44 km	Earthquake scenario and probabilistic ground shaking maps	Wong et al., 2000
Strike	NW	Topography	Yelin and Patton, 1991
	N30°W	Zone of earthquakes along eastern margin of Portland Basin striking in this orientation.	Yelin and Patton, 1991
	NW	Aeromagnetic data	Blakely et al., 1995; 2000
Dip	Fault is displaced down to the west	Inference based on topography	Mundorff, 1964
	70° SW	Earthquake scenario and probabilistic ground shaking maps	Wong et al., 2000
	36° SW	Focal Mechanisms from microseismicity	University of Washington, 1963
	45° SW	Focal Mechanisms from microseismicity	University of Washington, 1963
Sense of Movement	Normal	Inference based on topography.	Mundorff, 1964
	Dextral strike-slip with component of normal faulting	Gravity data	Yelin and Patton, 1991
Depths	15-20 km	Focal Mechanisms from earthquakes.	Yelin and Patton, 1991
Most Recent Activity	Mw 5.2 EQ in 1962 occurred between Frontal and Portland Hills faults	Location of earthquake epicenter	Yelin and Patton, 1991
Age	Age unknown, but fault displaces rock of late Oligocene age	Groundwater investigation	Mundorff, 1964
Other	Frontal fault and Portland Hills fault are right-stepping, right-lateral fault zones	Focal Mechanisms from microseismicity	Yelin and Patton, 1991

Mount Angel Fault			
	Data	**Type of Data**	**References**
Length	30 km	QFFD	Personius, et al., 2014
	>55 km, interpreted to connect with the geologically mapped GCF to the NW.	Aeromagnetic data	Blakely et al., 2000
Strike	N43°E	QFFD	Personius, et al., 2014
	N24°W	Earthquake main shock focal mechanisms	Blakely et al., 2000; Thomas et al., 1996
	Defined plane in West-Northwest direction	Aftershocks from 1993 Scotts Mills EQ	Yeats et al., 1996
	Northwest	Earthquake focal mechanisms (1993 Scotts Mills EQ)	Thomas et al., 1996
Dip	60° NE	Earthquake focal mechanisms (1993 Scotts Mills EQ)	Thomas et al., 1996
	58° NE	Earthquake main shock focal mechanisms	Blakely et al., 2000; Thomas et al., 1996
	60-70° NE	Seismic reflection and aeromagnetic data	Werner, 1990; 1992; Yeats et al., 1996
	80°	Focal Mechanisms from microseismicity	University of Washington, 1963
Sense of Movement	Reverse, right-lateral	QFFD	Personius, et al., 2014
	Subequal reverse and right-lateral strike-slip	Earthquake focal mechanisms (1993 Scotts Mills EQ)	Thomas et al., 1996
	Dip-slip and right-lateral strike-slip	Geologically mapped	Beeson et al., 1989b
	High angle reverse-oblique	Boreholes	Werner, 1990
Slip Rate	<0.2 mm/yr	QFFD	Personius, et al., 2014
	0.23 mm/yr (for the past 30 Ka)	SH-wave refraction and reflection methods	Wang and Madin, 2001
Displacement	200m offset in CRBG	Seismic and Aeromagnetic data	Liberty et al., 1999
Most Recent Activity	Mw 5.6 Scott Mills Earthquake (1993)	Aeromagnetic data; Focal mechanisms	Blakely et al., 2000; Yeats et al., 1996
Other	May connect with the Gales Creek fault 25 km to the NW	Aeromagnetic data	Blakely et al., 2000

Newberg Fault			
	Data	**Type of Data**	**References**
Location	Part of Gales Creek-Mount Angel northwest-striking structural zone	QFFD	Personius, 2002g
Length	8 km	Earthquake scenario and probabilistic ground shaking maps	Wong et al., 2000
	5 km	QFFD	
Strike	N42°W	QFFD	Personius, 2002g
Dip	70° SW	Earthquake scenario and probabilistic ground shaking maps	Wong et al., 2000
Slip Rate	<0.2 mm/yr	QFFD	Personius, 2002g
Sense of Movement	Reverse, if connected to Gales Creek / Mt. Angel fault zone	Geologic and structural mapping	Ray Wells, personal comm.
Other	This structure may link the Mount Angel and Gales Creek faults	Magnetic expression	Blakely et al., 2000

Oatfield (Sylvan-Oatfield) Fault			
	Data	**Type of Data**	**Reference**
Location	Along western flank of the Portland Hills.	Gravity	Blakely et al., 2000
Length	29 km	QFFD	Personius, 2002h
	40 km	Gravity	Blakely et al., 2000
	40 km	Earthquake scenario and probabilistic ground shaking maps	Wong et al., 2000
Strike	N41°W	QFFD	Personius, 2002h
Dip	NE	QFFD	Personius, 2002h
	70° E	Earthquake scenario and probabilistic ground shaking maps	Wong et al., 2000
	SW	Geologically mapped	Beeson et al., 1989b
	East-dipping	Exposures from boreholes drilled for metropolitan light-rail tunnel through the Portland Hills.	Blakely et al., 1997
	Steeply; NE	Aeromagnetic data	Blakely et al., 1995
Sense of Movement	Reverse and right-lateral	QFFD	Personius, 2002h
	High-angle reverse fault	Geologically mapped	Beeson et al., 1989b
	Reverse and strike slip	Microseismicity	Yelin, 1992
	Thrust	Aeromagnetic data	Blakely et al., 1995
	Reverse (vertical) and dextral	Exposures from boreholes drilled for metropolitan light-rail tunnel through the Portland Hills.	Blakely et al., 1997
Slip Rate	<0.2 mm/yr	QFFD	Personius, 2002h
	Estimate of 0.05-0.4 mm/yr	Earthquake scenario and probabilistic ground shaking maps	Wong et al., 2000
Offset	100m offset of 1 Ma Boring Lava	Exposures from boreholes drilled for metropolitan light-rail tunnel through the Portland Hills.	Blakely et al., 1997
Other	The fault forms linear magnetic anomalies and southwest-facing escarpments in volcanic rocks of the Miocene CRBG in Tualatin Mtns, and northern Willamette Valley.	Geologically mapped	Beeson et al., 1989b; 1991
	150 m of Mio-Pleistocene age sediments are stratigraphically above CRBG	Water wells	Popowski, 1996; Madin, 1990
	Boring lava vents along the length of the fault suggest it acted as a conduit for emplacement of Boring lava	Water wells and geologically mapping	Popowski, 1996
	The Sylvan fault is interpreted as a subsurface continuation of the Oatfield fault.	Gravity data	Blakely et al., 2000

Portland Hills Fault			
	Data	**Type of Data**	**References**
Location	Part of Portland Hills-Clackamas River structural zone, SE Portland?	Geochemical analysis of Frenchman Springs Member of the CRBG	Beeson et al., 1985
	Forms NE margin of Tualatin Mountains and SW margin of Portland Basin	QFFD	Personius and Haller, 2017b
Length	49 km	QFFD	Personius and Haller, 2017b
	Active zone of deformation is 400 m wide	Seismic reflection, GPR, magnetic methods, trench excavation @ North Clackamas Park and Rowe Middle school	Liberty et al., 2003
	62 km	Earthquake scenario and probabilistic ground shaking maps	Wong et al., 2000
Strike	N37°W	QFFD	Personius and Haller, 2017b
	NW	Geologically mapped	Beeson et al., 1989b
Dip	SW	QFFD	Personius and Haller, 2017b
	Steeply SW	Geologic Mapping	Schlicker and Finlayson, 1979
	SW	Aerial and field reconnaissance	Unruh et al, 1994
	NE	Geologic mapping	Beeson et al., 1989b
	70° NE	Seismic design mapping	Geomatrix Consultants, Inc., 1995
	NE side up displacement	Shallow seismic reflection data	Pratt et al., 2001
	SW	Aeromagnetic data	Blakely et al., 1995
	70-90° SW	Earthquake scenario and probabilistic ground shaking maps	Wong et al., 2000
Sense of Movement	Reverse, right-lateral	QFFD	Personius and Haller, 2017b
	Right-lateral	Geologic mapping	Schlicker and Finlayson, 1979
	Right-lateral strike slip	Geologic mapping	Beeson et al., 1985
	Reverse to vertical	Earthquake scenario and probabilistic ground shaking maps	Wong et al., 2000
	Normal	Geologic mapping, based on CRBG and November 1962 earthquake	Schlicker et al., 1964; Balsille and Benson, 1971
	Right-oblique strike-slip	Geologic mapping	Beeson et al., 1989b
	Asymmetrical folding above SW dipping blind thrust	Based on topography of Portland Hills escarpment	Unruh et al., 1994

	Near vertical dip slip	Geologic mapping	Beeson et al., 1989b
	Reverse or reverse oblique	Seismic design mapping	Geomatrix consultants, Inc., 1995
	Transpressional	Aeromagnetic data	Blakely et al., 1995
	Strike-slip with minor dip slip component.	Seismic reflection, GPR, magnetic methods, trench excavation at North Clackamas Park and Rowe Middle school, Clackamas.	Liberty et al, 2003
	Strike-slip or dip slip	Seismic profiling	Pratt et al., 2001
	Reverse is primary mode of deformation.	Seismic reflection data	Wong et al., 2001
	Right-stepping, right-lateral fault zone.	Microseismicity	Yelin and Patton, 1991
	Reverse displacement, with component of right-lateral strike slip.	Tectonic setting and geologic mapping	Beeson et al., 1989; Blakely et al., 2000
	Reverse	Aeromagnetic data	Blakely et al., 1995
Slip Rate	<0.2 mm/yr	QFFD	Personius and Haller, 2017b
Depth	5-20 km	Microseismicity	Wong et al., 2001; Yelin and Patton, 1991
Other	Fault defines western margin of pull-apart basin.	Geologic mapping	Beeson et al., 1989b
	Faulted anticline of Miocene CRBG.	Geologic mapping and subsurface data	Evarts et al., 2009
	Fault trace corresponds with low gravity values (-28 mGal), so likely dense basement rocks are not major part of Portand Hills uplift.	Gravity inversion	McPhee et al., 2014

Sherwood Fault			
	Data	**Type of Data**	**References**
Location	Separates NE dipping Chehalem Mountain beds from SE dipping Parrett Mountains	Water well logs	Hart and Newcomb, 1965
	Possibly continues along northern end of Amity Hills.	Seismic profiles	Yeats et al., 1996
	Appears as southwest continuation of northern margin of Columbia trans-arc lowland through which CRBG traversed the Cascade Range.	Geochemistry and geologic mapping of the CRBG	Beeson et al., 1989a
	Bounds the southeastern margin of the Tualatin Basin and northern margin of the northern Willamette basin	A broad northeast-trending gravity high	McPhee et al., 2014
Length	14.5 km	Geologic mapping of bedrock faults.	Wells et al., 2019
Strike	NE	Aeromagnetic data	Blakely et al., 2000
Dip	50° S	Focal Mechanisms from microseismicity	University of Washington, 1963
Displacement	Basement to northwest of the fault is offset vertically ~300 m lower than to the south	Aeromagnetic data	McPhee et al., 2014
Other	Could be offset right-laterally by the Gales Creek fault to the west. The offset part on the northwest end of the Gales Creek fault.	Geologic mapping	Wells personal comm. (2018)
	Originated as normal fault in the Eocene.	Aeromagnetic data	McPhee et al., 2014
	On strike and possibly related to Lake Oswego fault.	Geologic mapping	Popowski, 1996; Beeson et al., 1989b

Appendix A2. Fault dip and depth information from focal mechanisms

Beaverton Fault					
Strike	**Dip**	**Magnitude EQ**	**Depth of EQ (km)**	**Distance from fault (km)**	**Length of fault at Depth**
60°	70°	2.6	26.1	0.659	26.1

Canby Molalla Fault					
Strike	**Dip**	**Magnitude EQ**	**Depth of EQ (km)**	**Distance from fault (km)**	**Length of fault at Depth**
315°	75°	2.4	21.2	4.8	21.7
319°	67°	2.1	22.2	3.46	22.4

East Bank Fault					
Strike	**Dip**	**Magnitude EQ**	**Depth of EQ (km)**	**Distance from fault (km)**	**Length of fault at Depth**
320°	65°	2.8	15.2	0.34	15.2

Gales Creek Fault					
Strike	**Dip**	**Magnitude EQ**	**Depth of EQ (km)**	**Distance from fault (km)**	**Length of fault at Depth**
330°	90°	2.4	25.2	29.9	39.1

Lackamas Lake Fault					
Strike	**Dip**	**Magnitude EQ**	**Depth of EQ (km)**	**Distance from fault (km)**	**Length of fault at Depth**
104°	36°	2.5	5.6	4.06	6.9
125°	45°	2.5	15	7.13	16.6

Mount Angel Fault					
Strike	**Dip**	**Magnitude EQ**	**Depth of EQ (km)**	**Distance from fault (km)**	**Length of fault at Depth**
340°	80°	2.4	25.2	8.89	26.7

Sherwood Fault					
Strike	**Dip**	**Magnitude EQ**	**Depth of EQ (km)**	**Distance from fault (km)**	**Length of fault at Depth**
95°	50°	2	20.7	2.77	20.9

Appendix A3. Large induced earthquakes

EQ	Magnitude	Year	Injection Type	Volume per month (gallons)	Depth of Injection (feet)	Notes	Source
Prague	M5.6	2011	Wastewater injection wells	~168,000,000 gallons per month	7,217-11,483 feet	The only pressure data available for the Wilzetta North injection field are monthly reported wellhead pressure (the pressure at ground surface while pumping). There are no direct measurements of pressure within the reservoir available. Study by Keranen and others (2013) postulate a link between increased volume of fluid injection and the Prague earthquake.	Keranen et al., 2013
Fairview	M5.1	2016	Wastewater injection wells	>12,600,000 gallons per month	6,561-8,202 feet	Suggested cause: far-field pressurization from clustered, high-rate wells likely induced the earthquake. Suggests pre-existing faults have role in the occurrence of such a large induced earthquake.	Yeck et al., 2016 Goebel et al., 2017
Pawnee	M5.8	2016	Wastewater injection wells	Range from 7,138,888 – 135,416 gallons per month	~6,000 feet	Earthquake occurred in region with active wastewater injection into a basal formation group. There was an increase in injection	Barbour et al., 2016; Auch, 2016

						rates in the years just before 2016.	
Basel Event	M3.4	Dec. 9, 2006	Hot dry rock enhanced geothermal system	2,377,530 gallons per month	16,404 feet	Basel, Switzerland is located on a historically active fault that destroyed the city in 1356 There were numerous other smaller events before and after	The Sydney Morning Herald, 2007; Dyer et al., 2007

Appendix A4. *List of Publications Resulting from this Project*

Bershaw, J., Burns, E. R., Cladouhos, T. T., Horst, A. E., Van Houten, B., Hulseman, P., ... & Williams10, C. F. (2020). An integrated feasibility study of reservoir thermal energy storage in Portland, Oregon, USA. In 45th Workshop on Geothermal Reservoir Engineering.

Burns, E. R., Bershaw, J., Williams, C. F., Wells, R., Uddenberg, M., Scanlon, D., ... & Van Houten, B. (2020). Using saline or brackish aquifers as reservoirs for thermal energy storage, with example calculations for direct-use Heating in the Portland Basin, Oregon, USA. Geothermics, 88, 101877.

Burns, E.R., Cladouhos, T.T., Williams, C.F. and Bershaw, J. (2018). Controls on Deep Direct-Use Thermal Energy Storage (DDU-TES) in the Portland Basin, Oregon, USA. GRC Transactions. Vol. 42.

Horst, A. E., Streig, A. R., Wells, R. E., & Bershaw, J. (2021). Multiple Holocene Earthquakes on the Gales Creek Fault, Northwest Oregon Fore-Arc. Bulletin of the Seismological Society of America, 111(1), 476-489.

Scanlon, D. P., Bershaw, J., Wells, R. E., & Streig, A. R. (2021). The spatial and temporal evolution of the Portland and Tualatin forearc basins, Oregon, USA. Geosphere, 17(3), 804-823.

Sonnenthal, E. L., Smith, J. T., Dobson, P. F., & Nico, P. S. (2021). Thermal-Hydrological-Mechanical Models for Evaluating Reservoir Thermal Energy Storage in the Portland Basin, Oregon.